CSIC
Consejo Superior de Investigaciones Científicas

UAM
Universidad Autónoma de Madrid

Studies on secondary electron emission induced charging in dielectric materials: Novel methods and applications for space and plasma technologies

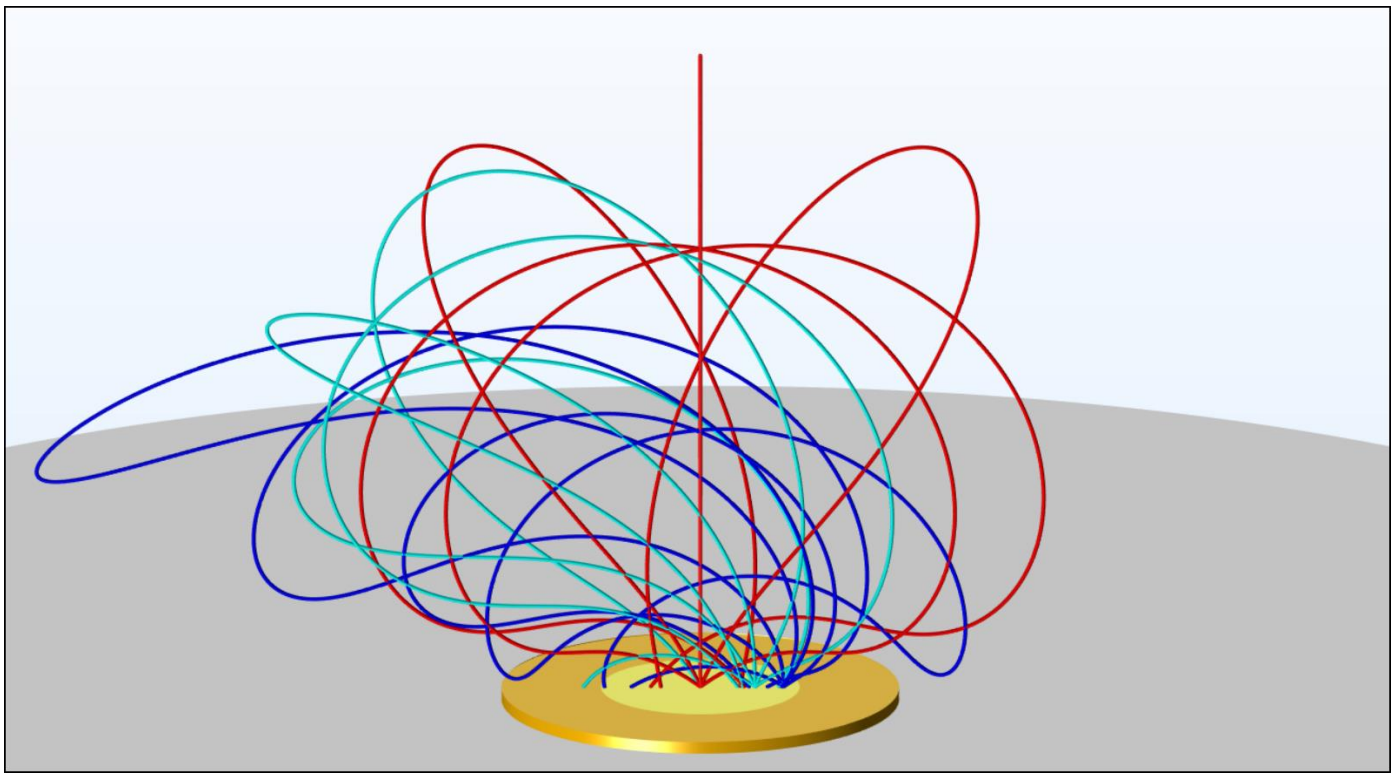

Leandro Olano García

Directora **Prof. Dra. Isabel Montero Herrero**

Codirectora **Dra. María Eugenia Dávila Benítez**

Studies on secondary electron emission induced charging in dielectric materials: Novel methods and applications for space and plasma technologies

Leandro Olano García

Memoria para optar al grado de Doctor en Ciencias Físicas

Directora

Prof. Dra. Isabel Montero Herrero

Codirectora

Dra. María Eugenia Dávila Benítez

Tutor:

Prof. Dr. Máximo León Macarrón

Madrid

Diciembre 2020

CSIC
Consejo Superior de Investigaciones Científicas

UAM
Universidad Autonoma de Madrid

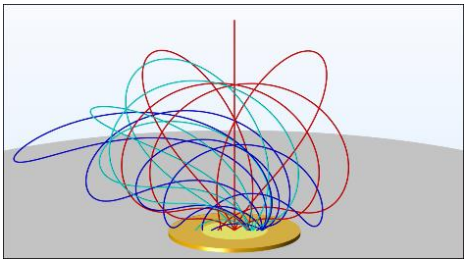

Comsol simulation of secondary electrons trapped in a positively charged sample. Different colors describe the initial position of the secondary electron at emission. The bright yellow circular area in the center of the circular sample denotes the irradiated surface. Picture extracted from: L. Olano, I. Montero. Energy spectra of secondary electrons in dielectric materials by charging analysis. *Results in Physics*, Volume 19, 2020, 103456, ISSN 2211-3797. https://doi.org/10.1016/j.rinp.2020.103456.

A mi familia,

A mis padres,

A mi hermano.

"What is mind? No matter.

What is matter? Never mind."

Bertrand Russell.

Agradecimientos

Es imposible agradecer lo suficiente a todos los que han colaborado en esta tesis y desgraciadamente, es muy posible que me deje a alguien sin mencionar. Espero que sepa no tenérmelo en cuenta.

En primer lugar, me gustaría empezar agradeciendo tanto a mi directora de tesis la Prof. Isabel Montero, como a mi codirectora de tesis la Dra. Maria Eugenia Dávila. Sin ellas, este trabajo habría sido imposible desde el minuto uno y, desde luego, yo no sería la persona que soy hoy. En especial, querría agradecerle a Isabel su disponibilidad y las horas y horas de trabajo codo con codo en el laboratorio durante todos estos años. Gracias por todo lo que he aprendido contigo.

Without any doubt, part of this work could not have been possible without the help and time of Prof. John Robert Dennison. My time in Logan, Utah, working in your laboratory was unforgettable, I learnt a lot there, scientifically and personally. That experience also made me the person I am today.

A todos los compañeros de laboratorio que han trabajado a mi lado. Gracias Francisca, Pablo, Dani, Rafa, Victor, Tiancun. Gracias a ti también Lydya, por enseñarme junto a Isabel aquellos primeros meses de mi andanza por el laboratorio.

Un trabajo de investigación no puede desarrollarse apropiadamente sin los servicios de apoyo a la investigación. Gracias a todos aquellos con los que he tratado estos años ya sea una o mil veces. En especial, me gustaría agradecer al servicio de SEM del SiDi de la *Universidad Autónoma de Madrid* por amenizar tantas horas junto a ellos, tanto que he acabado extrañando esas sesiones durante este extraño año de cuarentenas: Esperanza, Gabi e Isi. Agradecer especialmente también a Alfredo Jacas su disposición a la hora de resolver cualquier problema cuando me surgía, su positividad es siempre bienvenida, ánimo con todo.

A mi tutor de la Universidad Máximo León Macarrón por su inestimable ayuda.

A todos mis amigos del ICMM, sin vosotros estos años no habrían sido igual, como digo, habéis pasado a ser mis amigos y por tanto no me es posible agradeceros todo lo que me habéis dado, Juan José, Leo, Sandra, David, Rebe, Jose, Enrique, Unai, Irene, Lety, Rafa, Dulce, Adri (el orden no es importante). Que el final de nuestras tesis no nos separe y nos sigamos viendo en Casa Labra. Que el 2021 sea el año en que podamos celebrar, hablar y reír todo lo que el 2020 no nos ha dejado. A Helena, Celia y Jose por su amistad, estos años tampoco habrían sido igual sin vosotros. A Nacho, Gonzalo, Paloma y Ricardo, por todos los buenos momentos, sobre todo en las celebraciones del ICMM.

A mis amigos de la carrera, que ya son mis amigos de la vida, Laura, Gallego, Seo, Barriles, Bravo, Ikki, Alber, Irene, Alberto, Vicky, Filósofa, Ben, Capo (el orden tampoco es importante aquí). En especial a Laura por ser mucho más que una amiga y estar conmigo en las duras y en

las maduras todos estos años y a Gallego por tener que haber aguantado todos mis problemas y quejas. Sin vosotros no sé qué habría sido de mí. Gracias.

A Edu, por todas esas tardes de cine malo y charla que nos hemos comido con mi hermano o sin él. Por las visitas al aeropuerto disfrazados para recibir a mi hermano, no sé cómo alguna vez no hemos acabado en un calabozo.

A Ami, aunque has llegado la última, parte de esta tesis es también tuya. Estos últimos años, tú me has levantado el ánimo cuando me ha hecho falta y me has relajado con tu cariño. Te quiero, salvo cuando pones una peli de miedo que entonces, te necesito.

Finalmente, y por ello quizá más importante, quería agradecer a mi familia todos estos años, porque sin todos ellos seguro que no hubiese llegado a ser quien soy. Pienso en mis abuelas y en las largas y amenas conversaciones de sobremesa con mi tío Luis Miguel sobre casi cualquier tema. Pienso también, en la divertida dedicación de mi tío Fernando, tus enseñanzas de Blender son, sin duda, parte de lo que soy hoy. Muy especialmente, quería agradecer a mis padres, por haberme dado todo. Sobre todo, unas bases sobre las que he podido construir mi vida, tanto personal como profesional, tanto científica como cultural. Sólo espero poder estar a la altura y haceros sentir orgullosos. A mi hermano, por ser el espejo en el que me miro, simplemente no hay palabras con las que poder, si quiera, empezar a agradecer nada.

A todos, muchas gracias.

Contents

Table of acronyms and symbols

SEE	Secondary Electron Emission
SEY	Secondary Emission Yield
SE	Secondary Electrons
PE	Primary Electrons
ISE	Internal Secondary Electrons
EDC	Energy Distribution Curve
MFP	Mean Free Path
IMFP	Inelastic Mean Free Path
EMFP	Elastic Mean Free Path
EC	Electron Cloud
RF	Radio Frequency
CSDA	Continuous Slowing Down Approximation
MC	Monte Carlo
AES	Auger Electron Spectroscopy
XPS	X-Ray Photoelectron Spectroscopy
HEEA	Hemispherical Electron Energy Analyzer
SEM	Scanning Electron Microscope
EDX	Energy Dispersive X-Ray Spectroscopy
FC	Faraday Cup
PMT	Photomultiplier Tube
CFA	Cross Field Amplifiers
σ	Total Secondary Electron Emission Yield (SEY)
δ	True Secondary Electron Emission Yield
η	Total Backscattered Electron Emission Yield
η_i	Inelastically Backscattered Electron Emission Yield
η_e	Elastically Backscattered Electron Emission Yield
E_P	Primary Energy
E_1	First cross-over energy of the SEY curve
E_2	Second cross-over energy of the SEY curve

SEY_{max}, σ_{max}	Maximal SEY of a material
E_{max}	Energy at which SEY is SEY_{max}
E’	Primary energy at which R ~ r
R	Maximum penetration range of primary electrons
r	Maximum escape depth of secondary electrons
λ	Mean escape depth of secondary electrons

Abstract

The interaction of ionizing radiation with matter is of critical importance in many areas of science and technology such as space and plasma technology. Secondary electron emission is a direct consequence of electron irradiation on materials. To characterize materials in terms of secondary electron emission, the secondary emission yield (SEY) and the energy spectra of the secondary electrons are key physical properties. Secondary emission yields of materials are usually too high to avoid Multipactor effect or other related phenomena in applications for space. In addition, the measurement of electron energy spectra of secondary electrons in dielectric materials is a challenge due to charging issues.

For the first time, in this doctoral thesis, a synergy between conductor and dielectric domains in composite materials have been experimentally reported and modeled. Composite materials with SEY < 0.2 up to high primary energies (~1 keV) have been prepared and characterized. These composite materials have been modeled using a deterministic simulation to obtain an insight on the interaction process between domains that produces such extremely low secondary emission yield.

To obtain the electron energy spectra of dielectric materials, a method that takes advantage of the charging of dielectric materials during electron irradiation has been developed. The method was first tested on floating conductor samples, specifically for Cu, Ag and Au films. The results show a good fit between the new model proposed in this doctoral thesis and the electron spectra obtained with a hemispherical electron energy analyzer. Once the validity of the method was proved, it was used on dielectric materials. Kapton, Teflon and Ultem polymers were selected due to their applications in the space industry. The energy spectra of secondary electrons of these materials was measured and it showed a peak at 1.9 ± 0.1 eV for Kapton, 2.3 ± 0.1 eV for Teflon and 4.3 ± 0.2 eV for Ultem.

The results shown in this thesis on the composite materials pave the way to design new materials of low secondary emission yield. These materials are needed in certain vacuum applications, such as RF communications, as a high secondary emission yield produces an electron avalanche that limits the maximum working power of the RF devices. Also, the research on the charging of dielectric materials under electron irradiation has provided a new method to characterize the secondary electron energy spectra of dielectrics. The measurement of these spectra has been traditionally difficult due to the charging of the material as high

electron doses were needed. The presented new method allows to obtain the energy spectra with doses of only 10 pC/mm^2, which ensures a minimal distortion of the pristine state of the dielectric material by avoiding radiation damage, deep charging, defects, aging and other electron induced phenomena on the insulator.

Following the regulations of the *Universidad Autónoma de Madrid (UAM)*, this doctoral thesis is presented as a compendium of publications. The manuscript is divided into four parts. A general introduction exposing the main concepts of Secondary Electron Emission can be found in **Chapter 1**. This is followed by a global summary of the results and their discussion in **Chapter 2**. The main publications, *Publications 1, 2 and 3* that have been produced as part of this doctoral thesis can be found in **Chapter 3**. Finally, the conclusions are included in **Chapter 4**.

Resumen

La interacción de la radiación ionizante con la materia es de suma importancia en muchas áreas de la ciencia y tecnología, como la tecnología espacial y del plasma. La emisión de electrones secundarios es una consecuencia directa de la irradiación de electrones sobre los materiales. Para caracterizar los materiales en términos de emisión secundaria de electrones son clave las propiedades físicas del rendimiento de emisión secundaria (SEY según sus siglas en inglés) y el espectro de energía de los electrones secundarios. Los rendimientos de las emisiones secundarias de los materiales suelen ser demasiado altos para evitar el efecto Multipactor u otros fenómenos relacionados en las aplicaciones espaciales. Además, la medición de los espectros de energía de electrones secundarios en materiales dieléctricos es un desafío debido a problemas de carga.

Por primera vez, en esta tesis doctoral, se ha informado y modelado experimentalmente una sinergia entre dominios conductores y dieléctricos en materiales compuestos. Se han preparado y caracterizado materiales compuestos con SEY < 0.2 hasta energías primarias elevadas (~ 1 keV). Estos materiales compuestos se han modelado mediante una simulación determinista para obtener más información del proceso de interacción entre dominios que produce tan extremadamente bajo rendimiento de emisión secundaria.

Para obtener los espectros de energía de electrones de materiales dieléctricos, se ha desarrollado un método que aprovecha la carga de materiales dieléctricos durante la irradiación de electrones. El método se probó primero en muestras de conductores flotantes, específicamente para películas de Cu, Ag y Au. Los resultados muestran un buen ajuste entre el nuevo modelo propuesto en esta tesis doctoral y los espectros de electrones obtenidos con un analizador de energía de electrones hemisférico. Una vez probada la validez del método, se utilizó en materiales dieléctricos. Los polímeros Kapton, Teflon y Ultem fueron seleccionados debido a sus aplicaciones en la industria espacial. Se midió el espectro de energía de los electrones secundarios de estos materiales que mostró un pico de 1.9 ± 0.1 eV para Kapton, 2.3 ± 0.1 eV para Teflon y 4.3 ± 0.2 eV para Ultem.

Los resultados mostrados en esta tesis sobre los materiales compuestos pavimentan el camino para diseñar nuevos materiales de baja SEY. Estos materiales son necesarios en ciertas aplicaciones de vacío, como las comunicaciones RF, ya que un alto rendimiento de emisión secundaria produce una avalancha de electrones que limita la potencia máxima de trabajo de

los dispositivos de RF. Además, la investigación sobre la carga de materiales dieléctricos bajo irradiación de electrones ha proporcionado un nuevo método para caracterizar los espectros de energía de electrones secundarios de los dieléctricos. Las mediciones de estos espectros han sido tradicionalmente difíciles debido a la carga del material ya que se necesitaban altas dosis de electrones. El nuevo método presentado permite obtener los espectros de energía con dosis de solo 10 pC/mm^2, lo que asegura una distorsión mínima del estado original del material dieléctrico al evitar daños por radiación, carga profunda, defectos, envejecimiento y otros fenómenos inducidos por electrones en el aislante.

Siguiendo la normativa de la Universidad Autónoma de Madrid (UAM), esta tesis doctoral se presenta como un compendio de publicaciones. El manuscrito se divide en cuatro partes. El **Capítulo 1** es una introducción general que expone los conceptos principales de Emisión de Electrones Secundarios. A esto le sigue un resumen global de los resultados y su discusión en el **Capítulo 2**. Las principales publicaciones, *Publicaciones 1, 2 y 3* que se han producido como parte de esta tesis doctoral se encuentran en el **Capítulo 3**. Finalmente, las conclusiones se incluyen en el **Capítulo 4**.

1 General introduction

2.1 Early historical overview

Secondary Electron Emission, SEE, is the process by which electrons are ejected from the surface of materials under incident irradiation. The study of this process has produced an interest in the scientific community throughout the last century, with a surge in the last decades to the present day. Such an interest can be seen in **Figure 1.1**, where the number of publications per year is shown. Some of the most cited works in the field are [1-6] which range topics as different as Scanning Electron Microscopy, Auger Electron Microscopy, dielectric charging, theory of electron emission and semiempirical models.

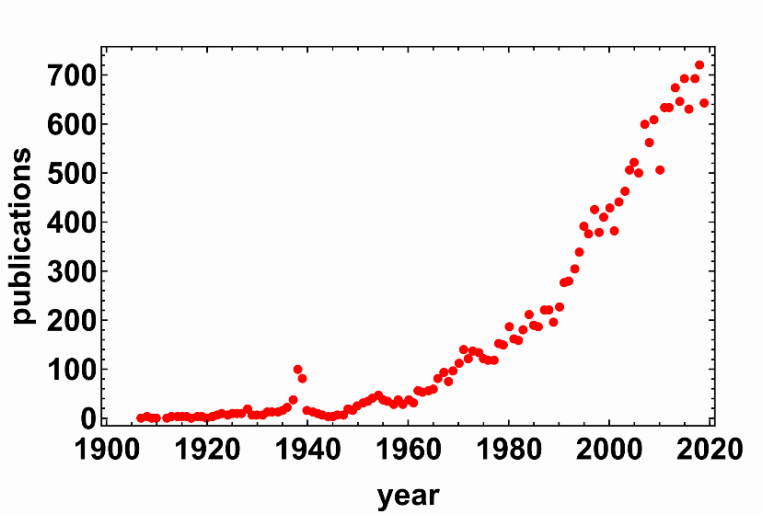

Figure 1.1. Number of publications on secondary electron emission since the discovery of the phenomena. It can be seen that the number of publications has increased monotonically with time.

SEE was first observed by Villard in 1899 [7] in Paris when he was studying cathode rays (high energy electrons). In his experiments he concluded that cathode rays were produced when Hydrogen cations hit a cathode. The first observation of secondary emission due to incident electrons was reported by Austin and Starke [8] at the Berlin University three years later. They were studying the reflection of cathode rays in metals when an unexpected positive current in the reflector plate at high incident angles was discovered, **Figure 1.2**. In their publication, they

concluded that only secondary emission of negative particles produced by the electron bombardment could explain their measurements. They supposed that the emission increased with the incident angle and correctly inferred that the current decreased with the energy at the energy range they used (several keV) and increased with the intensity of the cathode rays. Also, they found that the emission depended on the polishing of the surface, correctly stating that the better the polishing the greater the emission. They also concluded that the higher the density of the metal, the higher the secondary emission. They also made two wrong assumptions. (i) The energy of the emitted electrons was of the same order of the impinging cathode rays (several keV). (ii) The secondary emission disappeared at normal incidence. However, they discovered and correctly established some of the basic properties of secondary electron emission. We can even go a bit further in time, as Austin and Starke cite a work by Swinton [9] where he reported a platinum sheet positively charging to a few volts under electron irradiation. However, he did not go further to explain why that was happening.

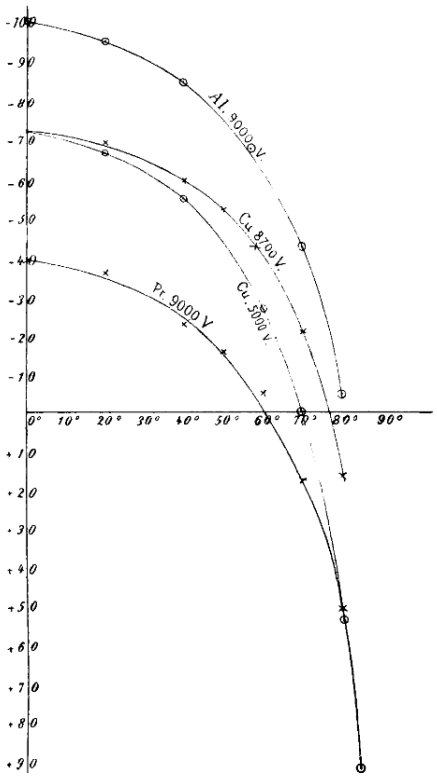

Figure 1.2. Registered current for different metals (Al, Cu, Pt) and different incident energies (in the order of keV) as a function of the angle of incidence of the primary electrons (or cathode rays). It can be seen the unexpected change of sign at high energies that can only be explained if the solid is emitting electrons. Figure extracted from the paper published by Austin and Starke reporting an unexpected negative current in the cathode at high incident angles [8].

It was the Noble prize winner Lenard [10] who corrected the two wrong statements of Austin and Starke. Lenard found that the energy of the outgoing secondary particles did not exceed 10 eV for copper and platinum. Also, he did not find any dependence of the energy of the secondary radiation on the angle of incidence, stating that *the speed of the secondary radiation was not significantly different even in the case of vertical primary incidence*. Lenard found that Platinum had a maximum yield at ~1000 eV.

Füchtbauer [11] studied simultaneously canal (positive ion beams) and cathode rays. He found low and similar energies (27 – 34 eV) for the secondary electrons produced by each phenomena and pointed out to a common cause. He also confirmed that the energy of the secondary electrons was independent of the energy of the incident electrons and their angle of incidence.

Füchtbauer in [12] and Laub in [13] independently and concurrently proposed that secondary electrons were extracted from a thin layer close to the surface of the bombarded material (interestingly, both works [12, 13] were published consecutively in the same issue). Concretely, Laub confirmed the results of Lenard and tried for the first time to describe theoretically the secondary electron emission process. In his experiment, Laub used a platinum plated thermometer to measure the energy deposited in the platinum by the incident electrons. The current from the platinum to ground was measured by a galvanometer. Using these two variables he could independently confirmed that: (i) secondary electron emission increased with the incident angle, (ii) there was emission even at normal incidence, (iii) the emission decreased with the energy of the incident electrons (incident energy of several keV), (iv) the energy of the secondary electrons was very low and did not depend much on the incident energy. (v) He also covered the platinum with several other metals (gold, silver, copper, nickel, aluminum and bismuth) and found no dependence of the energy of the secondary electrons on the material. (vi) The greater the density of the metal, the bigger the secondary emission (true for the energies of several keV). With these conclusions he attempted for the first time to lay a theoretical description of the secondary electron emission. He supposed that the incident electrons had straight trajectories in the solid and that the same number of electrons were excited at different incident angle, but at slanted angles and low incident energies this excitation was produced closer to the surface. This explained the increased emission at high angles and lower energies (always in the range of keV).

All these studies were carried on metals at the best available pressures at the moment ~ 10^{-4} – 10^{-5} hPa [14]. The first works in high vacuum were started in the 1920s with for example [15].

It was not until later, around the 1940s that studies on dielectric materials started, see [16] for example.

In 1918, Albert Hull was the first to propose a device that used the SEE [17]. It was a vacuum tube electronic oscillator called dynatron that characteristically had negative resistance due to the SEE. The dynatron was used to a limited extent from the 1920s to the 1940s in radio receivers. In 1919 Joseph Slepian proposed the first electron multiplier [18, 19] which was later applied in photomultiplier tubes, PMTs, probably the most extensively used application of SEE, even nowadays. PMTs were developed by Zworykin at the Radio Corporation of America in 1936 and commercialized soon afterwards [20]. However, some people date the invention of the photomultiplier in 1930 and attribute it to L. A. Kubetsky, still at that time a student of Physics in the old Leningrad [21]. Finally, what is probably the most scientifically relevant application came with the first commercial Scanning Electron Microscope, SEM, in 1965 by the Cambridge Instrument Company [22]. The foundations for this accomplishment were laid 30 years before by Knoll Max and more extensively by Manfred von Ardenne who patented in 1937 a proposal of a SEM [23]. Soon afterwards, his research in SEM had to be interrupted because of World War II when his work was necessarily diverted to nuclear physics. Regrettably, the electron microscope that von Ardenne built was destroyed in an air raid on Berlin in 1944 and he never resumed his work on the topic. It is remarkable that only sixty years after the discovery of the secondary electron emission, the development of the first commercial SEM was completed.

Soon afterwards SEE phenomena was found important in a new scientific and engineering field, the Space Race. In 1955, both United States and the Soviet Union announced that they would be launching artificial satellites by 1957-1958. This was first accomplished with the launch of the Sputnik 1, the *"fellow traveler"* on Friday, October 4, 1957 at 10:28:34 pm Moscow time by the URSS. The first measurements taken in orbit were performed by the Sputnik 2 a month later, which also carried the renowned dog called Laika. It measured solar radiation and cosmic rays. Three months later, USA successfully put the satellite Explorer 1 in orbit. It carried instrumentation that confirmed the existence of the Van Allen radiation belt. This is a belt of electrons and protons trapped around the Earth by its magnetic field [24]. With the data offered by these three first satellites the existence of photon, ion and electron radiation in orbit was confirmed. The study of SEE was going to be vital in the understanding of the interaction between spacecraft and space environment [25].

2.2 SEE and Transport of electrons in the solid

This section presents, the physical processes involved in the interaction between the incident or primary electrons (PE) and the solid and how secondary electrons (SE) are emitted.

2.2.1 Secondary electron emission process

The emission process of secondary electrons can be described in three consecutive steps:

- Transport of primary electrons in the solid.
- Generation of secondary electrons due to the interaction of the primary electron with the solid.
- Transport and escape over the surface potential barrier of the produced and backscattered secondary electrons.

The elastic and inelastic scattering of incident and secondary electrons are one of the most important phenomena that contribute to secondary electron emission.

2.2.2 Elastic and inelastic scattering of electrons

Both incident and excited electrons interact with the solid by two distinct and independent processes, elastic and inelastic scattering. The average distance traveled between two successive elastic events is called elastic mean free path, EMFP. Likewise, the average distance traveled between two successive inelastic events, regardless of the energy loss, is called inelastic mean free path, IMFP. The combination of both gives the mean free path, MFP.

$$\frac{1}{MFP} = \frac{1}{EMFP} + \frac{1}{IMFP} \tag{1.1}$$

These processes are dependent on the energy of the traveling electrons. At high energies, both components of the MFP increase with the electron energy. However, there is a minimum at low energies < 100 eV, see **Figure 1.3**. Usually, it is fulfilled that IMFP > EMFP [26-28].

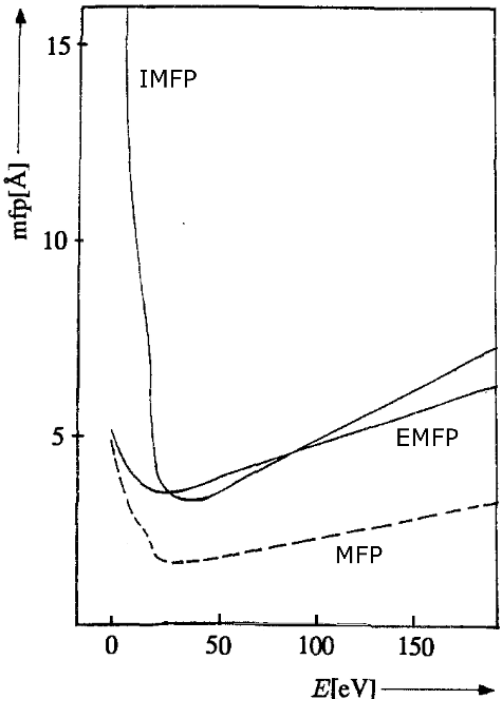

Figure 1.3. Energy dependence of the MFP (dashed line), EMFP (solid line) and IMFP (solid line) of electrons up to 200 eV in aluminum. It can be seen that the elastic mean free path is smaller than the inelastic mean free path. A minimum is observed at energies < 100 eV for the three different mean free paths. Modified figure extracted from [27].

The elastic scattering is due to the interaction of the traveling electrons with the screened Coulomb field of the nucleus of the atoms in the solid. This interaction can be properly described by the Mott cross-section. In contrast, the inelastic scattering is due to the interaction of the traveling electrons with defects in the solid, weakly bound electrons in the valence or conduction band of the solid and core electrons (the last interaction is only available to energetic electrons). The energy loss process produces excitation of the atoms that result in X-ray and Auger emission, production of plasmons and phonons and ultimately ejection of secondary electrons. Linear response theory and dielectric function models are used to describe the inelastic scattering. It is the case that momentum transfer or change in direction of the traveling electrons is controlled mainly by the elastic scattering and the energy loss (and therefore SE production) by the inelastic scattering [27-30].

2.2.3 Primary electron penetration depth

The penetration depth, R, is the maximum distance that an incident electron can penetrate in the solid before losing all its kinetic energy and stopping. This distance will mainly depend on the IMFP of the solid and the initial energy of the electron. The energy loss, and therefore R, can be computed in several ways, such as assuming a power law [31], a continuous slowing down approximation, CSDA, [32, 33] or by Monte Carlo methods, MC [28]. It is important to note that R is the total straight distance that an incident electron penetrates inside the solid. However, due to elastic scattering most electrons will be implanted at a depth closer to the surface than R. **Figure 1.4** shows a simulation on the CASINO software on aluminum performed in this doctoral thesis.

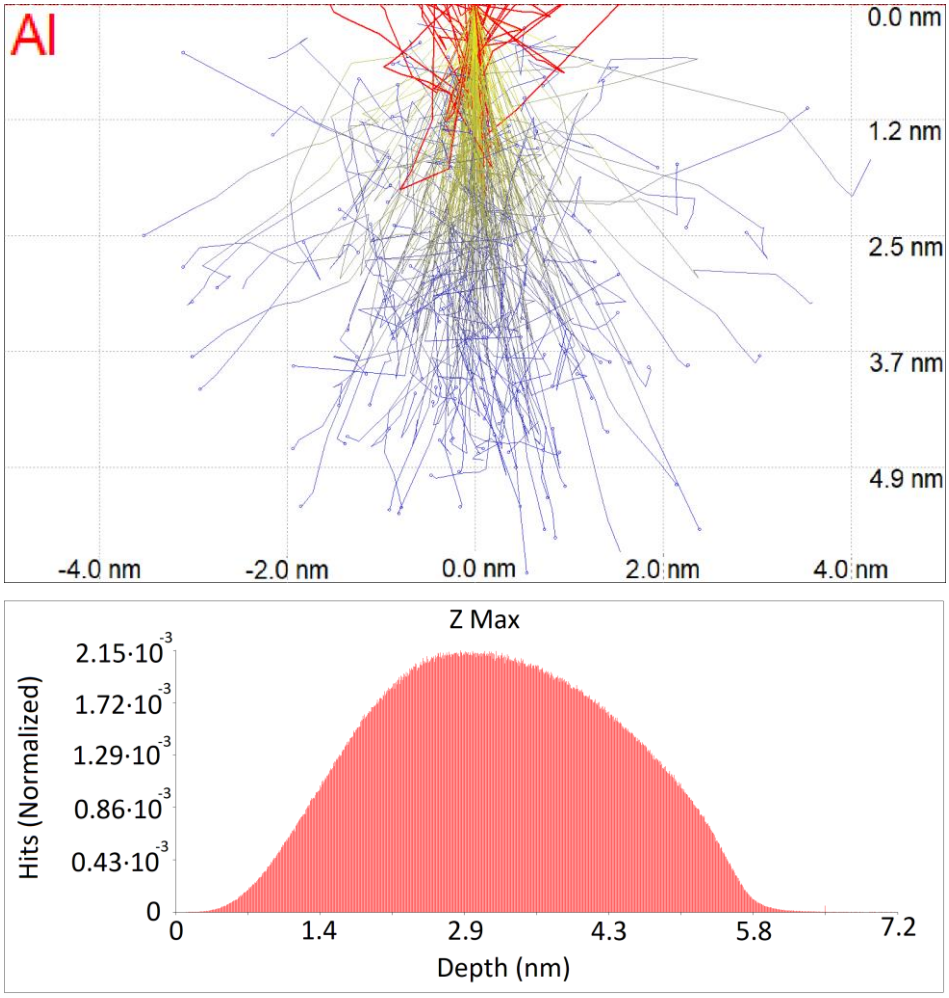

Figure 1.4. Simulation of the trajectories of the primary electrons on an aluminum sample (top) and the implantation depth (bottom). The simulation was performed in the CASINO software. The color of the PE trajectories shows their energy, starting at 300 eV (yellow) and finishing at 0 eV (blue). Trajectories of backscattered electrons are remarked by red lines.

Based on the results of [28] and [33], the penetration depth in the energy range used in this thesis 0 - 1000 eV is expected to be between 0.1 nm and 100 nm. The minimum penetration being at ~100 eV and the maximum penetration at 1000 eV. In addition, at low energies (< 100 eV), R increases to be similar to the penetration depth of electrons of energies ~1 keV. However, it should be noticed that the estimation of R at low electron energies is yet unreliable as there exist poor agreement between experimental results, MC calculations and proposed theoretical models for IMFP at these energies [30, 34-36].

2.2.4 Production and emission of secondary electrons

Internal secondary electrons (ISE) are produced in the irradiated volume of the solid due to the surface and volume plasmons decay [37-39]. Any initial direction of motion is equally likely for these excited electrons. In terms of energy, in a conductor, ISEs can have any energy higher than zero measured from the Fermi level, E_F. On the contrary, ISEs in insulators need to gain at least the band gap energy, E_{gap}, (measured from the top of the valence band) to be promoted to the conduction band and be able to travel in the solid, see **Figure 1.5**. This produces ISEs in dielectric and conductor materials to have very different behaviors. ISEs in conductor materials interact strongly with other electrons in the solid. This interaction is mainly with other electrons in the conduction band which is very populated, i.e. there is a strong electron-electron interaction. However, in dielectric materials this interaction is extremely reduced due to the band gap. There is only a limited number of electrons that have been excited to the valence band which diminishes the electron-electron interaction. The only mechanism available for energy loss in dielectric materials are electron-phonon or electron-impurity interactions, which were also present in conductor materials. This fact strongly increases the IMFP in dielectric materials respect to conductor materials as the available mechanisms tend to be less likely than electron-electron interaction between electrons in the conduction band. Nevertheless, the available interactions in both conductor and insulators make the ISEs progressively lose energy, accumulate at the lower possible energy levels and be absorbed again in the material.

Once ISEs reach the surface of the solid, they have to overcome the potential barrier called work function, ϕ, (conductors) or electron affinity, EA, (insulators) to be emitted, see **Figure 1.5**. Therefore, any internal secondary electron with less energy than the potential barrier will not be emitted. As most ISEs have been accumulated at low energies due to energy loss, only a relatively small quantity of them will be emitted. In addition, electrons reaching the surface

in an off-normal angle will suffer refraction. Finally, note that only a fraction of ISEs will reach the surface as their motion can also take them deeper in the material [28-31, 39, 40]. The minimum energy that an emitted electron can have is zero measured from the vacuum energy level (E_{vac}), **Figure 1.5**. In this thesis, E_{vac} is the energy reference used for both primary and secondary electrons.

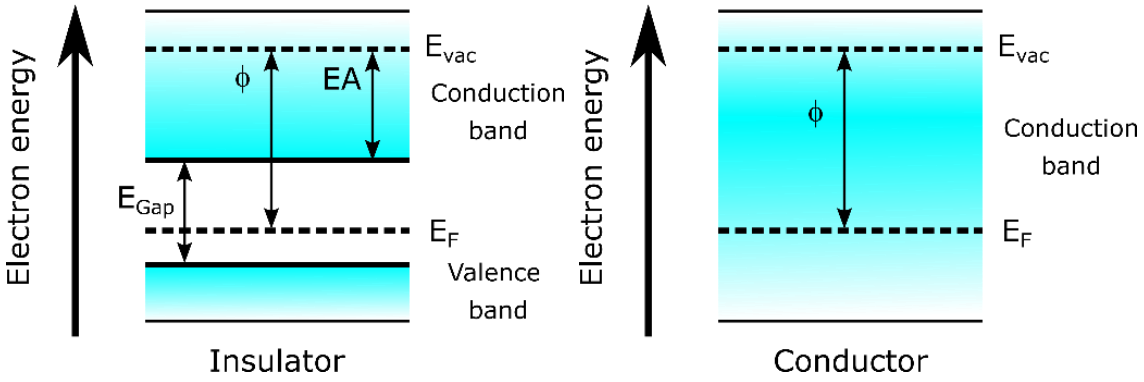

Figure 1.5. Band diagram for an insulator (left) and conductor (right) with their respective parameters. In the insulator, the valence band and the conduction band are displayed. These are separated by the energy gap, E_{Gap}. This is the energy that an electron in the solid needs to gain from the interaction with an incident electron to be excited, i.e. to be an internal secondary electron, ISE. In the case of conductor materials, any energy transference from an incident electron to an electron in the solid can produce an ISE.

In comparison, insulators will emit more SEs than conductors because the later have smallest IMFP than the former and therefore ISEs will lose energy quicker. In addition, there are insulators with very low, even negative, electron affinities. A negative electron affinity implies that most of all ISEs that reach the surface are emitted as SEs, producing very high SEYs, for example in cesiated diamonds where it gets to 130 [41-43].

2.2.5 Secondary electron escape depth

As stated before, even though secondary electrons are produced in all the irradiated volume of the solid, only those produced at a distance from where they can reach the surface will be emitted. The maximum depth normal to the surface from which secondary electrons can be extracted is called maximum escape depth, r. Obviously, the maximum escape depth matches the penetration depth, R, of low energy incident electrons.

In addition to the maximum escape depth, the mean escape depth (λ) can be defined. It is defined as the average depth normal to the surface from which secondary electrons are extracted. If elastic scattering is neglected, the mean escape depth is given by the IMFP and an exponential decay can be assumed for the escape probability of SE at a distance x from the surface, $e^{-x/\lambda}$, where λ is the mean escape depth. λ has been measured to be ~1 nm for metals and ~10 nm for electrical insulators [1]. The difference between the escape depth of metal and insulators is produced by the different IMFP of these materials, as previously discussed. In [1] the relation between maximum escape depth and mean escape depth r ~ 5 λ is given.

However, an exponential decay for the escape probability of SE can only be assumed if the elastic scattering is neglected. This is not the general case as the elastic scattering plays an important role in the transport of electrons (the elastic scattering modifies the direction of motion). Therefore, a mathematical description of the relationship between r and the IMFP is not straightforward once the elastic scattering is taken into account as has been shown in several works [44-48]. Note that these works deal with XPS and AES analysis and therefore they define the mean free path for those SE that do not suffer any inelastic scattering event. Nevertheless, the fact that λ is reduced by the effect of the elastic scattering can be applied to the present discussion.

2.3 Secondary Electron Emission properties

2.3.1 Secondary emission yield, SEY

The Secondary Emission Yield, SEY, is the main parameter in SEE characterization. The SEY, usually denoted by σ, is the ratio of the number of secondary electrons (SE) to the incident or primary electrons (PE) on a material, **Equation** 1.2:

$$\sigma(E_P, \theta) = {}^{N_{Sec}(E_P,\theta)}/_{N_{inc}} \qquad (1.2)$$

Where N_{sec} is the number of secondary emitted electrons, N_{inc} the number of incident electrons, E_P is the energy of the incident electrons (primary energy) and θ the angle of incidence of primary electrons relative to the normal. The energy, E_P, and the angle of incidence, θ, are the main dependences of the SEY.

Similar to the SEY definition, true secondary electron yield and backscattered electron yield can be defined as the ratio of true secondary electrons to incident electrons and the ratio of backscattered electrons to incident electrons respectively. The three yields are related and fulfill:

$$\sigma = \delta + \eta \tag{1.3}$$

Where δ is the true secondary electron yield and η the backscattered electron yield. The dependence of η with Z, the atomic number, is shown in **Figure 1.6**. It can be seen that η monotonically increases with the atomic number. Similarly, the backscattered electron yield can be divided into elastic backscatter emission yield, η_e, and inelastic backscatter electron yield, η_i.

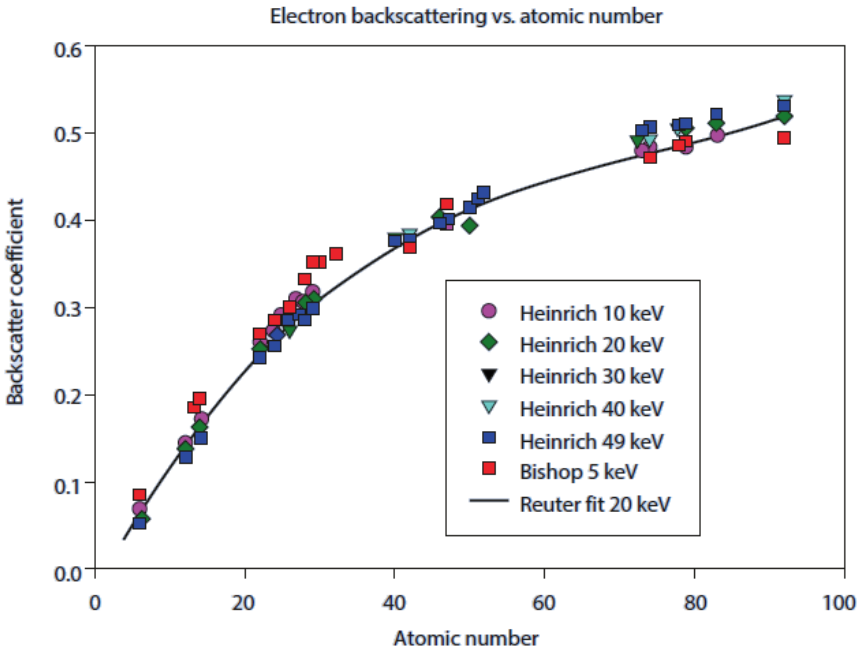

Figure 1.6. The backscattered electron yield (η) as a function of the atomic number at several incident energies. Figure extracted from [29].

2.3.2 SEY dependence on the primary electron energy

At normal incidence, the SEY as a function of E_P, or SEY curve, is defined by four parameters: the maximum SEY, SEY_{max}, the primary energy associated to this value, E_{max}, and the first and second cross-over energies, E_1 and E_2, defined as the energies at which SEY = 1, see **Figure**

1.7. The E_1 and E_2 cross-over energies are characteristic because it is fulfilled that the number of incident electrons equals the number of outgoing electrons.

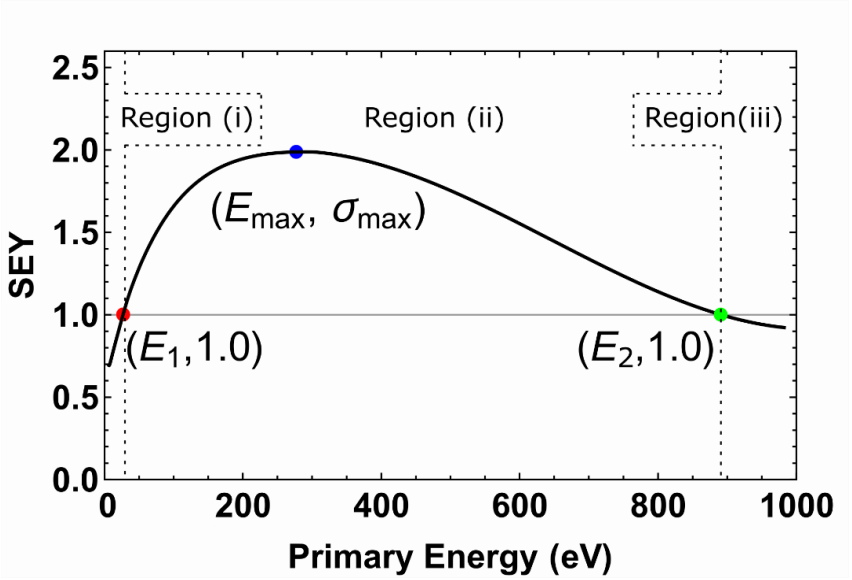

Figure 1.7. SEY as a function of the primary energy (SEY curve). The main SEY parameters are displayed. SEY_{max} and E_{max}, the maximum value of SEY and the corresponding energy, are marked in blue. The first cross-over energy, E_1, (minimum energy at which SEY = 1) is marked in red. The second cross-over energy, E_2, (maximum energy at which SEY = 1) is shown in green. The first and second cross-over energies mark three distinctive regions. Region (i) where SEY < 1, region (ii) where SEY > 1 and Region (iii) where SEY < 1 again.

Three regions can be discriminated attending to the E_1 and E_2 parameters (SEY = 1):

- Region (i), $E_P < E_1$: PE do not have enough energy to excite a considerable amount of SE, therefore the number of SE is smaller than the number PE and SEY < 1.
- Region (ii), $E_1 < E_P < E_2$: In this region, as the energy of the primary electrons increases the production of ISE per PE also increases. However, when the primary energy increases further part of their energy is deposited too deep in the material for some ISEs to be able to reach the surface and the SEY starts to decrease. This means that the penetration range of the primary electrons is bigger than the mean escape depth of the secondary electrons. The value of the penetration range at which the maximum value of the SEY occurs is at $R \sim \lambda$ [31]. The SEY curve achieves its maximum usually at primary energies 100 - 1000 eV.

Most technological materials exhibit this region and is in minimizing this region where efforts are focused when diminishing the SEY of materials. This can be achieved by increasing E_1, decreasing E_2 or reducing SEY_{max}.

- Region (iii), $E_2 < E_p$: In this region, more ISE are produced than in the regions (i) and (ii). However, the energy of the PEs is so high that it is deposited too deep in the solid. As R > r, most of the ISE are produced deep in the solid and they lose their energy before reaching the surface producing SEY < 1 in this region.

2.3.3 Models of Secondary Emission Yield

Semiempirical theories of secondary emission commonly assume that the secondary emission yield may be written as **Equation** 1.4:

$$\sigma(E_P) = \int_0^\infty n(x, E_P) \cdot f(x) dx \tag{1.4}$$

Where $n(x,E_P)dx$ is the number of internal secondary electrons produced per incident primary electron of energy E_P in a layer of thickness dx at a depth x below the surface and $f(x)$ the probability that an internal secondary electron produced at x arrives at the surface and is emitted. In $f(x)$ are included the elastic and inelastic scattering that ISE suffer in the solid, the isotropic generation of ISE and the fact that the work function barrier has to be overcame before being emitted. The function $n(x,E_P)dx$ expresses the interaction of the primary electrons with the solid, their energy loss as a function of the penetration depth, their absorption and their elastic and inelastic scattering.

2.3.3.1 Baroody model

Baroody [49] extending on the work of Bruining [50] was the first to observe and propose a universal curve for the SEY as a function of the primary energy E_P. Assuming that $n(x,E_P)dx$ is proportional to the energy loss of the primary electrons per unit path length

$$n(x, E_P) = -\frac{1}{\zeta}\frac{dE}{dx} \tag{1.5}$$

Where ζ is the energy required to excite one internal secondary electron. The probability of emission of a secondary electron produced at a depth x follows:

$$f(x) = B \cdot \exp\left(-\frac{x}{\lambda}\right) \tag{1.6}$$

where λ is the mean escape depth of the SE and *B* the escape probability once the electron reaches the surface.

The energy deposited per unit path length by the primary electrons in the solid can be expressed by the Whiddington's law as:

$$\frac{dE}{dx} = -\frac{A}{E(x)} \tag{1.7}$$

Where *A* is a constant characteristic of the material. Integrating **Equation** 1.7 from the surface ($x = 0$ and $E(x) = E_p$), to the penetration range ($x = R$ and $E(x) = 0$), the penetration range of the primary electrons can be easily computed:

$$\int_{x=0}^{x=R} E(x) \cdot dE = \int_{x=0}^{x=R} -A \cdot dx - \qquad R = \frac{E_P^2}{2A} \tag{1.8}$$

Putting everything together in **Equation** 1.4 with $E(x) = (E_P^2 - 2Ax)^{1/2}$ obtained from **Equation** 1.7:

$$\sigma(E_P) = \frac{B}{\zeta} \cdot A \int_0^R \frac{1}{(E_P^2 - 2Ax)^{\frac{1}{2}}} \cdot \mathrm{e}^{-\frac{x}{\lambda}} dx \tag{1.9}$$

Performing the change of variable $x = \frac{E_P^2 - 2A\lambda y^2}{2A}$, **Equation** 1.9 yields:

$$\sigma(E_P) = \frac{B}{\zeta} A' e^{-\left(\frac{E_P}{A'}\right)^2} \int_0^{\frac{E_P}{A'}} \mathrm{e}^{y^2}\, dy = \frac{B}{\zeta} A' F\left(\frac{E_P}{A'}\right) \tag{1.10}$$

With $A' = (2A\lambda)^{1/2}$ and

$$F(r) = e^{-r^2} \int_0^r e^{y^2} dy \tag{1.11}$$

With $r = E_P/A'$. The parameters *A, B*, ζ and λ depend on the material irradiated but Baroody showed that they could be eliminated by normalizing the SEY by SEY_{max} and E_P by E_{max}. For that the maximum value of the SEY as a function of E_p is computed:

$$\frac{\partial \sigma(E_P)}{\partial E_P} = \frac{B}{\zeta}\left(1 - \frac{2E_P}{A'} e^{-\left(\frac{E_P}{A'}\right)^2} \int_0^{\frac{E_P}{A'}} \mathrm{e}^{y^2}\, dy\right) = 0 \tag{1.12}$$

Which is only fulfilled when $r = E_P/A' = 0.92$. As the derivative is evaluated at the maximum $A' = E_{max}/0.92$ is obtained. Therefore:

$$\frac{\sigma(E_P)}{\sigma_{max}} = \frac{F\left(\frac{E_P}{A'}\right)}{F(0.92)} = 1.85 \cdot F\left(\frac{0.92E_P}{E_{max}}\right) \quad (1.13)$$

This curve does not fit entirely well the data but it does represent the universal behavior of the SEY increasing at low energies and decreasing after a critical energy (E_{max}).

2.3.3.2 Lye and Dekker model

Lye and Dekker [51] based on measurements for the electron penetration range that differed from the one predicted by the Whiddington's law, proposed two different energy loss mechanics. The first one was to use a generalized power law for the energy loss as:

$$\frac{dE}{dx} = -\frac{A}{E^n(x)} \quad (1.14)$$

With $n > 0$. The parameter n gave better agreement for the penetration depth at n = 0.35. By a similar computation to the one performed above, the obtained universal curve was:

$$\frac{\sigma(E_P)}{\sigma_{max}} = \frac{F_n\left(\frac{r_m E_P}{E_{max}}\right)}{F_n(r_m)} = (n+1) \cdot r_m^n \cdot F_n\left(\frac{r_m E_P}{E_{max}}\right) \quad (1.15)$$

Where r_m^n is the value or r at which $F_n(r)$ is maximum (similar to the value of 0.92 found by Baroody) and

$$F_n(r) = e^{-r^{n+1}} \int_0^r e^{y^{n+1}} dy \quad (1.16)$$

However, they remarked that for **Equation** 1.7 as well as for Whiddington's law the electron penetration depth was equal for all the primary electrons. This was against experiments, which showed that the number of electrons in a beam traveling in the solid decreased linearly with the depth. Thus the elastic scattering of the primary electrons should be taken into account. They concluded that a better approximation was to assume that the energy losses are constant over the entire primary electron path:

$$\frac{dE}{dx} = -\frac{E_P}{R(E_P)} \quad (1.17)$$

Using a range-energy relation in the form $R(E_P) = C \cdot E_P^{n+1}$, with C a constant, gives the universal curve:

$$\frac{\sigma(E_P)}{\sigma_{max}} = \frac{G_n\left(\frac{r_m E_P}{E_{max}}\right)}{G_n(z_m)} \quad (1.18)$$

With r_m the value for which $G_n(r)$ is maximum and:

$$G_n(r) = \frac{1 - e^{-r^{n+1}}}{r^n} \tag{1.19}$$

This model is particularly simple as $G_n(r)$ can be obtained in a closed form (see **Equation** 1.19) in opposition to F(r) or $F_n(r)$ that can only be expressed in integral form (see **Equation** 1.11 and **Equation** 1.16 respectively).

2.3.3.3 Dyonne model

Dyonne [52, 53] developed his model putting especial emphasis in the physical parameters. He also proposed a three dimensional model by adding the elastic scattering to the diffusion of the internal secondary electrons. This is done by modifying **Equation** 1.6 for the electron transport and letting the electrons disperse in a 4π angle at each depth *x*.

$$f(x) = B \cdot \int_0^{2\pi} \int_0^{\frac{\pi}{2}} \frac{e^{-\frac{l}{\lambda}} \sin\theta}{4\pi} d\theta \, d\phi = \frac{B}{2} \int_1^{\infty} \frac{e^{-x \cdot \frac{|z|}{\lambda}}}{z^2} dz \tag{1.20}$$

Where l makes reference to the three dimensionality of the model and fulfills $l = |x/\cos\theta|$ and $z = \cos^{-1}\theta$ is a change of variable to simplify the integration.

Which gives a universal curve for a power law energy loss:

$$\frac{\sigma(E_P)}{\sigma_{max}} = \frac{D_n\left(\frac{r_m E_P}{E_{max}}\right)}{D_n(r_m)} \tag{1.21}$$

With $D_n(r)$:

$$D_n(r) = \int_1^{\infty} dz \frac{e^{-r^{n+1}|z|}}{z^2} \int_0^{r} e^{y^{n+1}} dy \tag{1.22}$$

He also obtained the universal curve for a constant energy loss using **Equation** 1.17 instead of the **Equation** 1.14 used to obtain **Equation** 1.21.

It is worth discussing that Dionne not only found equations for the universal curve but for the actual SEY curves of the materials, trying to relate the solid and surface properties to the SEY_{max}, E_{max}, E_1 and E_2 values. He related the parameters *A, B*, ζ and λ with physical properties of conductors, semiconductors and insulators. *A* being the primary electron absorption constant, represents the electron stopping power of the solid and therefore is proportional to the density of the material. It is therefore inversely proportional to the penetration depth of the

primary electrons. The parameter *B* represents the probability of an electron being emitted once it reaches the surface and depends on the surface properties. ζ represents the energy that the internal secondary electrons obtain from the primary electrons. It needs to be bigger than the work function in metals and the sum of the affinity and bandgap for insulators and semiconductors. Finally, λ is directly the mean secondary electron escape depth.

In the previous discussion on the Baroody model (similarly applies with slight variations to the other models), it has been found that:

$$SEY_{max} \propto \frac{B}{\zeta}(2A\lambda)^{1/2} \tag{1.23}$$

$$E_{max} \propto (2A\lambda)^{1/2} \tag{1.24}$$

Therefore, the SEY_{max} increases with the escape probability, density, secondary electron escape depth and decreases with the work function. In the case of insulators, the bandgap plays a double role through ζ and λ. However, looking at the experimental measurements it can be seen that the bandgap increases the SEY. The E_{max} will be bigger with the density and the secondary electron escape depth.

Equation 1.23 and **Equation** 1.24 agree with the theory introduced in **Section 2.2**, where the SEY was related to the penetration range of the primary electrons and the escape depth of the secondary electrons. As the penetration range is inversely proportional to the electron absorption constant ($R \sim A^{-1}$) we have that both SEY_{max} and E_{max} are proportional to λ and inversely proportional to R:

$$SEY_{max} \propto (A \cdot \lambda)^{1/2} = (\lambda/R)^{1/2} \tag{1.25}$$

$$E_{max} \propto (\lambda/R)^{1/2} \tag{1.26}$$

Therefore, the semiempirical models support the fact introduced in **Section 2.3.2** that E_{max} is achieved when $R \sim \lambda$. The models also support the fact that a bigger λ produces a higher SEY introduced in **Section 2.2.4**.

2.3.3.4 Other SEY models

Other SEY models have also been proposed. Some of them, as the Kanaya model [54, 55] proposes a new formula for the penetration range derived from the atomic model. The Vaughan model [6, 56] proposes a simple empirical formula that may be valuable to estate explicitly due to its simplicity:

$$\frac{\sigma(E_P)}{\sigma_{max}} = (\nu e^{1-\nu})^k \tag{1.27}$$

$$\nu = \frac{E_P - E_1}{E_{max} - E_1} \tag{1.28}$$

$$k = \begin{cases} 0.62, & \nu < 1 \\ 0.25, & \nu > 1 \end{cases} \tag{1.29}$$

Where υ is the energy normalized in a somewhat different way.

Furman and Pivi made a very thorough description and computational implementation of their SEY model [57]. They treated true secondary, elastically backscattered and inelastically backscattered electrons independently to compute the actual SEY. They proposed for the three contributions the following equations:

$$\eta_e(E_P) = \eta_e^{\infty} + (\eta_e^{max} - \eta_e^{\infty}) \cdot e^{-\frac{|E_P - E_e^{max}|^p}{a}} \tag{1.30}$$

$$\eta_i(E_P) = \eta_i^{\infty}\left(1 - e^{-(E_P/E_r)^r}\right) \tag{1.31}$$

$$\delta(E_P) = \delta^{max} F\left(\frac{E_P}{E_\delta^{max}}\right) \tag{1.32}$$

$$F(x) = \frac{sx}{s - 1 + x^s} \tag{1.33}$$

Where η_e, η_i and δ are the elastic, inelastic and true secondary emission yields introduced in **Section 2.3.1**. The other are free parameters of the model. The elastic, inelastic and true secondary emission yields fulfill:

$$\sigma = \eta_e + \eta_i + \delta \tag{1.34}$$

The different electron yields from the fit to copper data computed with the Furman and Pivi model in [57] is shown in **Figure 1.8**. It can be seen that $\eta_e + \eta_i$ is essentially constant for all the primary electron energies, this is true for most of the materials. In order to compare the different models that have been presented in the discussion, they have been drawn together in **Figure 1.9**.

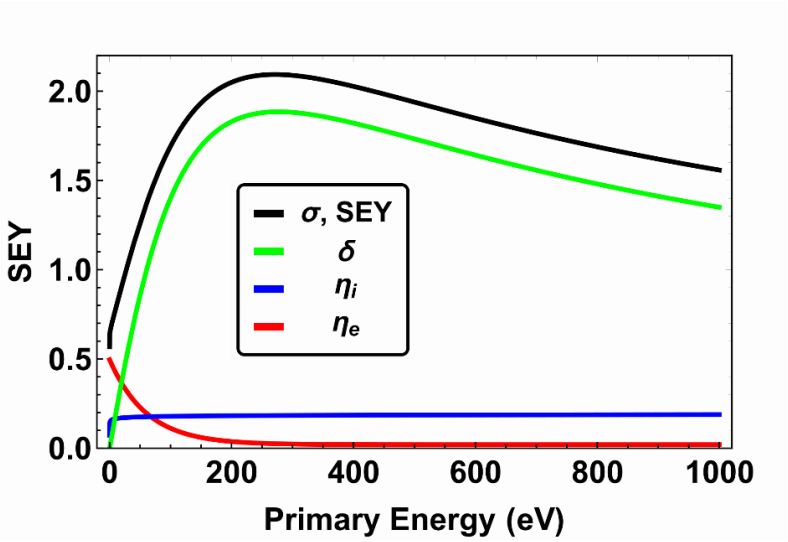

Figure 1.8. SEY curves of copper and the different contributions of elastically backscattered (η_e), inelastically backscattered (η_i) and true secondary electrons yield (δ) as a function of the energy following the Furman and Pivi model. The actual values for the parameters of **Equations** 1.30-1.34 are extracted from [57]. It can be seen that the sum of the inelastic and elastic component is essentially constant through the displayed energy range.

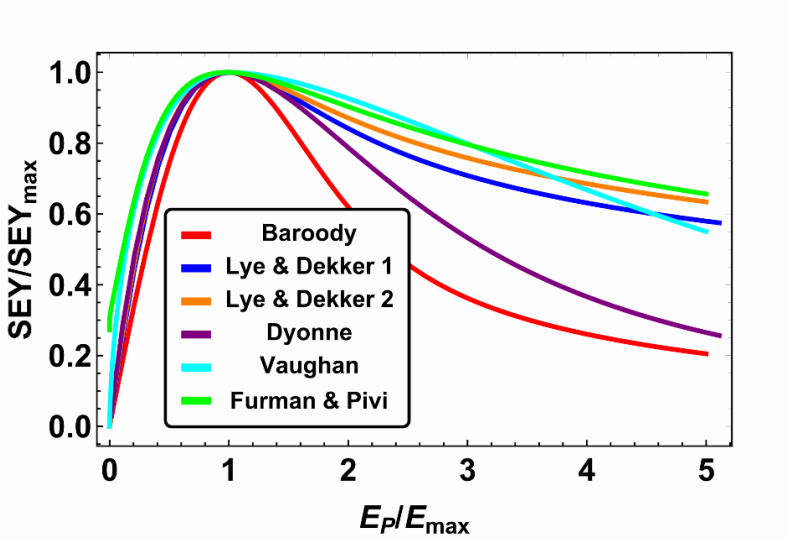

Figure 1.9. Universal curve predicted by the different discussed models. The Furman and Pivi curve is based on the normalization of the curve presented in **Figure 1.8**.

We can observe that these models predict very different behaviors at energies higher than E_{max}. The Baroody equation has a sharper shape that contrast with the smoother shape of the Furman and Pivi model. Furman and Pivi model can usually fit better the SEY experimental measurements, mainly due to being a complex model with a high number of parameters.

2.3.4 SEY dependence on incident angle

As we have seen in **Section 2.3.2**, the SEY depends on the penetration range of the incident electrons in the material. As the penetration range depends on the incident angle of the electron beam, the SEY also depends on the incident angle. Specifically, the penetration range decreases with the angle of incidence as $R(\theta) = R_{\theta=0} \cdot \cos\theta$, see top panels in **Figure 1.10**. In a flat surface, the SEY increases with the angle of incidence. Indeed, as can be seen in the top panels of **Figure 1.10**, the ratio of the volume of SE extraction region (green) to the volume of ISE production (red) is larger at oblique incident angles than at normal incidence. As the same energy is deposited closer to the surface, a greater number of excited electrons reach the surface with less energy loss and escape as SE more easily. Such enhancement of the SEY is more evident at higher incident energies. At low energies, the volumes of SE extraction and production are the same and the effect of the incident angle is more subtle [31, 58].

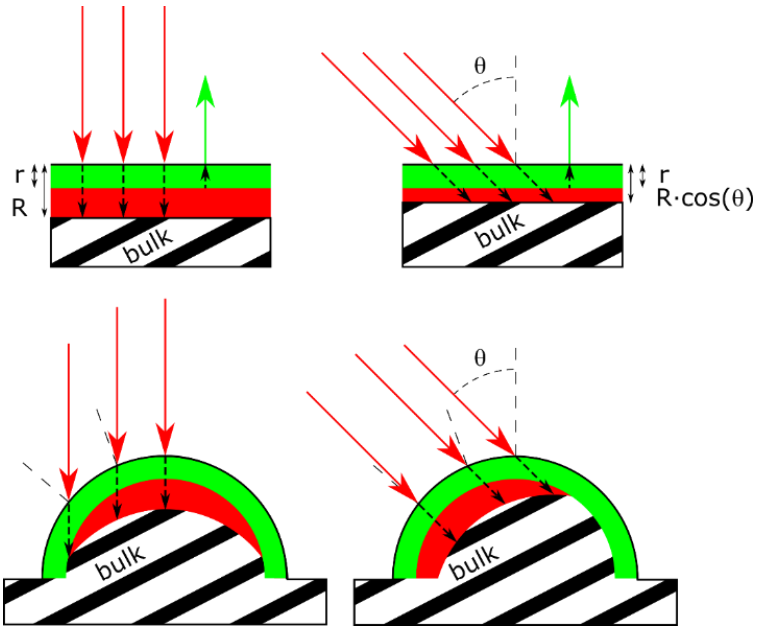

Figure 1.10. Effect of the incident angle on the SEY on flat (top panels) and rough surfaces (bottom panels). Normal incidence can be seen at the left panels and oblique incidence at the right panels. Normal direction to the surface are drawn as dashed lines. It can be seen that for a flat surface at oblique incident angles, the energy is deposited in a shallower region as the penetration depth (R) is reduced with the cosine of the angle of incidence. Therefore, more SE are extracted at oblique angles of incidence. In the case of a rough surface it can be seen how this effect is minimized and the SEY dependence on the angle of incidence is reduced.

Several models describe the dependence of the SEY with the angle of incidence. The Bruining model [50] expressed the dependence as:

$$\sigma(E,\theta) = \sigma(0)e^{C(E)\cdot(1-\cos\theta)} \tag{1.35}$$

$$E_{max}(\theta) = \frac{E_{max}(0)}{\sqrt{\cos\theta}} \tag{1.36}$$

Where C(E) depends on the energy.

Kanaya [54] described the dependence of the parameters SEY_{max} and E_{max} on the incident angle as:

$$\sigma_{max}(\theta) = \sigma_{max}(0) \cdot (\cos\theta)^{-1/n} \tag{1.37}$$

$$E_{max}(\theta) = E_{max}(0) \cdot (\cos\theta)^{-1/n} \tag{1.38}$$

Where n depends on material and ranges from 1 to 1.6.

Vaughan [6, 56] also proposed in his model an angular dependence of SEY_{max} and E_{max} as follows:

$$\sigma_{max}(\theta) = \sigma_{max}(0)(1 + k \cdot \theta^2/2\pi) \tag{1.39}$$

$$E_{max}(\theta) = E_{max}(0)(1 + k \cdot \theta^2/2\pi) \tag{1.40}$$

Where k is a "smoothness factor" for the surface, in the range from 0 for a rough surface to possibly 2 for a polished surface.

In their model, Furman and Pivi proposed for the incident angle dependence of SEY_{max} and E_{max}:

$$\sigma_{max}(\theta) = \sigma_{max}(0) \cdot [1 + a \cdot (1 - \cos^c\theta)] \tag{1.41}$$

$$E_{max}(\theta) = E_{max}(0) \cdot \left[1 + b \cdot \left(1 - \cos^d\theta\right)\right] \tag{1.42}$$

Where a, b, c and d are fitting parameters.

The models discussed can be compared in **Figure 1.11**, where bands of possible values as estimated from the different authors are presented. SEY as a function of the primary energy and the angle of incidence is displayed in **Figure 1.12**.

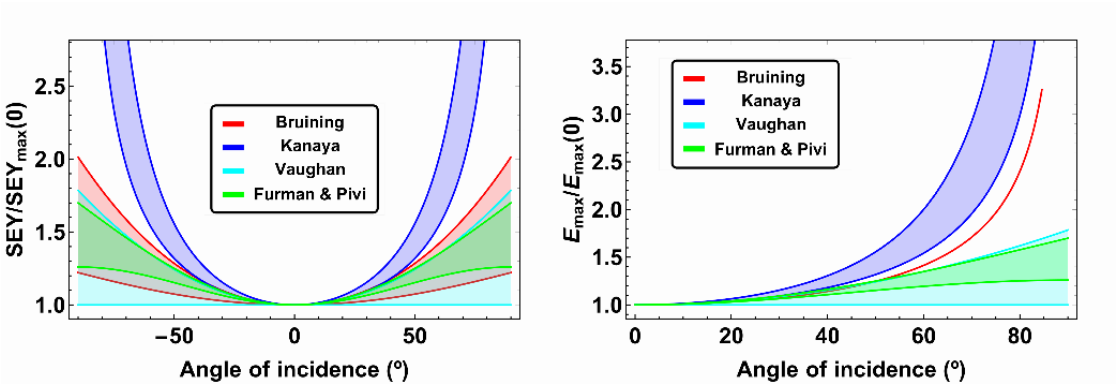

Figure 1.11. SEY_{max} (left panel) and E_{max} (right panel) dependence on the angle of incidence. Bands of possible values are displayed following the parameter values given by the respective authors in their research.

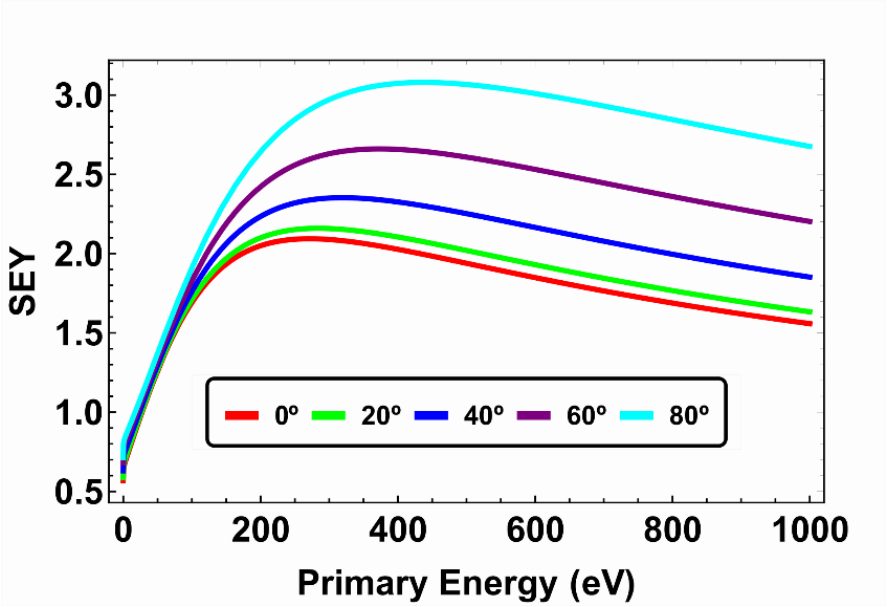

Figure 1.12. SEY of the copper sample shown in **Figure 1.8** with the incident angle dependence as predicted by the Furman and Pivi model. It can be seen that both SEY_{max} and E_{max} increase with the angle of incidence.

As can be seen explicitly in the Vaughan model, the roughness of a surface influence the dependence of the SEY with the angle of incidence. In this model, a constant $k = 0$ is proposed for very rough surfaces, which removes the angular dependence. This can be conceptually seen at the bottom panels of **Figure 1.10**. Unlike the case of a flat surface (top panels), where the ratio of volume from where SE are extracted (green) to irradiated volume (red) increases with

the angle of incidence, for rough surfaces (bottom panels) the ratio at oblique incidence is approximately equal to the ratio at normal incidence. This can be understood in the following way: in a rough surface at any incident angle there is always oblique incidence (there are multitude of normal directions that can be defined in a rough surface). Therefore, when modifying the angle of incidence the picture does not change much.

The SEY results exposed in *Publications 1, 2 and 3* of this thesis are obtained for an incident angle of 0º.

2.3.5 Energy distribution curves

In addition to the SEY curves that describe the total number of electrons emitted by the solid per incident electron, the energetic characterization of the emitted electrons is also important in the study of the SEE. A typical spectrum of SEE or energy distribution curve, EDC, can be seen in **Figure 1.13**. As previously mentioned, the emitted electrons can be divided into three groups:

- Elastically backscattered electrons. These are incident electrons that undergo elastic scattering in the solid, reach the surface and are emitted again without energy loss. The number of backscattered electrons does not depend strongly on the incident energy (see **Figure 1.8**) and increases with the atomic number, Z (see **Figure 1.6**). Elastically backscattered electrons can be seen in the EDC as a thin peak centered at E_p (shown in red in **Figure 1.13**).
- True secondary electrons. These are predominantly electrons that were initially in the solid and that are excited by the incident electrons and emitted. By convention, all electrons emitted with less than 50 eV are considered true secondary electrons [29, 59]. However, this convention only holds for primary energies higher than 100 eV as the elastic and true secondary electron population tend to overlap otherwise. True secondary electrons can be seen in the spectra at low energies as a broad peak (shown in green in **Figure 1.13**).
- Inelastically backscattered electrons. These are mainly primary electrons that undergo inelastic scattering in the solid (losing energy and exciting true secondary electrons) that eventually reach the surface and are emitted. By convention, electrons with energies between 50 eV and the energy of the peak of elastic electrons are considered

inelastically backscattered electrons. The inelastically backscattered electrons in the spectra populate the energies between the two main peaks (shown in blue in **Figure 1.13**). The Auger transition signal can be seen in this region, see **Section 2.7.6**. These electrons are produced by internal transitions of the electrons in the atoms of the irradiated material therefore, they are secondary electrons extracted from the solid. Auger transitions are produced at incident energies $E_p > 3$ keV. These transitions appear as additional peaks in the spectrum in the inelastic range. They convey the compositional and chemical state of the surface of the irradiated material.

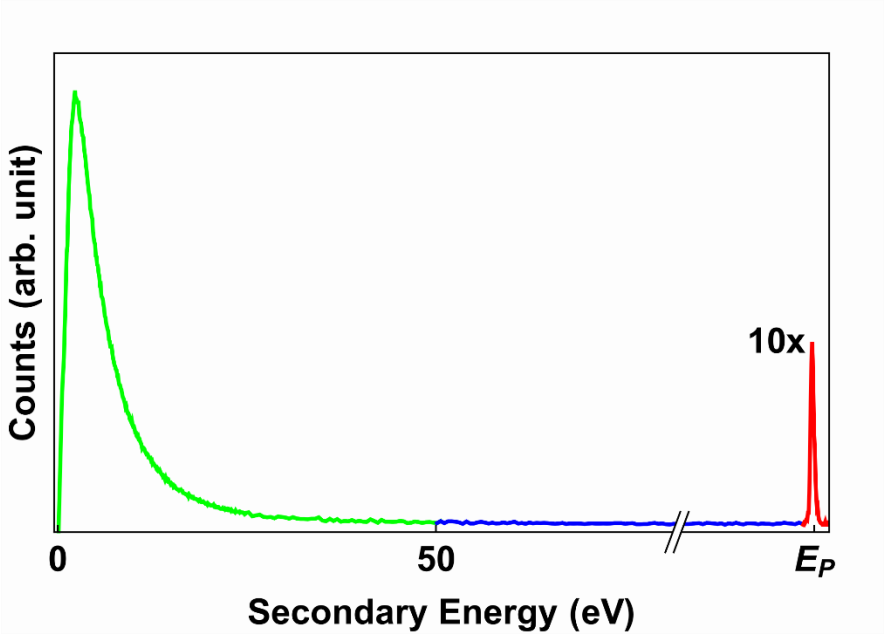

Figure 1.13. Energy spectra or energy distribution curve (EDC) of secondary electrons. All electrons emitted with less energy than 50 eV are considered true secondary electrons (green). The high energy peak, centered at the primary energy (E_P), are the elastically backscattered electrons (red). The region that expands between the two peaks are the inelastically backscattered electrons (blue).

Several formulas have been proposed to describe the true secondary electron spectra, i.e. the low energy peak of the spectra. Two of them were chosen to describe the EDC of the secondary electrons in the three publications accompanying this doctoral thesis. The first of them was proposed by M. S. Chung and T. E. Everhart [40]. They derived **Equation** 1.43 by a phenomenological approach:

$$\frac{dN}{dE} = \rho_0 \frac{E}{(E+\phi)^4} \tag{1.43}$$

Where E is the energy of the secondary electrons, ρ_0 a normalization factor and ϕ the work function of the solid. In the case of electrical insulators ϕ is naturally replaced by the dielectric affinity, χ.

The second formula of the spectra of true secondary electrons used throughout this doctoral thesis is based on an empiric approach [60], **Equation** 1.44:

$$\frac{dN}{dE} = \rho_0 \exp\left(\left(Ln\frac{E}{E_0}\right)^2 / 2\tau^2\right) \quad (1.44)$$

Where E is again the energy of the secondary electrons, ρ_0 a normalization factor, E_0 the position of the peak and τ a parameter controlling the raise and decay of the distribution. This equation decouples the width of the distribution and the position of the peak which might be preferable. This is done by using two parameters (E_0 and τ) instead of one (ϕ) as in **Equation** 1.43.

In this thesis, a method was devised to measure the energies of the true secondary electrons, i.e. the EDC at low energies. This region of the spectrum is extremely valuable as most of the emitted secondary electrons are found in this region. Of particular interest is the peak position, which corresponds to the most likely electron emission energy, and the width of the peak. The method was introduced and tested on materials with known EDC in *Publication 2* and applied to dielectric materials in *Publication 3.* Its application in dielectric materials is of particular interest due to the difficulties in characterizing their energy spectra by conventional methods. These difficulties reside mainly in the charging of the dielectric material under the incident radiation, which might distort the energy of the secondary electrons if acquired by conventional energy analyzers.

2.3.6 Angular distribution of secondary electrons

Secondary electrons are emitted in different angles. The distribution of true secondary electrons follows approximately a cosine distribution independently of the incident angle of the primary electrons, whereas the backscattered electrons tend to follow a specular distribution and therefore have a strong influence of the angle of incidence, see **Figure 1.14** [29, 50, 61, 62].

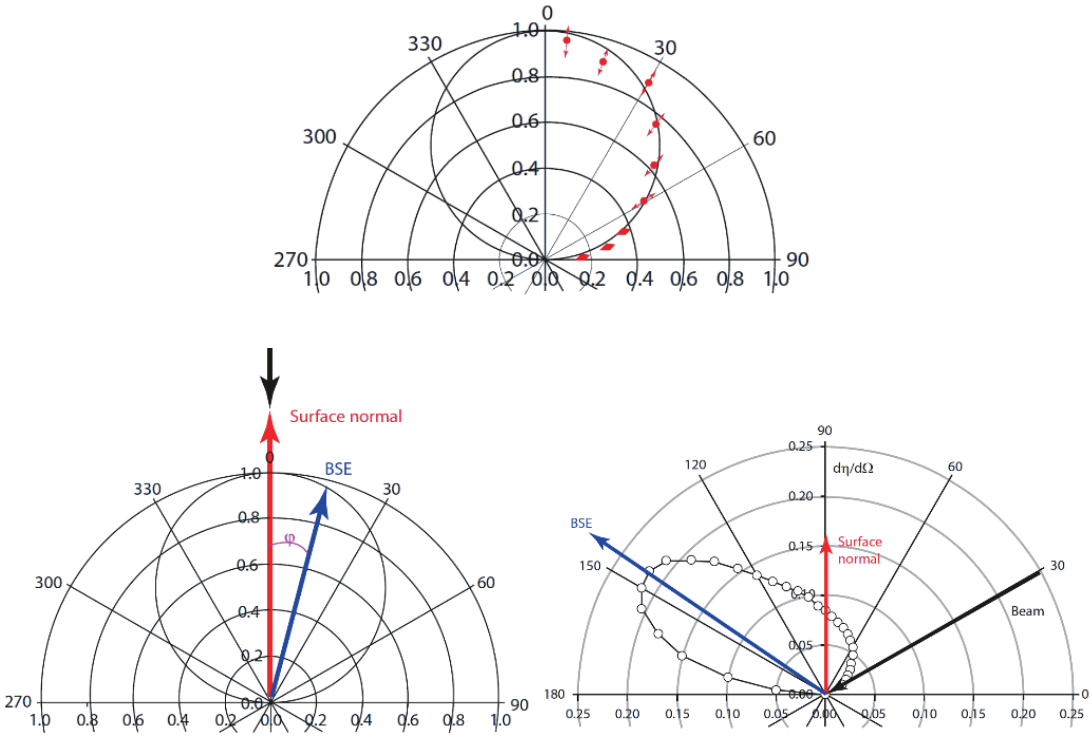

Figure 1.14.. Angular distribution of the true secondary electrons (top) and backscattered electrons (bottom) are displayed. Top panel, it can be seen that the angular distribution of SE follows a cosine distribution. Bottom panel, the emission of backscattered electrons depends strongly on the angle of incidence. Figures extracted from [29].

2.3.7 Effects of exposure to air and conditioning on SEY

Air exposure has been shown to increase SEY of metals from their nominal values, approximately in the range 1 – 2, to values over 3. This is mainly due to the interaction of the surface with the air producing the oxidation of the metallic surface. In most cases, as the metal oxide that develops is an insulator, the SEY of the oxidized metal is higher than the SEY of the clean metal. A layer of organic surface contamination is also usually found after exposure to air, this layer also contributes to increase further the SEY [63-68]. This effect can be masked if a high dose is used in the SEY characterization due to a charging effect.

One of the discussed methods to decrease the SEY on **Section 2.4** is the deposition on the surface of a low SEY carbon layer. This can be done by irradiating the surface with a high electron beam current (at doses over 10 $\mu C/mm^2$). This technique is called surface conditioning by electron bombardment or scrubbing. In this process, the organic contaminants present on the irradiated surface decompose and rearrange in graphitic assemblies while the volatile

compounds desorb from the surface. In addition, the carbon present in carbon molecules in the residual pressure of the vacuum chamber can be dissociated and adhered to the surface by this method. Heating seems to produce a similar effect to scrubbing in breaking the bonds of the absorbed molecules and producing graphitic layers on the surface [68-75].

2.3.8 SEY dependence on surface roughness

The effect of surface roughness plays an important role on the SEY of materials. It can be intuitively seen in **Figure 1.15** that whereas in a flat surface all SE leaving the surface are emitted, in a rough surface some of the emitted SE can be trapped by the protuberances of the surface itself. See **Section 2.4** for a discussion on different methods that can be used to imprint roughness as a way to decrease the SEY.

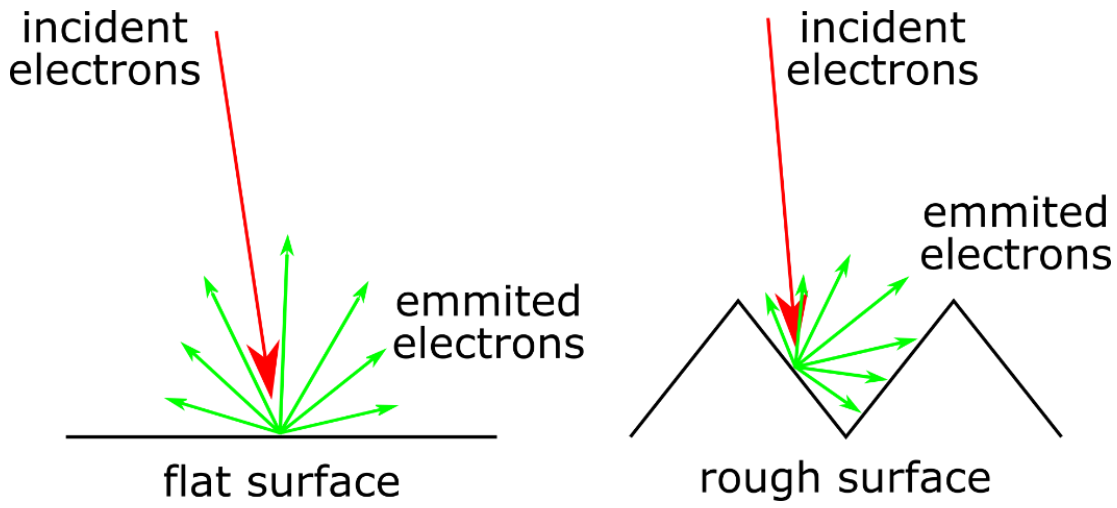

Figure 1.15. SEE dependence with the roughness of the surface. Incident electrons are drawn in red and secondary electrons in green. A flat surface is shown at the left side where all the secondary electrons are emitted. In a rough surface (shown at the right side) an important number of secondary electrons is trapped in the adjacent structures.

However, it would be wrong to assume that for SEY reduction any roughness is better than none at all. The roughness increases the angle of incidence of the primary electrons and therefore the SEY increases with it. Also, when SE impact with the surface second generation of SE will be produced. As the energies of most of the SE are small the SEY of this second order interaction will be smaller than the first generation of SE. Further generations of ever decreasing numbers of SE are produced subsequently each time SE impact with the surface. In

summary, not any roughness can be used to decrease the SEY. At the very least, the roughness of a surface has to be enough to overcompensate the increased SEY due to the increased angle of incidence on the surface and the subsequent generations of SE.

2.3.9 SEY examples

Figure 1.16 shows the SEY curves of three polymers, Kapton, Teflon and Ultem, which are relevant in the space industry [76-79]. These materials are insulators, the SEY measurement method used to measure them is introduced in **Section 2.7.2**. The SEY parameters of these SEY curves are shown in **Table 1.1**.

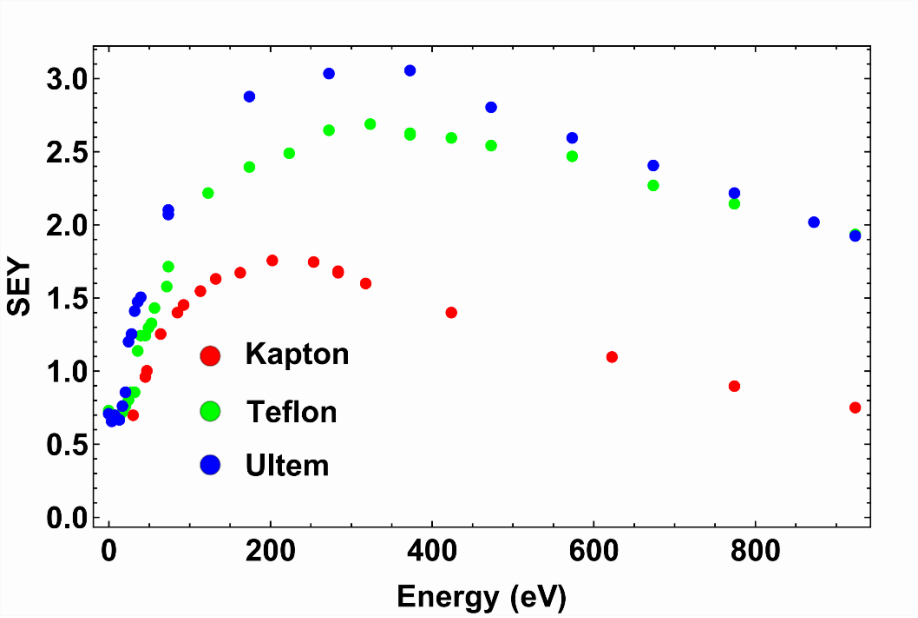

Figure 1.16. SEY of three different dielectric materials: Kapton, Teflon and Ultem. These measurements were acquired as part of the research in this doctoral thesis.

Table 1.1. SEY parameters of the Kapton, Teflon and Ultem samples.

	E_1 (eV)	E_{max} (eV)	SEY_{max}
Kapton	48	200	1.76
Teflon	33	303	2.66
Ultem	21	259	3.13

2.4 Secondary Emission Yield reduction

Technological surfaces such as those used in inner walls of RF components in satellites, particle accelerators or plasma devices usually present SEYs higher than desired for their optimal performance. For example, Alodine coatings in satellites components have been usually used to reduce the corrosion effects of reactive atmospheres were satellites are stored before their commissioning. This coating is now being replaced by Bonderite or Surtec as Alodine has been ruled out due to having the carcinogenic component Cr^{+6} [80]. Both of them present the same issue, a high SEY that prevents their use in certain applications. Therefore, different ways to decrease their SEY or alternative coatings are actively sought. Also, inner chambers of accelerator facilities, such as the Large Hadron Collider (LHC), are made of aluminum, copper or stainless steel. These materials have again a SEY too high (>2) and their SEY needs to be decreased for certain applications.

Part of the work exposed in this thesis has been devoted to study new ways of decreasing the SEY of materials. Usually, two main ways for decreasing the SEY have been used: (i) low SEY materials can be used to coat the relevant surfaces where high SEY is to be avoided or (ii) the roughness of these surfaces can be increased. An study of all these methods can be found in the theses developed previously in our research group [81-83].

Low secondary emission yield materials are for example TiN [84-88], TiZrV [87-89], carbon nitride [90], amorphous carbon [69, 74, 75, 91-94], graphene [95, 96] and velvet structures such as CuO [97-100]. Specifically, TiN, TiZrV and amorphous carbon have been the preferred coating materials for the specific areas were low SEY is needed in particle accelerators. Also, velvet structures have been recently tested for Hall Thrusters with promising results [101].

In fact, roughness is a main factor behind the low SEY of some materials used to coat surfaces such as amorphous carbon or velvet structures. Indeed, as roughness is a key factor governing the SEY of all surfaces, it has been thoroughly studied theoretically and computationally the last years [102-113]. Therefore, instead of treating surfaces with low SEY coatings, the surface roughness of the materials themselves can be modified to reduce their SEY. For this purpose, surfaces can be roughened by physical and chemical methods. The surfaces can be covered by physical vapor deposition (PVD) [113, 114], ablated by laser [115-118], ion beam irradiated [119-124], by photolithography [112] or using a chemical method [81, 125-127] to generate roughness in the surface by eroding or growing structures. For example, laser treated surfaces have recently attracted attention in particle accelerators [128, 129]. The chemical method

attains better coverage results as there are no shadow effects in the surface due to the directionality of the irradiation source (light, ion beam or particles) inherent in the other methods. An example of the finishing of the chemical method can be seen in **Figure 1.17**. For a more in depth explanation of the role of roughness on the reduction of SEY, refer to S**ection 2.3.8**.

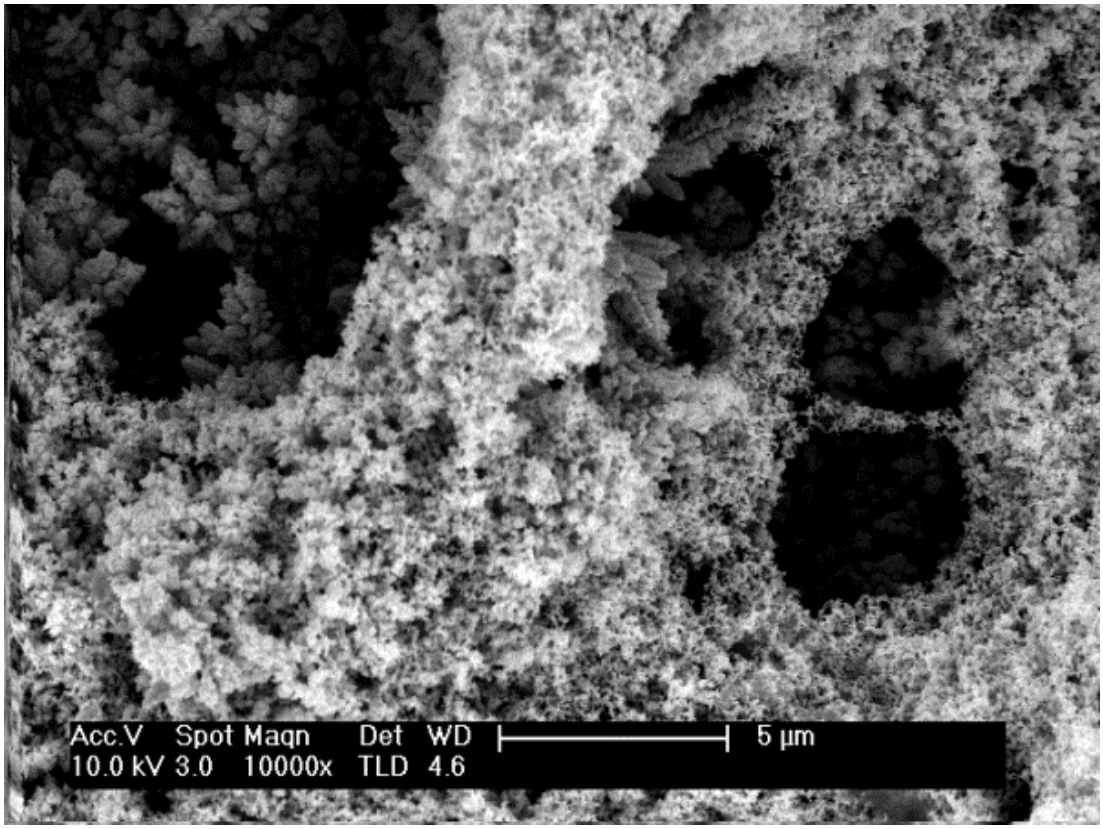

Figure 1.17. SEM image of a rough silver coating deposited on aluminum by a chemical method at ICMM-CSIC. This coating achieved a SEY < 1, key to avoid Multipactor discharge.

A novel alternative is proposed in *Publication 1*. In this work, a novel concept to diminish SEY was developed. Composite materials with conductor and dielectric domains were found to exhibit an unusually low SEY. This was due to the dielectric domains charging under electron irradiation which generated local electric fields between dielectric and conductor domains that were enough to trap an important fraction of secondary emitted electrons.

2.5 Electrical insulators

2.5.1 SEE and charging of electrical insulators

SEE and charging are at the core of the effects described in the three publications accompanying this thesis. Charging is generally considered an unwanted phenomenon as it can lead, for example, to high-powered discharges between different electronic components, **Section 2.6.1**. It can also dramatically affect the nature of the SEE properties of the surface, hindering the characterization of these materials. Charging modifies the total number of emitted electrons, the energy of primary and secondary electrons and their outgoing directions. In *Publication 1*, the effect of combining metal and dielectric domains on the surface of a composite material is studied. It was concluded, that the differential charging between the different domains can extremely reduce the SEY of the surface of the composite. The local electric fields between domains drive the secondary electrons towards the surface, inhibiting their emission. In *Publication 2* and *Publication 3*, the reduction of the emission of electrons due to a homogenous surface charging is studied. A method is proposed to couple the reduction of the number of emitted secondary electrons to the positive voltage arising on the surface and obtain the energy of the emitted secondary electrons. The positive potential in the surface inhibits the emission of the SE emitted with less energy than the arising potential barrier.

The charging behavior in dielectrics is mainly dictated by the magnitude of the SEY, the incident penetration range (R) and the maximum escape depth of the secondary electrons (r). Two charging regimes can be distinguished according to the sign of the net charge accumulated in the surface of the insulator: positive charging and negative charging. These charging regimes can be approximately discussed attending to the three regions defined by SEY = 1 presented in **Section 2.3.2**:

- Region (i), $E_p < E_1$: As SEY < 1 the number of PE deposited in the solid is greater than the number of SE emitted. This implies that net negative charge is deposited on the surface of the dielectric. As r > R in this region, the PE are deposited in the same volume where the SE are extracted, therefore the deposited charge is homogeneously distributed in a thin layer of thickness equal to the incident penetration depth of the primary electrons.

  For a constant E_p, the surface will increasingly charge up to a potential $q \cdot E_P$. At this moment, all the incident electrons are deflected before hitting the surface and the charging

of the solid and emission of SE stops, see **Figure 1.18a**. Incident energies in this region are in the negative charging regime.

- Region (ii), $E_1 < E_p < E_2$: As SEY > 1 the number of emitted electrons is higher than the incident electrons. Therefore, net positive charge is expected to be deposited on the surface of the dielectric. However, according to J. Cazaux in [130-132] two different behaviors occur due to a different charge distribution in the solid. This can be discussed attending to the relation between the incident penetration range and the maximum escape depth of secondary electrons.
  - Region (ii-1) $E_1 < E_p < E'$, where E' is an energy introduced in [131] that fulfills R ~ r. Thus, in this region as in region (i), the deposited charge is homogeneously distributed in a thin layer of thickness equal to the incident penetration depth of the corresponding primary energy. E' is found to be slightly larger than E_{max} and often far smaller than E_2 ($E_{max} < E' << E_2$).

    For a constant E_p, the surface will charge positively and a positive potential acting as a retarding potential for all the secondary electrons will arise reducing their energy. The emission of the secondary electrons with less energy than the increasing potential barrier will be inhibited until the total number of outgoing electrons equals the number of incident electrons, see **Figure 1.18b**. At the steady state, SEY = 1 is achieved at an energy that should exhibit (in the uncharged state) SEY > 1. The maximum potential acquired in this region is not very high ~ 1 -10 V and depends on the SEY and the EDC of the secondary electrons. Primary energies in this region are in the positive charging regime.
  - Region (ii-2) $E' < E_p < E_2$. In this region, a unique layer of deposited charge can no longer be considered as R > r, which means that some of the primary electrons are deposited deeper than the extraction volume of SE. This implies two charge distributions in the irradiated solid: a shallow positive charge distribution (from where SEs are extracted) and a deeper negative charge distribution (where PEs are deposited). For a constant $E_p = E_2$, by definition, the number of SE equals the number of PE. Therefore, the net charge of the solid remains zero. However, as R > r at this incident energy the positive charge is accumulated in a shallower volume than the negative charge. This implies that a dipolar-like electric field arises, inside and outside the bulk, see **Figure 1.18c**. Specifically, a potential barrier appears due to the positively charged layer just over the surface. As before, the emission of low energetic electrons will be

inhibited producing a SEY slightly smaller than one (SEY < 1). Consequently, the solid will start charging negatively as the deep negative distribution increases its absolute value respect to the shallow positive layer. Note that this does not prevent the low energetic electrons from being trapped and SEY continue to be smaller than one, as the positive charge layer at the surface still exists. However, the landing electron energy will decrease and R will diminish consequently. This negative charging will continue until the landing energy equals E' (where R ~ r) and SEY = 1. At this point, the steady state is achieved and the charging stops in both net value and distribution profile.

Likewise, for a constant E_p higher than E', as the SEY > 1 the surface will charge positively and the SEY will decrease towards SEY = 1 as in region (ii-1). At this point, the total charge is constant but not the distribution of charge. As R > r the same argument as before arises to achieve the steady state.

In this region, positive and negative charging can take place. At primary energies close to E', positive charging will arise as E_p only needs to decrease slightly to reach E' and fulfill R ~ r. At primary energies close to E_2, negative charging will take place as E_p needs to be decreased more dramatically to fulfill the same condition. As a matter of fact, the boundary between the two charging regimes is yet not completely clear. This reasoning was proposed and developed by J. Cazaux in [130-132]. In addition, several models describing the charge distribution and its evolution are introduced in [133, 134].

- Region (iii), $E_2 < E_p$: In this region, SEY < 1 and the net deposited charge is negative. For a constant E_P the landing energy of the primary electrons is diminished due to the negative voltage arising on the surface, see **Figure 1.18d**. As the process continues the energy of the primary electrons is diminished until the steady state is achieved with landing energy E' and SEY = 1. Primary energies in this region are in the negative charging regime.

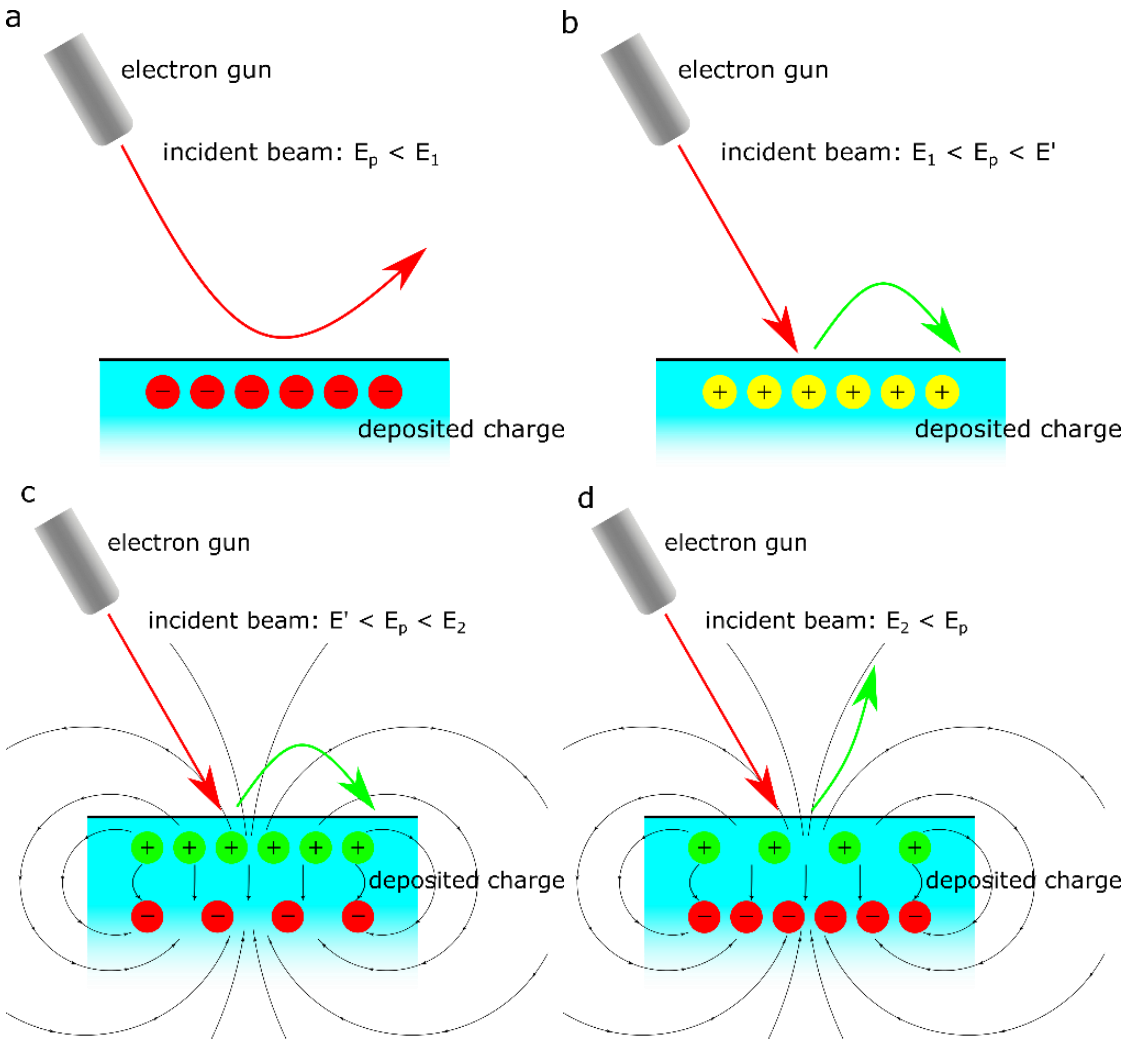

Figure 1.18. Conceptual description of the charging of an insulator during electron irradiation at different primary energies. Four distinctive charging regions are described in panels a-d, see main text. Panel a, region (i), $E_P < E_1$. Energies in this region are in the negative charging regime. A unique negative charge layer is deposited in the solid. Panel b, region (ii-1), $E_1 < E_P < E'$. Energies in this region are in the positive charging regime. A unique positive charge layer is deposited in the solid. Panel c, region (ii-2), $E' < E_P < E_2$. Two separate charge distributions arises in this region: a shallow positive charge layer and a deeper negative charge distribution. This originates a dipolar-like electric field that affects the dynamic of the evolution of charging. Panel d, region (iii), $E_2 < E_P$. Energies in this region are in the negative charging regime. Two separate charge distribution arises as in region (ii-2) and a dipolar-like field contributes to the charging dynamics.

2.5.2 Discharging mechanisms

Several charge relaxation mechanisms take place in solids, amongst them are ohmic conduction, space-charge-limited conduction and hopping charge transport [135-137]. Several of them can be present at the same time with each one having their own characteristic discharging time, the combination of which gives rise to the discharging time of the solid.

As can be seen in **Table 1.2**, characteristic discharging times of some dielectric materials can range from seconds to days. For applications where a quick discharge is needed, several methods of charge dissipation have been devised. The most remarkable of them are: heating the samples or irradiating the charged surface with low or medium energy electrons, ultraviolet radiation or positive ions [132, 138-153].

Table 1.2. Electrical properties and discharging time of Kapton, Teflon and Ultem [154-157].

	Resistivity ρ (Ω·cm)	Relative permittivity ε_r	Discharging time R·C (s)	Dielectric strength (MV/m)
Kapton	$1.4 \cdot 10^{17}$	3.5	$43 \cdot 10^3$	87-173
Teflon	$> 10^{18}$	2.1	$> 186 \cdot 10^3$	389-430
Ultem	10^{15}	2.9	257	437-565

By heating the solid [142, 145, 151, 153], the mobility of the charge carriers increases, therefore the conductivity of the dielectric increases and the discharging time decreases. Both positive and negative charge can be dissipated, as well as deep charging. The insulator can be maintained at high temperatures, usually between 200- 800 ºC or heated between subsequent measurements. However, the latter can be extremely time consuming and both might modify the sample properties. Some dielectrics, especially polymers, can have low melting points and their bulk or surface properties can be modified. Also, degasification of some of the components of the insulator can take place.

By irradiating the surface with low energy electrons [138, 139, 141, 143-149], the charge in positively charged materials can be dissipated. The low energy incident electrons are usually delivered by a flood gun. However, once the charge of the solid is dissipated, a charging process, as the one discussed in the previous **Section 2.5.1**, takes place. This charging process will leave the surface negatively charged to a few volts, equal to the energy of the low energy incident electrons. Interestingly, in [158] primary electrons with energies ~ 100 eV coupled to a positive bias in the dielectric are used to dissipate positive charge. When positively biased,

most of the secondary electrons are trapped in the potential barrier and some of the positive charge is eliminated as SEY is effectively smaller than one.

By irradiating the sample with medium energy electrons (electrons between the two cross-over energies, i.e. energies at which SEY > 1) [132, 140-142], the deposited negative charge can be dissipated. A similar discussion as in the low energy electrons applies in this case.

By irradiating the material with ultraviolet radiation [141, 142, 145, 146, 148, 150, 152], negative charges in the solid can be removed due to the photoelectric effect and photo-induced conductivity in some materials. The volume from where charge is extracted equals the penetration depth of the radiation, several nm. After using ultraviolet light to discharge a dielectric a slight positive surface voltage will be left in the solid. Usually, irradiation with ultraviolet light is coupled with low energy electron irradiation to diminish the final voltage left in the solid.

By irradiating the surface with low energy positive ions [132, 140-143], negative charge can be dissipated. There maybe two main concerns when using positive ions. The energy must be low to maintain the sputtering yield as low as possible. If a high sputtering yield is achieved the morphology and composition of the surface might change and therefore its properties. Also, the volume at which positive charge is implanted is very shallow, as the penetration range of ions is extremely smaller than the penetration depth of the primary electrons. However, this mechanism is valuable as has been demonstrated in the Environmental Scanning Electron Microscope (ESEM) [29, 159]. ESEM permits insulating as well as wet samples to be observed without prior preparation.

The use of one or other or a combination of the possible methods of charge dissipation is dictated by the characteristics of the material and the sensitivity of the measurements to a few positive or negative volts. Furthermore, deep dielectric charging, i.e. charge deposited below 10 nm deep in the material cannot be effectively removed by surface irradiation methods. If deep charging is not removed, charge builds up in the surface to compensate with the net charge approaching zero. In this case, electric fields can still remain in the insulator that can modify its properties. Sometimes, patiently waiting for the dielectric to discharge can be the best option.

2.5.3 Dielectric breakdown

There is an upper limit to the charge that can be accumulated in a dielectric. This is because, if the electric field through the insulator is high enough, a dielectric breakdown will take place. The dielectric breakdown is defined as the loss of the dielectric properties of materials as a result of the application of an electric field higher than a certain critical value. At strong electric fields, solid insulators do not obey Ohm's law and the current increases exponentially with the electric field, reaching very high magnitudes at which the material is destroyed. The electric field at which the dielectric breakdown takes place is called the dielectric strength or breakdown electric field. The dielectric strength of solids is typically over 10 MV/m and can reach values over 500 MV/m, depending on the material [157]. **Table 1.2** shows the breakdown electric field of Kapton, Teflon and Ultem.

2.6 SEE phenomena

2.6.1 Spacecraft charging

Different anomalies have been diagnosed on spacecraft, in the majority of them charging due to SEE, has been identified as the cause [160]. Anomalies can be logic errors produced by spurious signals (which might inadvertently order, for example, a change of orbit in the beginning of the space era) power system failures due to permanent damage to hardware onboard or radio interference in the communications [161]. The first noticed anomaly in spacecraft was in 1963, the cause has not yet been determined even now. The first anomaly attributed to solar or galactic cosmic radiation was in 1971 and produced a software error [160]. The first anomaly due to surface charging (caused by SEE) produced an electrostatic discharge [162] in a military communication satellite in 1973. This caused a power interruption of its communications subsystem, which produced a failure. Due to this incident a joint NASA and Air Force investigation on spacecraft charging was issued [163]. **Figure 1.19** shows an example of an electrostatic discharge in a solar panel.

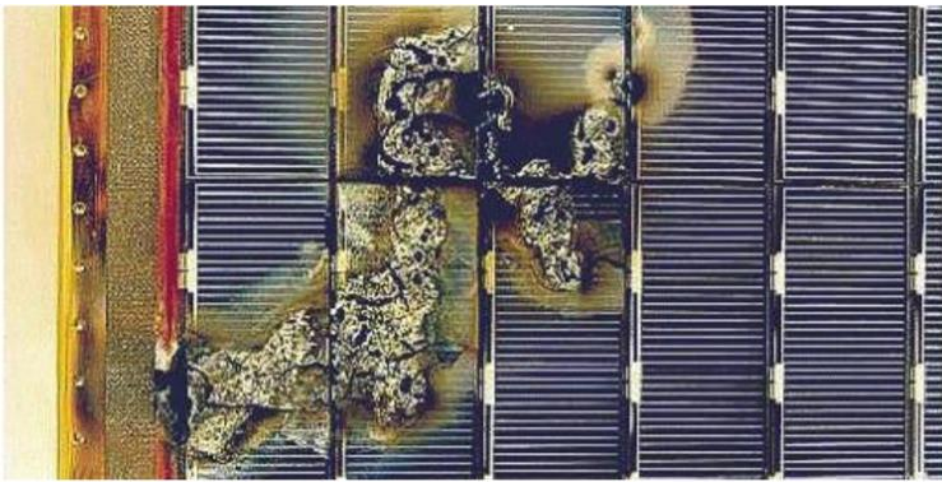

Figure 1.19. An example of the consequences of an electrostatic discharge in a solar panel. Two adjacent components with different SEY has produced an electrostatic discharge due to the potential difference between them. In this case, the arc discharge has damaged and destroyed part of a solar panel array. Credit: ESA.

The first generation of satellites packed big and simple electronics that made them robust against the effects of charging. This is not the case for modern satellites which carry complex and ever smaller integrated circuits. The first satellites also started orbiting the Earth at low altitude and inclination orbits which have lower environment radiation. As satellites started populating geosynchronous or polar orbits, the space environment became more hostile [163]. To try to diminish the severity and occurrence of spacecraft charging, an important effort is being made by the different space agencies, (ESA, NASA, JAXA…). To this effect, guidelines had been published in the standards followed by the distinct agencies, ECSS (ESA), NTSS (NASA), JERG (JAXA). This activity can be also seen in the biennial international conference "Spacecraft charging and technology conference" SCTC. However, even with all these efforts in improving charging mitigation capabilities and decreasing the related occurrence of failures (temporal or final), as the number of satellites is constantly increasing, spacecraft charging continues to be an issue [164-171]. An important one, once the tremendous economical investment of the companies is considered [172, 173]. In December 2019 there was at least 2218 active satellites in orbit around Earth [174]. The last openly reported incident due to spacecraft charging dates to 2012 but due to its commercial sensitiveness data is usually confidential [173].

Additionally, new materials are constantly being developed and employed in new missions such as Mars Atmosphere and Volatiles Evolution (MAVEN) [175, 176], Solar Orbiter [177, 178], Cassini [179] or Parker Solar Probe [180, 181]. The secondary electron emission properties of these materials need to be characterized to model and control spacecraft charging and correctly interpret the data of these missions [182].

2.6.2 Multipactor

Spacecraft charging is not the only phenomena that is caused by SEE in space. Radiofrequency (RF) hardware can be specifically affected by Multipactor. The Multipactor effect is a resonant secondary electron avalanche in a cavity whose walls have high SEY.

In a Multipactor discharge, a free electron in the RF cavity is accelerated towards the walls of the device by the RF signal. In the case, for example, of a parallel waveguide plate, this electron reaches the surface with some energy acquired from the signal and interact with the plate exciting new secondary electrons. These secondary electrons are then accelerated towards the other wall and consequently more secondary electrons are emitted. The number of electrons increase exponentially as they continue hitting the walls until an avalanche discharge is produced with enough density and energy to be able to distort the signal, increase the reflection coefficient, produce local surface heating or even destroy the device, **Figure 1.20**. The Multipactor discharge can be single-surface (dielectrics) or two-surface (metals) and depends on the walls and RF properties and the specific design of the device. Multipactor was first observed by Gutton in the laboratory [183] and has been studied with increasing attention to dielectric materials and numerical simulation in the last decades [76, 184-195]. The increasing demand of higher power in RF components and smaller devices has placed Multipactor as one of the main problems to be solved [189]. A higher power output facilitates the onset of the Multipactor effect as emitted electrons will attain higher energies and will liberate more electrons in the successive collisions with the walls.

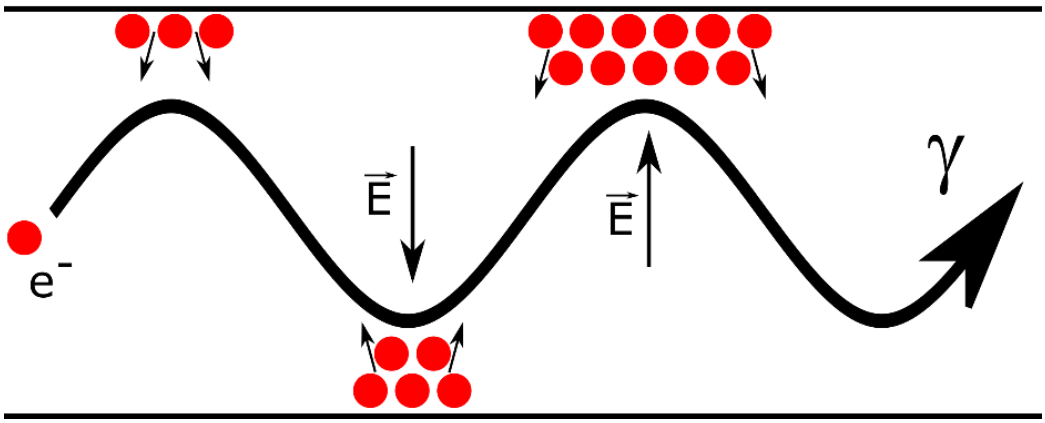

Figure 1.20. Schematic description of the Multipactor effect. An initial free electron oscillates with the RF signal traveling through the RF device. As it oscillates, the free electron hits the walls of the device at an energy given by the oscillation. If the free electron has enough energy on its impact, it will liberate more electrons from the wall, increasing the population of free electrons. As the electrons continue oscillating by the sustained RF signal, the population will increase up to a moment when the energy deposited by the electron flux is able to distort the signal or destroy the device.

As the Multipactor discharge is a secondary electron resonance phenomenon, it can occur only for certain combinations of operating conditions of the RF devices operating at low pressures. Multipactor is frequently represented by the 2D susceptibility charts or Multipactor diagrams, see **Figure 1.21**. In the case of the two parallel plates models, the Y axis of the chart is the amplitude of the RF wave and the X axis the product of the frequency and the gap distance between the walls of the device (the distance of the parallel plates). In this doctoral thesis, the MEST software was used to obtain the susceptibility charts of different materials. This software was previously developed as a task in an ESA project where ICMM-CSIC participated [184]. The main inputs of the software are the SEY parameters and the geometrical details of the two-parallel plates. The amplitude of the RF wave is parameterized as the peak to peak voltage. The susceptibility curves delimit the region where Multipactor is likely to occur or Multipactor region. Thus, the overall region where conditions of the system produce the electron discharge are clearly depicted. Multipactor discharge can happen in various modes, each characterized by an electron transit time equal to a certain odd number of half cycles of the propagating RF wave. It can be seen that for a fixed frequency, the Multipactor can appear at smaller gaps and higher voltages. This is directly confronted with the development of more powerful and smaller gaps (related to smaller devices) RF components.

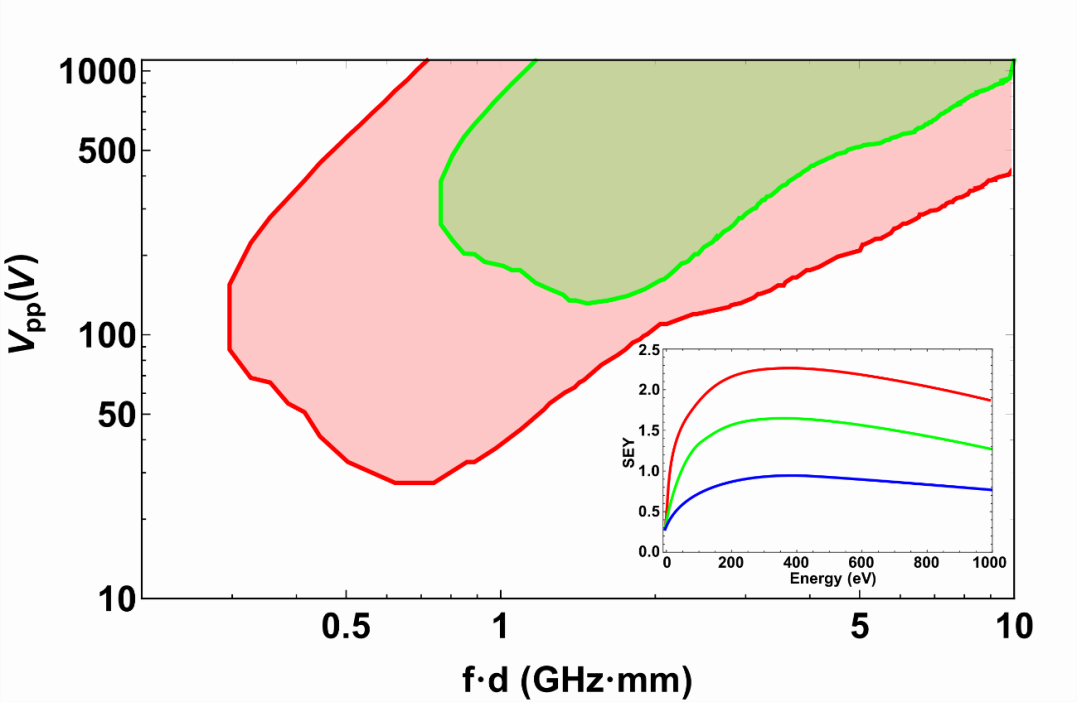

Figure 1.21. Multipactor susceptibility chart. Three different materials have been simulated in MEST to obtain their Multipactor regions. As can be seen the lower SEY (see inset) the smaller Multipactor region. It even completely vanishes for materials which SEY < 1.

The reduction of the SEY plays a very important role in the development of smaller and more powerful components. This can be easily seen comparing the three SEY curves in the Multipactor diagram, **Figure 1.21**. If the walls of the devices are coated with a material with a lower SEY, a device is able to sustain higher power outputs and the same coating can be used in smaller RF devices. The Multipactor discharge can be even avoided in RF filters if the SEY of the wall coating is < 1 [125, 196]. Multiple efforts are employed in mitigating Multipactor as can be seen for example in the triennial International Workshop MULCOPIM. Multipactor can also arise in any other vacuum system, such as particle accelerators and synchrotrons [197].

2.6.3 Electron cloud effects

Other phenomena produced by SEE such us electron-cloud effects, ECEs, affect specifically to large particle accelerators [198-204]. The electron cloud effect reduces the quality of the particle beam as the electric field produced by the free electrons inside the accelerator distort the main particle beam. The electron population inside the accelerator is produced in a similar

way as Multipactor but instead of gaining energy by the RF signal they gain it by the interaction with the central particle beam. The main outcome is that the vacuum quality and the beam intensity are reduced and instabilities of the main particle beam increase. The efforts to understand and mitigate the ECE can be seen, for example, in the international workshop ECLOUD.

2.6.4 Hall Thrusters

SEE is also a key factor in Hall Thrusters, one of the preferred electric propulsion systems for spacecraft in space. Currently, they are also being actively developed for their use in micropropulsion systems for Cubesats and small satellites [205-209].

In Hall Thrusters, a quasineutral plasma of ions and electrons is confined by electric and magnetic fields in a channel typically defined by two concentric ceramic cylinders. The anode is located at the bottom of this channel and an electron emissive cathode outside of it. A gas (typically Xenon) is injected through the anode and is ionized by the electrons forming the plasma. The ions are then accelerated away from the plasma by the electric field and neutralized at the plume end by the electrons flowing from the cathode to the anode, **Figure 1.22**.

In particular, electrons in the plasma are prevented from hitting the cylindrical walls that contains them by the effect of the plasma sheath. The plasma sheath appears due to the plasma having two distinctive species i.e. the ions and the electrons. As the diffusion of each species depends on their mass and temperature, in this plasma, ions diffuse slower than electrons due to their bigger mass and smaller energy. This produces a positive core in the middle of the concentric channel where electrons are attracted to as they diffuse close to the walls. Therefore, electrons are stopped or their energy is greatly decreased before hitting the walls of the channel which charge negatively due to the low energy electron bombardment. The potential gradient created by this mechanism between the plasma and the cylindrical walls is called the plasma sheath. The plasma sheath keeps the plasma electrons confined in the channel, reducing the electrons losses to the walls which is the main power loss mechanism in Hall Thrusters. The plasma-wall interaction dictates the performance and lifetime of the engine. A low SEY of the cylindrical walls is a critical factor to the performance of the Hall Thruster, as the less number of electrons emitted from the walls the more negatively the walls will charge, sustaining a bigger plasma sheath (i.e. a reduced number of plasma electrons reaching the walls and

therefore improved performance). Furthermore, a high number of secondary electrons injected in the plasma from the walls will be detrimental to the thruster performance because the plasma temperature will diminish due to the low energy of the secondary electrons [210-212]. However, the effect of SEE in the dynamics of Hall Thrusters are not yet completely understood and an extensive bibliography can be found on the subject [213-223].

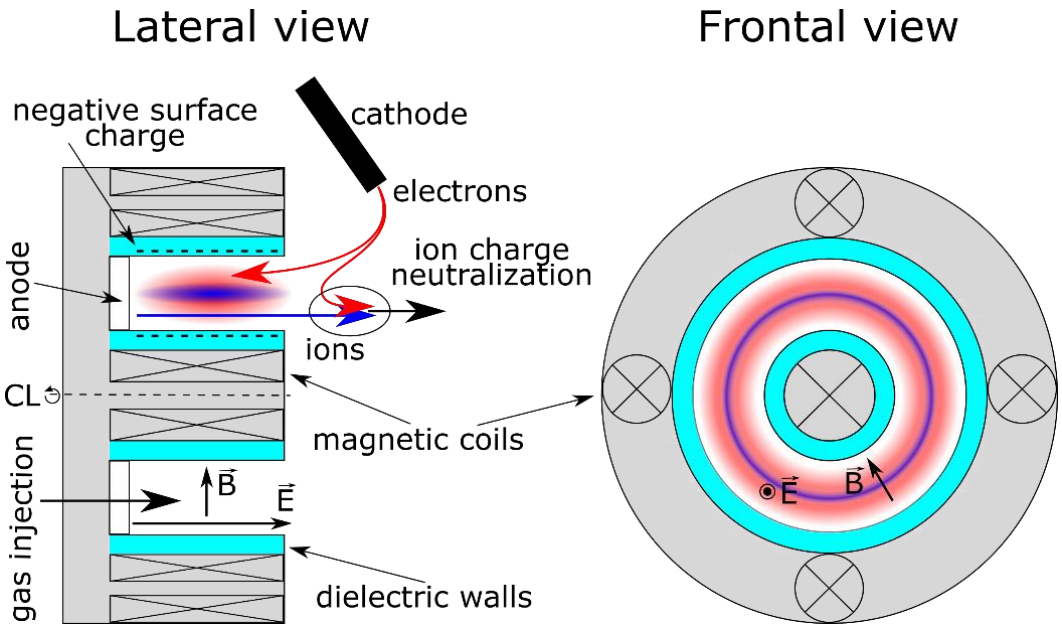

Figure 1.22. Diagram of the functioning of a Hall Thruster. Lateral (left) and frontal (right) view. The electrons are drawn in red and ions in blue. Ions and electrons are confined in the channel by the orthogonal magnetic ($\bar{B}$) and electric ($\bar{E}$) fields. Magnetic coils, anode and external cathode are used to produce the magnetic and electric fields respectively. Due to their smaller diffusion, the ion population is confined in a narrower volume in the center of the channel compared to the electron population. The cylindrical walls charge negatively due to plasma electron bombardment, increasing the electron confinement in the channel. Good electron confinement is important to decrease the power lost to the walls by the electron bombardment. Ions, once accelerated, are neutralized by the flow of electrons coming from the cathode.

2.6.5 Nuclear fusion

Similarly to Hall Thrusters, fusion tokamaks deal with plasma and therefore SEE raises to be an important factor in defining the plasma sheath and global performance [224-230]. Nuclear fusion has had sustained attention since the 1950s but it has not been until the last decades

when the fulfillment of its promises seems closer with the ITER (Latin for *'the way'*) and the following DEMO projects. Materials for the walls facing the plasma for the DEMO tokamak are still being discussed and the SEE of them studied [231]. Surely, further studies and discussions on these materials and their properties will take place the next years, as DEMO will not be constructed until at least 2040 [232].

Hall Thrusters and fusion are not the only plasma applications where SEE raise to be important. It is also essential in the understanding of dusty plasmas [233-235], plasma display panels [236-239] and emissive probes [240] to name a few other applications.

2.6.6 High Secondary Emission Yield applications

In all the applications introduced previously, high SEY materials are detrimental for the correct performance of spacecraft, devices or facilities. However, high SEY is also required for certain applications. For example, high SEY is desired in photomultiplier tubes (PMTs), cross field amplifiers (CFAs) and magnetrons [31, 41, 241-244]. In PMTs, multiple dynodes (electrodes with high SEY) are successively placed to amplify a weak input signal [20], **Figure 1.23**. PMTs can be used whenever feeble light signals need to be registered, which encompasses a wide range of fields. Hamamatsu, one of the main companies commercializing PMTs, list between the current possible applications healthcare, oil drilling, radiation monitoring, high energy experiments, microscopy and spectroscopy [245]. In CFAs and magnetrons, a cathode with high SEY is needed to maintain the electron population required for their operation. Magnetons are used in radar systems, microwave ovens, food processing, product sterilization and wood and rubber curing. CFAs are mainly used in radar systems [244].

Some materials such as, Al_2O_3, KI, KBr, KCl, MgO or diamond exhibit high SEY [241, 242] and values as high as 80 and 130 for diamond have been reported [31, 41]. These materials are insulators with a wide bandgap and/or negative electron affinity, which confers them the high SEY properties, see **Section 2.2.4**.

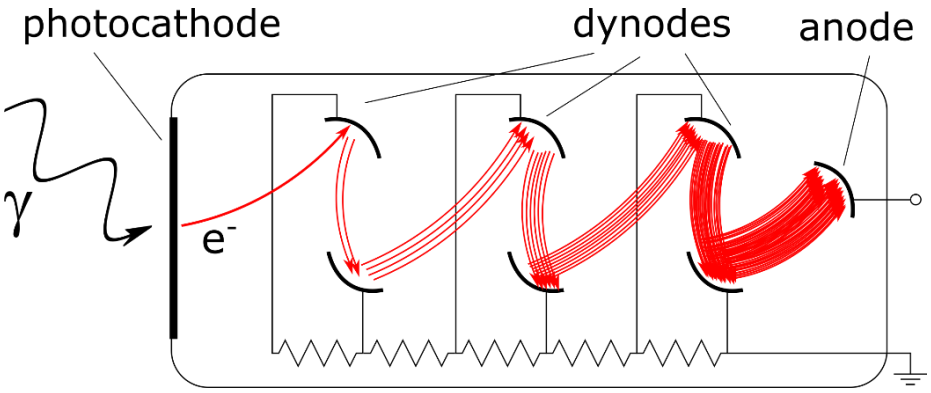

Figure 1.23. Description of the operation of a photomultiplier tube. The incident photon interacts with the photocathode to generate a photoelectron inside the tube. This photoelectron is accelerated towards the first dynode where it impacts producing a high number of secondary electrons due to the SEE. These secondary electrons are then accelerated towards the second dynode where they liberate even more secondary electrons. The process is subsequently repeated a number of times until the strongly amplified signal is collected in the anode where it can be measured.

2.7 Experimental techniques

The main characterization techniques used in this doctoral thesis in the laboratory at ICMM-CSIC are described in this section. The SEY measurements have been performed by the pulsed and continuous methods. The EDC has been acquired by the hemispherical electron analyzer and by the transient method proposed in *Publication 2* of this thesis. These techniques focus on the characterization of the SEE of the samples under study and therefore have been the more relevant on the thesis.

Other characterization techniques available in the ultrahigh vacuum (UHV) system of the laboratory are Auger electron spectroscopy (AES) and X-Ray Photoelectron spectroscopy (XPS), among others. These spectroscopic techniques mainly focus on the characterization of the surface composition and the electronic structure of the samples under study by analyzing the energy of the emitted electrons when the samples are irradiated by x-ray (XPS) or electrons (AES).

Scanning electron microscopy (SEM) is also a SEE technique that gives information on the topography of the samples and coupled to an energy dispersive X-ray (EDX) analyzer, the

composition of the sample can be obtained. SEM-EDX results were obtained mainly at ICMM-CSIC and at the SiDi of UAM.

2.7.1 SEY facility for space applications of CSIC

In the SEY facility for space applications at the *Instituto de Ciencia de Materiales de Madrid-CSIC* four ultra-high vacuum chambers are connected where SEY characterization, EDC acquisition, VUV photoemission characterization, AES and XPS spectroscopy can be performed, see **Figure 1.24**. The pressure in this set of chambers is always < 10^{-9} hPa. In the sample introduction chamber the vacuum reaches ~10^{-8} hPa. The three chambers can be completely isolated from each other by UHV gate valves and are provided with their own pumping system. The pumping system of each chamber comprises one scroll pump and one turbo pump. In addition, in the third chamber there is also an ionic pump. The characterization chambers count also with their own micrometric manipulators to place the samples on the desired position. Both of them are four axis manipulators and one of them is a helium cryostat, that can provide temperatures ranging from 2 to 700 K. A magnetic linear transference rod is used to transfer the samples from the sample introduction chamber to the desired analysis chamber.

In the vacuum system, Kimball physics electron guns can be found which can deliver electrons with energies from 0 to 5000 eV. An X-ray gun that delivers photons with monochromatic energies of 1486.6 eV (aluminum source) or 1253.6 eV (Magnesium source) is also present. A hemispherical electron energy analyzer (HEEA) is used to record the energy spectrum of electrons emitted by the samples under X-ray irradiation (XPS, XAES) or electron irradiation (EDC, AES). An ion gun is also available which can be used to clean the surface. The residual gas can be measured with a quadrupole.

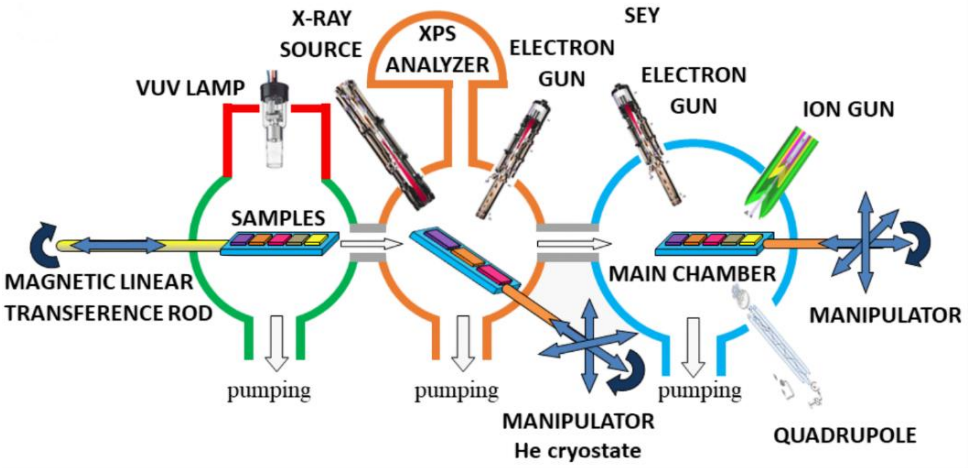

Figure 1.24. Diagram of the experimental system showing the characterization capabilities at the *Instituto de Ciencia de Materiales de Madrid – CSIC*.

2.7.2 SEY measurement method

Measuring the SEY requires a calibrating setup and the knowledge of two main variables, the incident charge and the emitted charge. There are several methods to measure the SEY.

The called *sample current method* measures the current from sample to ground. As can be seen in **Figure 1.25**, the sample current is the difference between the incident current and the emitted current, therefore from **Equation** 1.2:

$$SEY = \frac{I_{secondary}}{I_{incident}} = \frac{I_{emit}}{I_{eGun}} = \frac{I_{egun} + I_{sample}}{I_{eGun}} = 1 + \frac{I_{sample}}{I_{eGun}} \qquad (1.45)$$

Where $I_{secondary} = I_{emit}$ is the emitted current, $I_{incident} = I_{eGun}$ the incident current and I_{sample} the current flowing through the sample from ground. To measure the sample current, a negative bias is sometimes used to avoid that some SE may be trapped by a local positive charge that might develop in the surface of the sample. In this thesis the sample current method has been used to measure the SEY.

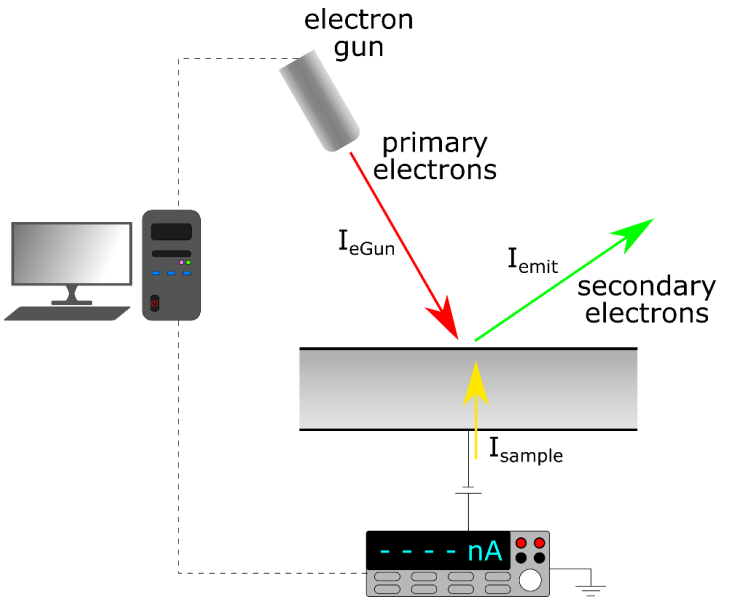

Figure 1.25. SEY measurement method. A computer software is used to control the energy of the primary electrons and acquire the current sample (I_{sample}). By charge conservation, I_{sample} is the difference between the electron gun current (I_{eGun}) and the emitted current (I_{emit}).

There are different ways to measure the gun current. One of the most extended one is the Faraday cup, FC. The FC is a metal cup designed to trap (ideally) all charged particles that go into it. As any electron that enters the FC cannot escape, the total current of the electron beam can be characterized measuring the current in the FC.

Other method to obtain I_{eGun} is to use a flat graphite sample. As explained in **Section 2.3.5**, most of the SEE radiation emitted by any sample has energies below 50 eV. Therefore, biasing a sample to +50 V ensures that all the secondary radiation but the backscattered radiation is trapped. In the case of the graphite, it is known that the backscattered radiation is ~12% of the total emitted radiation for a wide range of energies, **Figure 1.8**. Thus, measuring the sample current to ground of a positively biased graphite sample, the current of the incident electrons can be characterized. This method to measure the gun current has been used in this doctoral thesis.

2.7.2.1 Continuous method for SEY measurement

The continuous method is a method to acquire SEY curves (SEY as a function of the energy of the incident electrons) with a continuous beam of increasing energy. The sample current is acquired as the energy of the electron beam is linearly increased. The acquisition is done by a

computer program that continuously sets the energy of the electron beam and acquires the current measurement from an electrometer.

The typical current used to measure the SEY with this method is ~ 2 nA. This means that the current density used was 25 pA/mm^2 with a total dose in the complete measurement of a SEY curve of ~10 nC/ mm^2. However, for the purpose of this thesis it was sometimes required to increase the incident current to ~ 20 nA, such as in the high dose measurements in *Publication 1*.

The continuous method used in the laboratory is a reliable method that can measure the complete SEY curve up to 5000 eV with an error ≤ 0.1.

2.7.2.2 Pulsed method for SEY measurement

The pulsed method used in the ICMM-CSIC facility focusses on the use of a very low electron dose for SEY characterization to avoid charging issues. In this method, a single pulse is generated for each primary energy to perform the SEY measurements. Therefore, the **Equation** 1.45 is now to be expressed as:

$$SEY = \frac{Q_{emit}}{Q_{eGun}} = \frac{Q_{egun} + Q_{ground}}{Q_{eGun}} = 1 + \frac{Q_{ground}}{Q_{eGun}} \quad (1.46)$$

Where Q_{emit} is the emitted charge, Q_{eGun} the incident charge in one pulse and Q_{ground} the charge flowing from ground to sample.

For this measurement, a pulsed electron beam, a fast amplifier and an oscilloscope to capture and register the pulses are required, see **Figure 1.26**. In the results presented in this thesis, pulses of 180 ns were used. In addition to single pulses, train of pulses with periods of 10 µs were used in *Publication 2* and *Publication 3*. The fast amplifier is set at an amplification of 10^5 V/C. The pulse length used in this thesis has been mainly 180 ns. The total incident charge per pulse under these conditions is approximately 0.5 pC, which means approximately 6 fC/mm^2. The oscilloscope has four channels, records one or several pulses and saves them on the format desired for their subsequent analysis.

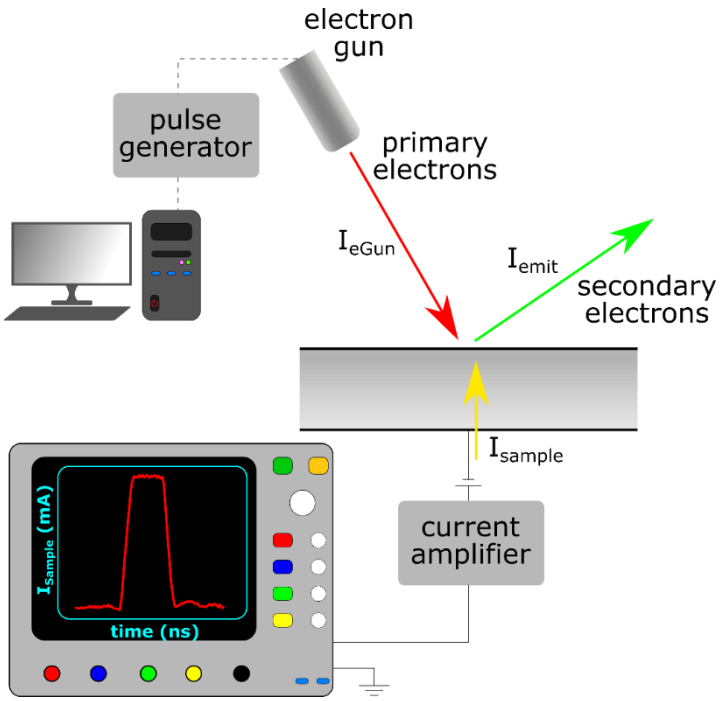

Figure 1.26. SEY pulse method. The computer is used to set the energy of the pulse electron beam. A current amplifier is then needed to amplify the sample current (I_{Sample}) signal. The amplified signal is finally acquired by an oscilloscope where pulses can be analyzed *in-situ* or exported to be treated elsewhere.

The reduced charge makes this method adequate to measure non-conductive samples. It avoids charging the sample and charging has been shown in **Section 2.5.1** to produce a very important effect on the SEE properties. However, depending on the material under study, even this low dose method can produce charging after a few measurements and the dissipation of the deposited charge becomes essential.

2.7.2.3 Spot Size

A spot size of 0.5 mm and 5 mm of the electron beam were used. The charge is delivered homogeneously on all the irradiated area. The charge densities and doses given in the previous sections are delivered when the spot size of 5 mm is used.

As part of the work performed in the thesis, the author of this thesis updated the capabilities of the gun software controller by adding the functionality of using the small spot in the measurements.

2.7.3 EDC acquisition with the HEEA

The hemispherical electron energy analyzer, HEEA, can be used to acquire the electron energy spectra, or energy distribution curve, of samples under continuous irradiation with a monoenergetic primary electron beam. The current of the incident beam is ~ 10 nA and the samples must be grounded to avoid charging.

The HEEA can acquire the complete EDC curve from 0 eV up to the energy of the incident beam. However, as the current needs to be high its use is not suitable to measure electrical insulating samples. It has been used coupled with charge dissipation techniques but not always with satisfactory results [145, 246]. Problems might be explained by deep charging and radiation damage due to high doses of incident electrons as the authors themselves suggest.

2.7.4 EDC measurement by transient analysis

This method is proposed in *Publication 2* and used in *Publication 3* to measure EDC of electrical insulating materials. It expands the possibilities of measuring EDC in the positive charging regime (ii-1), i.e. between the first cross-over energy, E_1, and E'. In this region, a unique positive charge layer is produced by the incident radiation in the solid.

This method takes advantage on the charging transient that any electrical insulator sustains while irradiated. If the primary energy is $E_1 < E_p < E'$, the surface of the dielectric will charge positively, trapping the low energetic emitted secondary electrons. Coupling the increasing deposited charge (therefore the increasing surface potential) with the decreasing number of emitted secondary electrons, the energy distribution curve can be obtained. See *Publication 2*, *Publication 3* and the previous discussion on them for a more thorough explanation.

2.7.5 X-ray photoelectron spectroscopy, XPS

X-ray photoelectron spectroscopy (XPS) is a technique that permits to obtain information about the composition, chemical state, interfaces and electronic structure of a sample [48, 247]. It is based on the photoelectric effect discovered by Einstein and worth of his Nobel Prize [248]. Interestingly, Kai Siegbahn also obtained the Nobel Prize for developing XPS [249]. When a material is irradiated by photons of enough energy, for example, soft X-rays, by the conservation of energy, it is fulfilled:

$$E_K = h \cdot \upsilon - E_B - \phi_{SPEC} \quad (1.47)$$

Where E_K is the kinetic energy of the photoelectron, $h \cdot \upsilon$ the energy of the photon, E_B the binding energy of the atomic orbital from which the photoelectron originates and ϕ_{SPEC} is the work function of the spectrometer. **Figure 1.27** shows a description of the photoemission process.

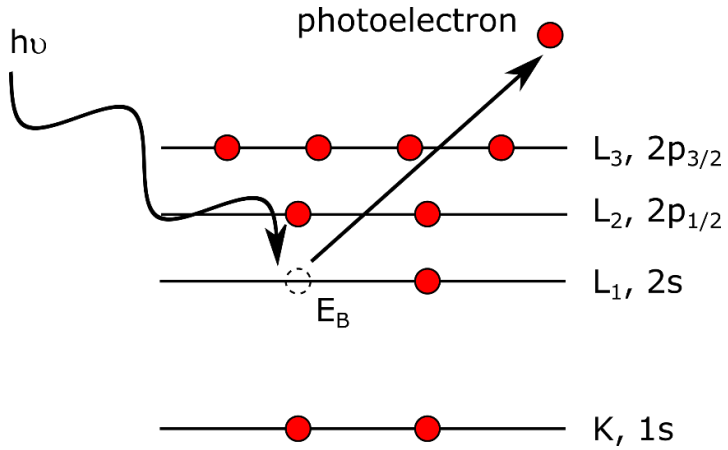

Figure 1.27. Description of the emission process of XPS. The energy of an X-ray photon is absorbed by an electron of a core level in the atom and it is emitted as a photoelectron with an energy equal to the difference of the photon energy ($h\upsilon$) and the binding energy of the electron in the atom (E_B). In this case a photoelectron from the level 2s is emitted.

Every sample has a specific atomic density with elements that have orbitals with characteristic cross-sections and different orbital symmetry factors, also different inelastic electron mean-free paths, which leads to specific peaks in the XPS spectra of the sample. For example, small shifts in the binding energies of the peaks of the core levels can be measured during the quantification of the spectra and the chemical state of the elements can be obtained.

Usually monoenergetic soft X-rays are used to irradiate the sample, typically the Kα lines of Mg (1253.6 eV) and Al (1486.6 eV). These photons can travel in the solid some 1-10 μm but, as explained in **Section 2.2.5**, the photoelectrons are only emitted from the most superficial layer of ~1 nm. Furthermore, only those originated very superficially will be emitted without any energy loss and will produce the peaks on the spectra. The rest of them will contribute to the background.

2.7.6 Auger electron spectroscopy

During electron irradiation of the sample other phenomena arise, such as X-ray emission or Auger emission from the sample, as the atom relaxes from its excited state [29, 247]. Auger electron spectroscopy, AES, analyze the auger electrons emitted from the solid. As these electrons are emitted due to the relaxation of an excited atom, the mechanism is independent of the initial radiation that had previously excited the atom. Auger electrons are emitted when the solid is irradiated with either photon or electron radiation.

When an electron of the excited atom relaxes to an available lower energetic state, the energy liberated can be released emitting a second electron (i.e. Auger electron). The energy of this second electron will be directly related to the energetic structure of the material and therefore it will be characteristic of it. The conservation of energy dictates:

$$E_K = E_A - E_B - E_C \tag{1.48}$$

Where E_K is the kinetic energy of the Auger electron, E_A the binding energy of the atomic orbital from which the electron is liberated by the primary source of radiation (i.e. the vacancy to which the relaxed electron falls), E_B the binding energy of the atomic orbital of the falling electron and E_C the binding energy of the atomic orbital of the Auger electron, see **Figure 1.28**. $E_A - E_B$ is the energy available for the emission of the Auger electron and E_C the required energy emission.

As there are more electrons involved in the process Auger spectra are more complex than XPS spectra. A difference of Auger spectra with XPS spectra is that the kinetic energy of the emitted electron does not depend on the energy of the source of excitation and therefore the measured spectrum does not shift with the energy of the source.

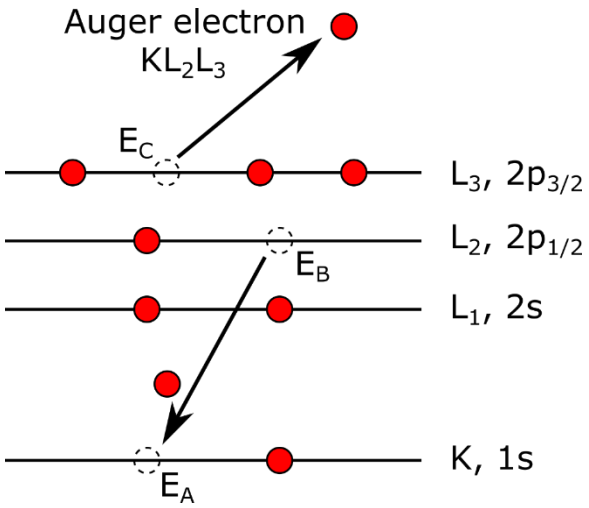

Figure 1.28. Description of the Auger emission process. The transition KL_2L_3 is displayed. An excited atom with a vacancy in the orbital K level is shown. An electron from a less energetic orbital (from the L_2 level) relaxes and occupy the vacancy. The energy is liberated by the emission of an Auger electron (from the level L_3) with energy obeying the energy conservation law. The Auger spectra does not depend on the radiation source as the energy of the incident irradiation is not involved in the possible transitions in Auger spectroscopy.

2.7.7 Energy dispersive X-Ray spectroscopy

Energy dispersive X-Ray spectroscopy, (EDX or EDS), is usually coupled to scanning electron microscopy [29]. It acquires the X-Ray radiation emitted from the solid during electron bombardment. As mentioned before, one of the relaxation mechanism of an excited ion is the emission of a photon, in this case, the emitted photons are X-Rays. The measurement of their energy gives a characteristic signal in the spectra for each element. It is a powerful technique to obtain the composition of the analyzed samples in a SEM. The energy of the photons is the energy difference between the binding energies of the emitted electron and the electron that relaxes to the vacancy:

$$h\nu = E_A - E_B \tag{1.49}$$

Where $h\upsilon$ is the energy of the emitted photon, E_A the binding energy of the extracted electron and E_B the binding energy of the core level of the relaxed electron, see **Figure 1.29**. Similar to AES, EDX spectra do not depend on the energy of the incident electrons.

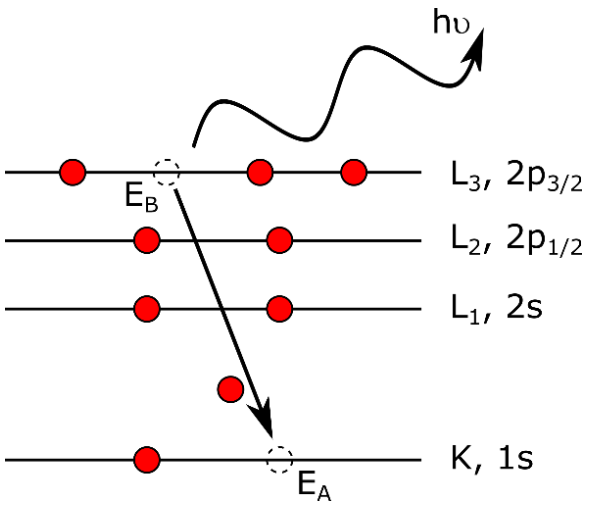

Figure 1.29. Description of energy dispersive X-Ray spectroscopy. The transition KL_3 is shown. An excited atom with a vacancy in the K level can be seen in the figure. An electron from a less energetic orbital (level L_3 in the figure) relaxes and occupy the vacancy.

2.7.8 Scanning electron microscopy

Scanning electron microscopy (SEM) is a technique used to obtain images of the surface of a sample by scanning its surface with a focused electron beam. The secondary electrons emitted are recorded in a detector to produce the images.

The extensive use of SEM is due to the direct interpretation of the images it produces and the relevant information they convey. This is mainly due to the *topographic contrast* that allows the visualization of the topography of the sample. Topographic contrast arises from the properties of the SEE already discussed on **Section 2.3**. The dependence of the SEY on the angle of incidence of the beam is one of the main contributions to this contrast.

In addition to SEM, in this doctoral thesis Field Emission SEM (FE-SEM) was also used. FE-SEM benefits from an enhanced method of producing primary electrons which enables it to obtain better resolution and higher signal than the standard SEM.

The interaction of the electron beam with the atoms of the sample, as explained in the previous discussion, gives raise to two different signals: backscattered electrons and true secondary electrons. These two signals convey different information about the scanned surface [29].

2.7.8.1 Backscattered electron signal

Due to the strong dependence of the backscattered electron yield on the atomic number, Z, this signal is sensitive to the composition of the sample, **Figure 1.6**. Elements with higher atomic number will be seen brighter than elements with lower atomic number. This is called, *compositional contrast*. The backscattered electron signal confers information on specimen composition usually mixed with topography information. *Topographic contrast* of backscattered electrons come from the fact that the angle at which they are emitted depends on the inclination of the surface, which modifies the collection efficiency of backscattered electrons [29].

2.7.8.2 Secondary electron signal

The true secondary electron yield depends strongly on the surface inclination, **Section 2.3.4**. This effect creates the *topographic contrast* of the secondary electron signal. As the only contrast, this signal is more sensitive to surface topography than the backscattered signal [29].

2.7.8.3 Charging phenomena in SEM

Charging in SEM images develops when the specimen under study is not able to dissipate all the deposited charge by the electron beam. In SEM, charging is usually seen as bright spots or areas where the *topographic contrast* is completely overwhelmed, see **Figure 1.30**. Is easy to see that charging in SEM especially affects the secondary electron signal due to the low energy of these electrons. Several specific methods exist to mitigate or eliminate charging in SEM, such as metallization: coating the samples by a thin (~ 5 nm) layer of a conduction material (for example gold, chromium or carbon) or work with low vacuum (ESEM) [29, 159].

In this doctoral thesis, charging in SEM experiments was employed to demonstrate that charging was taking place in the metal/dielectric samples in *Publication 1*.

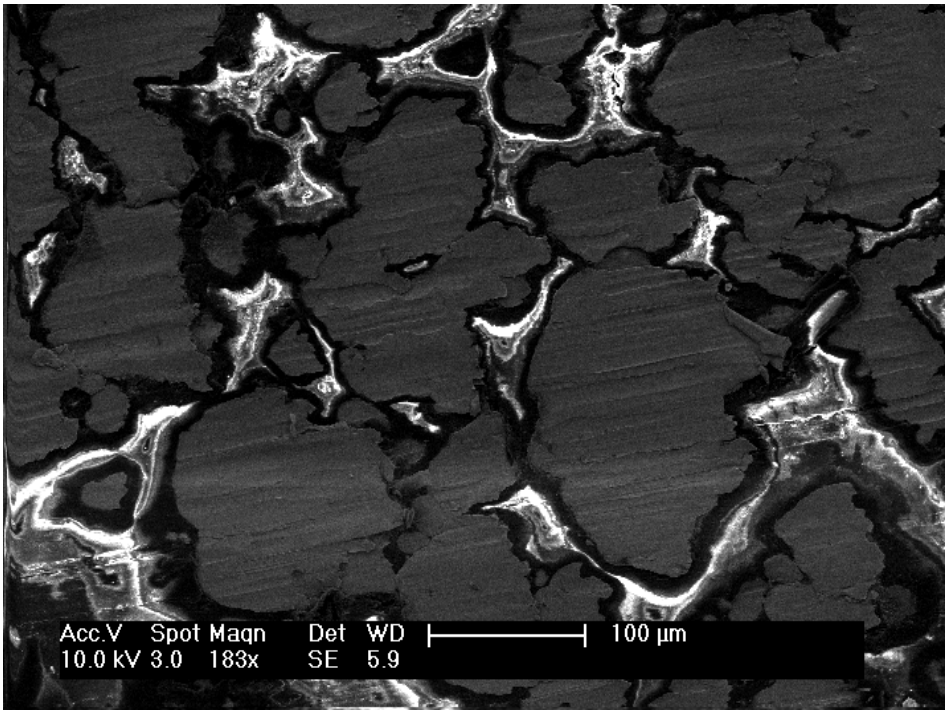

Figure 1.30. SEM image of a metal/dielectric sample obtained in a FE-SEM. Flat conductor areas can be seen of an almost homogenous gray, where small ridges can be appreciated. Insulator areas can be seen as bright shapes surrounded by black areas. These bright shapes, rapidly oscillate under continuous visualization in the SEM. The topographical information of the dielectric domains has been distorted by the effect of charging.

2.8 Software

Different software was used to support the investigation presented in this thesis. The most relevant software used in this doctoral thesis will be introduced below.

2.8.1 Wolfram Mathematica

Wolfram Mathematica [250] is a modern technical computing system based on the Wolfram Language used in many scientific fields. It was used in *Publication 1* to compute electric fields and then simulate trajectories of electrons in them. It was also used to treat and analyze the charging curves to obtain the EDC of different materials in *Publication 2* and *Publication 3*.

2.8.2 Comsol Multiphysics

Comsol Multiphysics [251] is a general-purpose simulation software for modeling designs, devices and processes in all fields of engineering, manufacturing and scientific research. In *Publication 2*, simulations in Comsol were compared to measurements obtained in the laboratory. It was also used in *Publication 3* for computing the voltage produced by a dielectric surface when it has been charged with constant surface charge density.

2.8.3 LabView

LabView [252] is a development environment for a graphical programming language called "G" designed by National Instruments. It eases the complex task of developing graphical user interfaces (GUI) and communications with a wide scope of laboratory equipment. Among its capabilities are instrument control, automation and data acquisition. The author of this thesis spent a considerable amount of his time developing a GUI for the control and data acquisition of voltage sources and ammeters to electroplate aluminum with silver. However, the results obtained were not published and therefore not shown in this thesis.

2.8.4 Borland C++

Borland C++ [253] is a C++ integrated development environment (IDE). It was used to improve the functionality of the electron gun. Specifically, a new small spot mode was implemented in the acquisition software that controls the electron gun and the electrometers. This mode focuses the electrons of the electron beam in a 0.1 mm radius spot.

2.8.5 CASINO

CASINO [254] is a Monte Carlo simulation of electron trajectories in solids. It can simulate SE and X-rays emission produced by the interaction of the incident electrons. It was used to simulate the penetration range of primary electrons on different materials.

2.8.6 MEST

MEST (Multipactor Electron Simulation Tool) [184] is a software tool that simulates the occurrence of Multipactor discharge between parallel plates. It was used to obtain the Multipactor charts. In this software, each electron between the two plates of the system is modelled separately. To perform the simulation, the critical inputs are the secondary emission yield (SEY) of the plates and the external parameters of the device and RF wave. The goal of this software is to generate V-f·d maps or susceptibility charts of the Multipactor discharge detected in the simulations. Materials are described in the software using the usual SEY parameters (σ_{max}, E_{max}, E_1 and E_2,) or a more detailed SEY model, where the total SEY is divided into the three contributions: true secondary, backscattered or elastically reflected electrons, along with parameters for the angle dependence.

2.8.7 Python

Python [255] is an interpreted, high-level and general-purpose programming language. In this doctoral thesis Python was used, for example, to develop a program that extracts and treats the data obtained in MEST for Multipactor simulation. This way the data treatment capability of MEST was improved.

2.9 References

[1] H. Seiler, "Secondary electron emission in the scanning electron microscope," *Journal of Applied Physics,* vol. 54, no. 11, pp. R1-R18, 1983, doi: 10.1063/1.332840.

[2] L. A. Harris, "Analysis of Materials by Electron-Excited Auger Electrons," *Journal of Applied Physics,* vol. 39, no. 3, pp. 1419-1427, 1968/02/15 1968, doi: 10.1063/1.1656374.

[3] H. C. Miller, "Surface flashover of insulators," *IEEE Transactions on Electrical Insulation,* vol. 24, no. 5, pp. 765-786, 1989, doi: 10.1109/14.42158.

[4] J. J. Lander, "Auger Peaks in the Energy Spectra of Secondary Electrons from Various Materials," *Physical Review,* vol. 91, no. 6, pp. 1382-1387, 09/15/ 1953, doi: 10.1103/PhysRev.91.1382.

[5] D. Haneman, "Surface Structures and Properties of Diamond-Structure Semiconductors," *Physical Review,* vol. 121, no. 4, pp. 1093-1100, 02/15/ 1961, doi: 10.1103/PhysRev.121.1093.

[6] J. R. M. Vaughan, "A NEW FORMULA FOR SECONDARY-EMISSION YIELD," (in English), *Ieee Transactions on Electron Devices,* Article vol. 36, no. 9, pp. 1963-1967, Sep 1989, doi: 10.1109/16.34278.

[7] M. P. Villard, "Sur les rayons cathodiques," *J. Phys. Theor. Appl.,* vol. 8, no. 1, pp. 5-16, 1899.

[8] L. Austin and H. Starke, "Ueber die Reflexion der Kathodenstrahlen und eine damit verbundene neue Erscheinung secundärer Emission," *Annalen der Physik,* vol. 314, no. 10, pp. 271-292, 1902, doi: 10.1002/andp.19023141003.

[9] A. A. C. Swinton and W. Thomson, "On the reflection of cathode rays," *Proceedings of the Royal Society of London,* vol. 64, no. 402-411, pp. 377-395, 1899, doi: doi:10.1098/rspl.1898.0117.

[10] P. Lenard, "Über sekundäre Kathodenstrahlung in gasförmigen und festen Körpern," *Annalen der Physik,* vol. 320, no. 13, pp. 485-508, 1904, doi: 10.1002/andp.19043201304.

[11] C. Füchtbauer, "Über die Geschwindigkeit der von Kanalstrahlen und von Kathodenstrahlen beim Auftreffen auf Metalle erzeugten negativen Strahlen," *Deutschen physikalischen Gesellschaft,* pp. 394-398, 1906.

[12] C. Füchtbauer, "Über Sekundärstrahlen," *Annalen der Physik,* vol. 328, no. 7, pp. 301-307, 1907, doi: 10.1002/andp.19073280709.

[13] J. Laub, "Über sekundäre Kathodenstrahlen," *Annalen der Physik,* vol. 328, no. 7, pp. 285-300, 1907, doi: 10.1002/andp.19073280708.

[14] P. Redhead, "History of vacuum devices," 1999, doi: 10.5170/CERN-1999-005.281.

[15] I. G. Barber, "Secondary Electron Emission from Copper Surfaces," *Physical Review,* vol. 17, no. 3, pp. 322-338, 03/01/ 1921, doi: 10.1103/PhysRev.17.322.

[16] J. B. Johnson, "Secondary Electron Emission from Targets of Barium-Strontium Oxide," *Physical Review,* vol. 73, no. 9, pp. 1058-1073, 05/01/ 1948, doi: 10.1103/PhysRev.73.1058.

[17] A. W. Hull, "The Dynatron A Vacuum Tube Possessing Negative Electric Resistance," *Proceedings of The Institute of Radio Engineers,* vol. 6, no. 1, pp. 5-35, 1918.

[18] J. Slepian, "Hot-cathode tube," US Patent Appl. US1450265A, 1919. [Online]. Available: https://patents.google.com/patent/US1450265A

[19] F. A. Furfari, "Joseph Slepian-scientist, engineer, inventor," *IEEE Industry Applications Magazine,* vol. 6, no. 6, pp. 14-19, Nov.-Dec. 2000, doi: 10.1109/2943.877835.

[20] T. Wright and A. G. Wright, *The Photomultiplier Handbook*. Oxford University Press, 2017.

[21] B. K. Lubsandorzhiev, "On the history of photomultiplier tube invention," *Nuclear Instruments and Methods in Physics Research Section A: Accelerators, Spectrometers, Detectors and Associated Equipment,* vol. 567, no. 1, pp. 236-238, 2006/11/01/ 2006, doi: https://doi.org/10.1016/j.nima.2006.05.221.

[22] D. McMullan, "Scanning electron microscopy 1928–1965," *Scanning,* vol. 17, no. 3, pp. 175-185, 1995, doi: 10.1002/sca.4950170309.
[23] M. von Ardenne, "Improvements in electron microscopes. British patent no. 511204, convention date (Germany) 18 Feb 1937," [Online]. Available: https://worldwide.espacenet.com/textdoc?DB=EPODOC&IDX=GB511204
[24] D. Hastings and H. Garrett, *Spacecraft-Environment Interactions*. Cambridge University Press, 2004.
[25] R. Grard, K. Knott, and Pedersen, "Spacecraft charging effects," *Space Science Reviews,* vol. 34, no. 3, pp. 289-304, 1983/03/01 1983, doi: 10.1007/BF00175284.
[26] P. Zhang, Z. Wang, J. H. Perepezko, and P. M. Voyles, "Elastic and inelastic mean free paths of 200keV electrons in metallic glasses," *Ultramicroscopy,* vol. 171, pp. 89-95, 2016/12/01/ 2016, doi: https://doi.org/10.1016/j.ultramic.2016.09.005.
[27] M. Rösler, *Particle induced electron emission I*. Springer-Verlag, 1991.
[28] W. S. M. Werner, "Electron transport in solids for quantitative surface analysis," (in English), *Surface and Interface Analysis,* Review vol. 31, no. 3, pp. 141-176, Mar 2001, doi: 10.1002/sia.973.
[29] J. I. Goldstein, D. E. Newbury, J. R. Michael, N. W. M. Ritchie, J. H. J. Scott, and D. C. Joy, *Scanning Electron Microscopy and X-Ray Microanalysis*. Springer New York, 2017.
[30] O. Y. Ridzel, V. Astašauskas, and W. S. M. Werner, "Low energy (1–100 eV) electron inelastic mean free path (IMFP) values determined from analysis of secondary electron yields (SEY) in the incident energy range of 0.1–10 keV," *Journal of Electron Spectroscopy and Related Phenomena,* 2019/02/12/ 2019, doi: https://doi.org/10.1016/j.elspec.2019.02.003.
[31] A. Shih, J. Yater, C. Hor, and R. Abrams, "Secondary electron emission studies," *Applied Surface Science,* vol. 111, pp. 251-258, 1997/02/03/ 1997, doi: https://doi.org/10.1016/S0169-4332(96)00729-5.
[32] S. Clerc, J. R. Dennison, R. Hoffmann, and J. Abbott, "On the Computation of Secondary Electron Emission Models," *IEEE Transactions on Plasma Science,* vol. 34, no. 5, pp. 2219-2225, 2006, doi: 10.1109/TPS.2006.883379.
[33] G. Wilson and J. R. Dennison, "Approximation of Range in Materials as a Function of Incident Electron Energy," (in English), *Ieee Transactions on Plasma Science,* Article vol. 40, no. 2, pp. 291-297, Feb 2012, doi: 10.1109/tps.2011.2176515.
[34] C. T. Chantler and J. D. Bourke, "Electron Inelastic Mean Free Path Theory and Density Functional Theory Resolving Discrepancies for Low-Energy Electrons in Copper," *The Journal of Physical Chemistry A,* vol. 118, no. 5, pp. 909-914, 2014/02/06 2014, doi: 10.1021/jp408438r.
[35] C. T. Chantler and J. D. Bourke, "Low-energy electron properties: Electron inelastic mean free path, energy loss function and the dielectric function. Recent measurements, applications, and the plasmon-coupling theory," *Ultramicroscopy,* vol. 201, pp. 38-48, 2019/06/01/ 2019, doi: https://doi.org/10.1016/j.ultramic.2019.03.014.
[36] P. de Vera and R. Garcia-Molina, "Electron Inelastic Mean Free Paths in Condensed Matter Down to a Few Electronvolts," *The Journal of Physical Chemistry C,* vol. 123, no. 4, pp. 2075-2083, 2019/01/31 2019, doi: 10.1021/acs.jpcc.8b10832.
[37] W. S. M. Werner *et al.*, "Contribution of surface plasmon decay to secondary electron emission from an Al surface," *Applied Physics Letters,* vol. 99, no. 18, p. 184102, 2011, doi: 10.1063/1.3658455.
[38] W. S. M. Werner *et al.*, "Role of surface and bulk plasmon decay in secondary electron emission," (in English), *Physical Review B,* Article vol. 78, no. 23, p. 4, Dec 2008, Art no. 233403, doi: 10.1103/PhysRevB.78.233403.
[39] A. Bellissimo *et al.*, "Secondary electron generation mechanisms in carbon allotropes at low impact electron energies," *Journal of Electron Spectroscopy and Related Phenomena,* p. 146883, 2019/08/21/ 2019, doi: https://doi.org/10.1016/j.elspec.2019.07.004.

[40] M. S. Chung and T. E. Everhart, "Simple calculation of energy distribution of low-energy secondary electrons emitted from metals under electron bombardment," *Journal of Applied Physics,* vol. 45, no. 2, pp. 707-709, 1974, doi: 10.1063/1.1663306.

[41] J. E. Yater, A. Shih, and R. Abrams, "Electronic properties of diamond for high-power device applications," *Solid-State Electronics,* vol. 42, no. 12, pp. 2225-2232, 1998/12/01/ 1998, doi: https://doi.org/10.1016/S0038-1101(98)00219-6.

[42] J. E. Yater and A. Shih, "Secondary electron emission characteristics of single-crystal and polycrystalline diamond," *Journal of Applied Physics,* vol. 87, no. 11, pp. 8103-8112, 2000/06/01 2000, doi: 10.1063/1.373505.

[43] J. E. Yater, A. Shih, and R. Abrams, "Electron transport and emission properties of C(100)," *Physical Review B,* vol. 56, no. 8, pp. R4410-R4416, 08/15/ 1997, doi: 10.1103/PhysRevB.56.R4410.

[44] C. J. Powell, A. Jablonski, I. S. Tilinin, S. Tanuma, and D. R. Penn, "Surface sensitivity of Auger-electron spectroscopy and X-ray photoelectron spectroscopy," *Journal of Electron Spectroscopy and Related Phenomena,* vol. 98-99, pp. 1-15, 1999/01/01/ 1999, doi: https://doi.org/10.1016/S0368-2048(98)00271-0.

[45] A. Jablonski, "Effects of Auger electron elastic scattering in quantitative AES," *Surface Science,* vol. 188, no. 1, pp. 164-180, 1987/09/02/ 1987, doi: https://doi.org/10.1016/S0039-6028(87)80149-8.

[46] A. Jablonski and H. Ebel, "Comparison of electron attenuation lengths and escape depths with inelastic mean free paths," *Surface and Interface Analysis,* vol. 11, no. 12, pp. 627-632, 1988, doi: 10.1002/sia.740111208.

[47] A. Jablonski, "Quantitative AES: Via the inelastic mean free path or the attenuation length?," *Surface and Interface Analysis,* vol. 15, no. 9, pp. 559-566, 1990, doi: 10.1002/sia.740150910.

[48] C. J. Powell and A. Jablonski, "Progress in quantitative surface analysis by X-ray photoelectron spectroscopy: Current status and perspectives," *Journal of Electron Spectroscopy and Related Phenomena,* vol. 178-179, pp. 331-346, 2010/05/01/ 2010, doi: https://doi.org/10.1016/j.elspec.2009.05.004.

[49] E. M. Baroody, "A Theory of Secondary Electron Emission from Metals," *Physical Review,* vol. 78, no. 6, pp. 780-787, 06/15/ 1950, doi: 10.1103/PhysRev.78.780.

[50] H. Bruining, *Physics and applications of secondary electron emission*, 1st ed. (Electronics and Waves Series). Great Britain: Pergamon Press LTD., 1954.

[51] R. G. Lye and A. J. Dekker, "Theory of Secondary Emission," *Physical Review,* vol. 107, no. 4, pp. 977-981, 08/15/ 1957, doi: 10.1103/PhysRev.107.977.

[52] G. F. Dionne, "Effects of secondary electron scattering on secondary emission yield curves," *Journal of Applied Physics,* vol. 44, no. 12, pp. 5361-5364, 1973/12/01 1973, doi: 10.1063/1.1662156.

[53] G. F. Dionne, "Origin of secondary-electron-emission yield-curve parameters," *Journal of Applied Physics,* vol. 46, no. 8, pp. 3347-3351, 1975/08/01 1975, doi: 10.1063/1.322061.

[54] K. Kanaya and H. Kawakatsu, "Secondary electron emission due to primary and backscattered electrons," *Journal of Physics D: Applied Physics,* vol. 5, no. 9, pp. 1727-1742, 1972/09/01 1972, doi: 10.1088/0022-3727/5/9/330.

[55] S. Ono and K. Kanaya, "The energy dependence of secondary emission based on the range-energy retardation power formula," *Journal of Physics D: Applied Physics,* vol. 12, no. 4, pp. 619-632, 1979/04/14 1979, doi: 10.1088/0022-3727/12/4/019.

[56] R. Vaughan, "SECONDARY-EMISSION FORMULAS," (in English), *Ieee Transactions on Electron Devices,* Note vol. 40, no. 4, pp. 830-830, Apr 1993, doi: 10.1109/16.202798.

[57] M. A. Furman and M. T. F. Pivi, "Probabilistic model for the simulation of secondary electron emission," (in English), *Physical Review Special Topics-Accelerators and Beams,* Article vol. 5, no. 12, p. 18, Dec 2002, Art no. 124404, doi: 10.1103/PhysRevSTAB.5.124404.

[58] A. Shih and C. Hor, "SECONDARY-EMISSION PROPERTIES AS A FUNCTION OF THE ELECTRON INCIDENCE ANGLE," (in English), *Ieee Transactions on Electron Devices,* Article vol. 40, no. 4, pp. 824-829, Apr 1993, doi: 10.1109/16.202797.

[59] O. Hachenberg and W. Brauer, "Secondary Electron Emission from Solids," in *Advances in Electronics and Electron Physics*, vol. 11, L. Marton and C. Marton Eds.: Academic Press, 1959, pp. 413-499.

[60] J. J. Scholtz, D. Dijkkamp, and R. W. A. Schmitz, "Secondary electron emission properties," *Philips Journal of Research,* vol. 50, no. 3, pp. 375-389, 1996/01/01/ 1996, doi: https://doi.org/10.1016/S0165-5817(97)84681-5.

[61] A. J. Dekker, F. Seitz, and D. Turnbull, "Secondary Electron Emission," in *Advances in Research and Applications*, vol. 6: Academic Press, 1958, pp. 251-311.

[62] J. L. H. Jonker, "The angular distribution of the secondary electrons of nickel," *Philips Res. Repts.,* vol. 6, pp. 372-387, 1951.

[63] Y. He *et al.*, "Effect of atmospheric exposure on secondary electron yield of inert metal and its potential impact on the threshold of multipactor effect," *Applied Surface Science,* vol. 520, p. 146320, 2020/08/01/ 2020, doi: https://doi.org/10.1016/j.apsusc.2020.146320.

[64] N. Hilleret, C. Scheuerlein, and M. Taborelli, "The secondary-electron yield of air-exposed metal surfaces," *Applied Physics A,* vol. 76, no. 7, pp. 1085-1091, 2003/05/01 2003, doi: 10.1007/s00339-002-1667-2.

[65] H.-B. Zhang, X.-C. Hu, R. Wang, M. Cao, N. Zhang, and W.-Z. Cui, "Note: Measuring effects of Ar-ion cleaning on the secondary electron yield of copper due to electron impact," *Review of Scientific Instruments,* vol. 83, no. 6, p. 066105, 2012/06/01 2012, doi: 10.1063/1.4729379.

[66] I. Bojko, N. Hilleret, and C. Scheuerlein, "Influence of air exposures and thermal treatments on the secondary electron yield of copper," *Journal of Vacuum Science & Technology A,* vol. 18, no. 3, pp. 972-979, 2000/05/01 2000, doi: 10.1116/1.582286.

[67] H. B. Zhang, X. C. Hu, M. Cao, N. Zhang, and W. Z. Cui, "The quantitative effect of thermal treatment on the secondary electron yield from air-exposed silver surface," (in English), *Vacuum,* Article vol. 102, pp. 12-15, Apr 2014, doi: 10.1016/j.vacuum.2013.10.020.

[68] V. Petit, M. Taborelli, H. Neupert, P. Chiggiato, and M. Belhaj, "Role of the different chemical components in the conditioning process of air exposed copper surfaces," *Physical Review Accelerators and Beams,* vol. 22, no. 8, p. 083101, 08/09/ 2019, doi: 10.1103/PhysRevAccelBeams.22.083101.

[69] R. Cimino *et al.*, "Nature of the Decrease of the Secondary-Electron Yield by Electron Bombardment and its Energy Dependence," *Physical Review Letters,* vol. 109, no. 6, p. 064801, 08/10/ 2012, doi: 10.1103/PhysRevLett.109.064801.

[70] C. Scheuerlein and M. Taborelli, "Electron stimulated carbon adsorption in ultrahigh vacuum monitored by Auger electron spectroscopy," *Journal of Vacuum Science & Technology A,* vol. 20, no. 1, pp. 93-101, 2002/01/01 2002, doi: 10.1116/1.1424273.

[71] M. Nishiwaki and S. Kato, "Influence of electron irradiation and heating on secondary electron yields from non-evaporable getter films observed with in situ x-ray photoelectron spectroscopy," *Journal of Vacuum Science & Technology A,* vol. 25, no. 4, pp. 675-679, 2007/07/01 2007, doi: 10.1116/1.2738491.

[72] L. Calliari, M. Filippi, and N. Laidani, "Electron beam irradiation of hydrogenated amorphous carbon films," *Surface and Interface Analysis,* vol. 36, no. 8, pp. 1126-1129, 2004/08/01 2004, doi: 10.1002/sia.1856.

[73] O. Guise, H. Marbach, J. Levy, J. Ahner, and J. T. Yates, "Electron-beam-induced deposition of carbon films on Si(100) using chemisorbed ethylene as a precursor molecule," *Surface Science,* vol. 571, no. 1, pp. 128-138, 2004/11/01/ 2004, doi: https://doi.org/10.1016/j.susc.2004.07.053.

[74] R. Larciprete, D. R. Grosso, M. Commisso, R. Flammini, and R. Cimino, "Secondary electron yield of Cu technical surfaces: Dependence on electron irradiation," (in English), *Physical*

Review Special Topics-Accelerators and Beams, Article vol. 16, no. 1, p. 7, Jan 2013, Art no. 011002, doi: 10.1103/PhysRevSTAB.16.011002.

[75] R. Larciprete, D. R. Grosso, A. Di Trolio, and R. Cimino, "Evolution of the secondary electron emission during the graphitization of thin C films," (in English), *Applied Surface Science,* Article vol. 328, pp. 356-360, Feb 2015, doi: 10.1016/j.apsusc.2014.12.046.

[76] J. Vague *et al.*, "Multipactor Effect Characterization of Dielectric Materials for Space Applications," *IEEE Transactions on Microwave Theory and Techniques,* vol. 66, no. 8, pp. 3644-3655, 2018, doi: 10.1109/TMTT.2018.2845869.

[77] C. Perrin *et al.*, "Space charge detection in Kapton (R) and PTFE polymer films by the open Pulsed Electro-Acoustic method," (in English), *High Performance Polymers,* Article; Proceedings Paper vol. 20, no. 4-5, pp. 535-548, Aug-Oct 2008, doi: 10.1177/0954008308089714.

[78] C. L. Bungay, T. E. Tiwald, M. J. Devries, B. J. Dworak, and J. A. Woollam, "Characterization of UV irradiated space application polymers by spectroscopic ellipsometry," (in English), *Polymer Engineering and Science,* Article vol. 40, no. 2, pp. 300-309, Feb 2000, doi: 10.1002/pen.11163.

[79] E. Plis, D. Engelhart, R. Cooper, W. Johnston, D. Ferguson, and R. Hoffmann, "Review of Radiation-Induced Effects in Polyimide," *Applied Sciences,* vol. 9, p. 1999, 05/16 2019, doi: 10.3390/app9101999.

[80] I. Montero *et al.*, "SEY of Chromate-Free Treatments of Aluminum for RF Devices," in *Whorkshop Multipactor, Corona and Passive Intermodulation, MULCOPIM 14* ESA, ESTEC, Noordwijk, Netherland, ESA, Ed., April 2017 2014.

[81] L. S. Aguilera Maestro, "Supresión del efecto multipactor en instrumentación de RF en misiones en el espacio mediante superficies nano y microestructuradas," Universidad Autónoma de Madrid, 2014. [Online]. Available: http://hdl.handle.net/10486/663388

[82] L. A. González Gómez, "Practical Control of Multipactor Threshold and Insertion Losses on RF Satellite Devices and Study of Secondary Electron Emission for Multipactor and Electron Cloud Mitigation," Universidad Autónoma de Madrid, 2015. [Online]. Available: http://hdl.handle.net/10486/674719

[83] V. C. Nistor, "New approaches to anti-multipactor coatings for space applications," Universidad Autónoma de Madrid, 2016. [Online]. Available: http://hdl.handle.net/10486/672118

[84] P. He, H. C. Hseuh, M. Mapes, R. Todd, and D. Weiss, "Development of titanium nitride coating for SNS ring vacuum chambers," in *PACS2001. Proceedings of the 2001 Particle Accelerator Conference (Cat. No.01CH37268)*, 18-22 June 2001 2001, vol. 3, pp. 2159-2161 vol.3, doi: 10.1109/PAC.2001.987309.

[85] S. I. Castañeda, N. Díaz, D. Raboso, I. Montero, L. Galán, and F. Rueda, "Effects of air exposure on ion beam assisted TiN:O coatings to prevent multipactor," *Journal of Vacuum Science & Technology A,* vol. 21, no. 6, pp. 2007-2012, 2003, doi: 10.1116/1.1621403.

[86] A. Ruiz *et al.*, "UHV reactive evaporation growth of titanium nitride thin films, looking for multipactor effect suppression in space applications," *Vacuum,* vol. 81, no. 11, pp. 1493-1497, 2007/08/28/ 2007, doi: https://doi.org/10.1016/j.vacuum.2007.04.007.

[87] Y. Suetsugu, K. Kanazawa, K. Shibata, and H. Hisamatsu, "Continuing study on the photoelectron and secondary electron yield of TiN coating and NEG (Ti–Zr–V) coating under intense photon irradiation at the KEKB positron ring," *Nuclear Instruments and Methods in Physics Research Section A: Accelerators, Spectrometers, Detectors and Associated Equipment,* vol. 556, no. 2, pp. 399-409, 2006/01/15/ 2006, doi: https://doi.org/10.1016/j.nima.2005.10.113.

[88] Y. Suetsugu, K. Kanazawa, K. Shibata, and H. Hisamatsu, "Continued study on photoelectron and secondary electron yields of tin and NEG (Ti-Zr-V) coatings at the KEKB positron ring," in *2007 IEEE Particle Accelerator Conference (PAC)*, 25-29 June 2007 2007, pp. 4054-4056, doi: 10.1109/PAC.2007.4439958.

[89] Y. Suetsugu *et al.*, "First experimental and simulation study on the secondary electron and photoelectron yield of NEG materials (Ti–Zr–V) coating under intense photon irradiation," *Nuclear Instruments and Methods in Physics Research Section A: Accelerators, Spectrometers, Detectors and Associated Equipment,* vol. 554, no. 1, pp. 92-113, 2005/12/01/ 2005, doi: https://doi.org/10.1016/j.nima.2005.08.061.

[90] J. M. Ripalda, I. Montero, L. Vázquez, D. Raboso, and L. Galán, "Secondary electron emission and photoemission studies on surface films of carbon nitride," *Journal of Applied Physics,* vol. 99, no. 4, p. 043513, 2006, doi: 10.1063/1.2173307.

[91] A. Santos, N. Bundaleski, B. J. Shaw, A. G. Silva, and O. Teodoro, "Increase of secondary electron yield of amorphous carbon coatings under high vacuum conditions," (in English), *Vacuum,* Article vol. 98, pp. 37-40, Dec 2013, doi: 10.1016/j.vacuum.2012.11.005.

[92] V. C. Y. *et al.*, "Amorphous carbon coatings for the mitigation of electron cloud in the CERN Super Proton Synchrotron," *Phys. Rev. ST Accel. Beams,* vol. 14, p. 071001, 2011.

[93] M. Nishiwaki and S. Kato, "Graphitization of inner surface of copper beam duct of KEKB positron ring," *Vacuum,* vol. 84, no. 5, pp. 743-746, 2009/12/10/ 2009, doi: https://doi.org/10.1016/j.vacuum.2009.06.028.

[94] Q. Lu *et al.*, "Surface roughness evolution induced low secondary electron yield in carbon coated Ag/Al substrates for space microwave devices," *Applied Surface Science,* vol. 501, p. 144236, 2020/01/31/ 2020, doi: https://doi.org/10.1016/j.apsusc.2019.144236.

[95] I. Montero *et al.*, "Secondary electron emission under electron bombardment from graphene nanoplatelets," (in English), *Applied Surface Science,* Article vol. 291, pp. 74-77, Feb 2014, doi: 10.1016/j.apsusc.2013.10.045.

[96] M. Cao, X.-S. Zhang, W.-H. Liu, H.-G. Wang, and Y.-D. Li, "Secondary electron emission of graphene-coated copper," *Diamond and Related Materials,* vol. 73, pp. 199-203, 2017/03/01/ 2017, doi: https://doi.org/10.1016/j.diamond.2016.09.019.

[97] L. Aguilera *et al.*, "CuO nanowires for inhibiting secondary electron emission," (in English), *Journal of Physics D-Applied Physics,* Article vol. 46, no. 16, p. 6, Apr 2013, Art no. 165104, doi: 10.1088/0022-3727/46/16/165104.

[98] C. G. Jin, A. Ottaviano, and Y. Raitses, "Secondary electron emission yield from high aspect ratio carbon velvet surfaces," (in English), *Journal of Applied Physics,* Article vol. 122, no. 17, p. 5, Nov 2017, Art no. 173301, doi: 10.1063/1.4993979.

[99] B. Wood, J. Lee, G. Wilson, T. Shen, and J. R. Dennison, "Secondary Electron Yield Measurements of Carbon Nanotube Forests: Dependence on Morphology and Substrate," *IEEE Transactions on Plasma Science,* vol. 47, no. 8, pp. 3801-3809, 2019, doi: 10.1109/TPS.2019.2921505.

[100] M. K. Alam, P. Yaghoobi, M. Chang, and A. Nojeh, "Secondary electron yield of multiwalled carbon nanotubes," *Applied Physics Letters,* vol. 97, no. 26, p. 261902, 2010, doi: 10.1063/1.3532851.

[101] Y. Raitses, D. Staack, A. Dunaevsky, and N. J. Fisch, "Operation of a segmented Hall thruster with low-sputtering carbon-velvet electrodes," *Journal of Applied Physics,* vol. 99, no. 3, p. 036103, 2006, doi: 10.1063/1.2168023.

[102] M. Pivi, F. K. King, R. E. Kirby, T. O. Raubenheimer, G. Stupakov, and F. Le Pimpec, "Sharp reduction of the secondary electron emission yield from grooved surfaces," (in English), *Journal of Applied Physics,* Article vol. 104, no. 10, p. 10, Nov 2008, Art no. 104904, doi: 10.1063/1.3021149.

[103] C. E. Huerta, M. I. Patino, and R. E. Wirz, "Secondary electron emission from textured surfaces," (in English), *Journal of Physics D-Applied Physics,* Article vol. 51, no. 14, p. 8, Apr 2018, Art no. 145202, doi: 10.1088/1361-6463/aab1ac.

[104] C. Swanson and I. D. Kaganovich, "Modeling of reduced secondary electron emission yield from a foam or fuzz surface," (in English), *Journal of Applied Physics,* Article vol. 123, no. 2, p. 6, Jan 2018, Art no. 023302, doi: 10.1063/1.5008261.

[105] J. Kawata, K. Ohya, and K. Nishimura, "Simulation of secondary electron emission from rough surfaces," *Journal of Nuclear Materials,* vol. 220-222, pp. 997-1000, 1995/04/01/ 1995, doi: https://doi.org/10.1016/0022-3115(94)00460-9.

[106] MingYe, PengFeng, YunLi, DanWang, YongningHe, and WanzhaoCui, "The total secondary electron yield of a conductive random rough surface," *Journal of Applied Physics,* vol. 125, no. 4, p. 043301, 2019, doi: 10.1063/1.5023769.

[107] M. Cao, N. Zhang, T.-C. Hu, F. Wang, and W.-Z. Cui, "Secondary electron emission from rough metal surfaces: a multi-generation model," *Journal of Physics D: Applied Physics,* vol. 48, no. 5, p. 055501, 2015/01/19 2015, doi: 10.1088/0022-3727/48/5/055501.

[108] MingYe, DanWang, and YongningHe, "Mechanism of total electron emission yield reduction using a micro-porous surface," *Journal of Applied Physics,* vol. 121, no. 12, p. 124901, 2017, doi: 10.1063/1.4978760.

[109] C. Swanson and I. D. Kaganovich, ""“Feathered” fractal surfaces to minimize secondary electron emission for a wide range of incident angles," *Journal of Applied Physics,* vol. 122, no. 4, p. 043301, 2017, doi: 10.1063/1.4995535.

[110] L. Wang, T. O. Raubenheimer, and G. Stupakov, "Suppression of secondary emission in a magnetic field using triangular and rectangular surfaces," *Nuclear Instruments and Methods in Physics Research Section A: Accelerators, Spectrometers, Detectors and Associated Equipment,* vol. 571, no. 3, pp. 588-598, 2007/02/11/ 2007, doi: https://doi.org/10.1016/j.nima.2006.11.039.

[111] K. Nishimura, T. Itotani, and K. Ohya, "Influence of Surface Roughness on Secondary Electron Emission and Electron Backscattering from Metal Surface," *Japanese Journal of Applied Physics,* vol. 33, no. Part 1, No. 8, pp. 4727-4734, 1994/08/15 1994, doi: 10.1143/jjap.33.4727.

[112] M. Ye *et al.*, "Suppression of secondary electron yield by micro-porous array structure," *Journal of Applied Physics,* vol. 113, no. 7, p. 074904, 2013, doi: 10.1063/1.4792514.

[113] DanWang, YongningHe, MingYe, WenboPeng, and WanzhaoCui, "Secondary electron emission characteristics of nanostructured silver surfaces," *Journal of Applied Physics,* vol. 122, no. 15, p. 153302, 2017, doi: 10.1063/1.4989965.

[114] Y. N. He *et al.*, "Thermal evaporated hyperbranched Ag nanostructure as an effective secondary-electron trapping surface coating," *AIP Advances,* vol. 6, no. 2, p. 025122, 2016, doi: 10.1063/1.4943050.

[115] R. Valizadeh, O. B. Malyshev, S. Wang, T. Sian, M. D. Cropper, and N. Sykes, "Reduction of secondary electron yield for E-cloud mitigation by laser ablation surface engineering," (in English), *Applied Surface Science,* Article vol. 404, pp. 370-379, May 2017, doi: 10.1016/j.apsusc.2017.02.013.

[116] R. Valizadeh, O. B. Malyshev, S. Wang, S. A. Zolotovskaya, W. A. Gillespie, and A. Abdolvand, "Low secondary electron yield engineered surface for electron cloud mitigation," *Applied Physics Letters,* vol. 105, no. 23, p. 231605, 2014, doi: 10.1063/1.4902993.

[117] C. Watts, M. Gilmore, and E. Schamiloglu, "Effects of Laser Surface Modification on Secondary Electron Emission of Copper," *IEEE Transactions on Plasma Science,* vol. 39, no. 3, pp. 836-841, 2011, doi: 10.1109/TPS.2010.2102750.

[118] D. Bajek *et al.*, "Role of surface microgeometries on electron escape probability and secondary electron yield of metal surfaces," *Scientific Reports,* vol. 10, no. 1, p. 250, 2020/01/14 2020, doi: 10.1038/s41598-019-57160-w.

[119] M. Patino, Y. Raitses, and R. Wirz, "Secondary electron emission from plasma-generated nanostructured tungsten fuzz," *Applied Physics Letters,* vol. 109, no. 20, p. 201602, 2016, doi: 10.1063/1.4967830.

[120] Y. S. Ow, S. Azimi, M. B. H. Breese, E. J. Teo, and D. Mangaiyarkarasi, "Effects of focused MeV ion beam irradiation on the roughness of electrochemically micromachined silicon surfaces," *Journal of Vacuum Science & Technology B,* vol. 28, no. 3, pp. 500-505, 2010, doi: 10.1116/1.3406130.

[121] J. Xu, C.-j. Wang, B. Guo, D.-b. Shan, Y. Sugiyama, and S. Ono, "Surface finish of micro punch with ion beam irradiation," *Transactions of Nonferrous Metals Society of China,* vol. 19, pp. s526-s530, 2009/09/01/ 2009, doi: https://doi.org/10.1016/S1003-6326(10)60102-1.

[122] İ. Tanyeli, L. Marot, D. Mathys, M. C. M. van de Sanden, and G. De Temmerman, "Surface Modifications Induced by High Fluxes of Low Energy Helium Ions," *Scientific Reports,* vol. 5, no. 1, p. 9779, 2015/04/28 2015, doi: 10.1038/srep09779.

[123] G. D. Temmerman *et al.*, "Nanostructuring of molybdenum and tungsten surfaces by low-energy helium ions," *Journal of Vacuum Science & Technology A,* vol. 30, no. 4, p. 041306, 2012, doi: 10.1116/1.4731196.

[124] X.-C. Hu, M. Cao, and W.-Z. Cui, "Influence of surface topography on the secondary electron yield of clean copper samples," *Micron,* vol. 90, pp. 71-77, 2016/11/01/ 2016, doi: https://doi.org/10.1016/j.micron.2016.08.008.

[125] I. Montero, L. Aguilera, D. Raboso, and U. Wochner, "Anti-multipactor device," Patent WO2016042192 A1, 2016-03-24, 2016. [Online]. Available: http://hdl.handle.net/10261/135730

[126] V. Nistor *et al.*, "Multipactor suppression by micro-structured gold/silver coatings for space applications," (in English), *Applied Surface Science,* Article vol. 315, pp. 445-453, Oct 2014, doi: 10.1016/j.apsusc.2014.05.049.

[127] D. Wu *et al.*, "Fabrication of Porous Ag/TiO2/Au Coatings with Excellent Multipactor Suppression," *Scientific Reports,* vol. 7, no. 1, p. 43749, 2017/03/10 2017, doi: 10.1038/srep43749.

[128] S. Calatroni *et al.*, "First accelerator test of vacuum components with laser-engineered surfaces for electron-cloud mitigation," *Physical Review Accelerators and Beams,* vol. 20, no. 11, p. 113201, 11/20/ 2017, doi: 10.1103/PhysRevAccelBeams.20.113201.

[129] R. Salemme *et al.*, "First beam test of Laser Engineered Surface Structures (LESS) at cryogenic temperature in C ERN SPS accelerator," *Journal of Physics: Conference Series,* vol. 1067, p. 082017, 2018/09 2018, doi: 10.1088/1742-6596/1067/8/082017.

[130] J. Cazaux, "About the secondary electron yield and the sign of charging of electron irradiated insulators," (in English), *European Physical Journal-Applied Physics,* Article vol. 15, no. 3, pp. 167-172, Sep 2001, doi: 10.1051/epjap:2001178.

[131] J. Cazaux, "e-Induced secondary electron emission yield of insulators and charging effects," (in English), *Nuclear Instruments & Methods in Physics Research Section B-Beam Interactions with Materials and Atoms,* Article vol. 244, no. 2, pp. 307-322, Mar 2006, doi: 10.1016/j.nimb.2005.10.006.

[132] J. Cazaux, "Secondary electron emission and charging mechanisms in Auger Electron Spectroscopy and related e-beam techniques," (in English), *Journal of Electron Spectroscopy and Related Phenomena,* Article vol. 176, no. 1-3, pp. 58-79, Jan 2010, doi: 10.1016/j.elspec.2009.06.004.

[133] J. Cazaux, V. J. P., D. L. P., L. M. A., L. G. C., and G. D. L., "Some considerations on the electric field induced in insulators by electron bombardment," *Journal of Applied Physics,* vol. 59, no. 5, pp. 1418-1430, 1986, doi: 10.1063/1.336493.

[134] A. Melchinger, S. Hofmann, and W. W., "Dynamic double layer model: Description of time dependent charging phenomena in insulators under electron beam irradiation," *Journal of Applied Physics,* vol. 78, no. 10, pp. 6224-6232, 1995, doi: 10.1063/1.360569.

[135] F. C. Chiu, "A Review on Conduction Mechanisms in Dielectric Films," (in English), *Advances in Materials Science and Engineering,* Review p. 18, 2014, Art no. 578168, doi: 10.1155/2014/578168.

[136] T. Chiang and J. F. Wager, "Electronic Conduction Mechanisms in Insulators," *IEEE Transactions on Electron Devices,* vol. 65, no. 1, pp. 223-230, 2018, doi: 10.1109/TED.2017.2776612.

[137] K. C. Kao, *Dielectric Phenomena in Solids*. Elsevier Science, 2004.

[138] J. Cazaux, "Mechanisms of charging in electron spectroscopy," *Journal of Electron Spectroscopy and Related Phenomena,* vol. 105, no. 2, pp. 155-185, 1999/12/01/ 1999, doi: https://doi.org/10.1016/S0368-2048(99)00068-7.

[139] M. Weng, M. Cao, H.-J. Zhao, and H.-B. Zhang, "Note: A simple charge neutralization method for measuring the secondary electron yield of insulators," *Review of Scientific Instruments,* vol. 85, no. 3, p. 036108, 2014/03/01 2014, doi: 10.1063/1.4869139.

[140] S. Ichimura, H. E. Bauer, H. Seiler, and S. Hofmann, "Reduction of charging in surface analysis of insulating materials by AES," *Surface and Interface Analysis,* vol. 14, no. 5, pp. 250-256, 1989/05/01 1989, doi: 10.1002/sia.740140507.

[141] D. R. Baer *et al.*, "Approaches to analyzing insulators with Auger electron spectroscopy: Update and overview," *Journal of Electron Spectroscopy and Related Phenomena,* vol. 176, no. 1, pp. 80-94, 2010/01/01/ 2010, doi: https://doi.org/10.1016/j.elspec.2009.03.021.

[142] S. Hofmann, "Charging and charge compensation in AES analysis of insulators," *Journal of Electron Spectroscopy and Related Phenomena,* vol. 59, no. 1, pp. 15-32, 1992/06/15/ 1992, doi: https://doi.org/10.1016/0368-2048(92)85009-V.

[143] P. E. Larson and M. A. Kelly, "Surface charge neutralization of insulating samples in x-ray photoemission spectroscopy," *Journal of Vacuum Science & Technology A,* vol. 16, no. 6, pp. 3483-3489, 1998, doi: 10.1116/1.581507.

[144] K. J. Handel, A. S. Jensen, and M. P. Siedband, "A two electron gun technique for the measurement of secondary emission characteristics of a variety of materials," *IEEE Transactions on Electron Devices,* vol. ED-13, no. 6, pp. 525-528, 1966, doi: 10.1109/T-ED.1966.15725.

[145] J. R. Dennison, A. Sim, and C. D. Thomson, "Evolution of the electron yield curves of insulators as a function of impinging electron fluence and energy," (in English), *Ieee Transactions on Plasma Science,* Article; Proceedings Paper vol. 34, no. 5, pp. 2204-2218, Oct 2006, doi: 10.1109/tps.2006.883398.

[146] C. D. Thomson, "Measurements of the Secondary Electron Emission Properties of Insulators," 2005. [Online]. Available: http://digitalcommons.usu.edu/etd/2093

[147] R. Hoffmann and J. R. Dennison, "Measurement Methods of Electron Emission Over a Full Range of Sample Charging," (in English), *Ieee Transactions on Plasma Science,* Article vol. 40, no. 2, pp. 298-304, Feb 2012, doi: 10.1109/tps.2011.2178251.

[148] R. Hoffmann, J. R. Dennison, C. D. Thomson, and J. Albretsen, "Low-Fluence Electron Yields of Highly Insulating Materials," *IEEE Transactions on Plasma Science,* vol. 36, no. 5, pp. 2238-2245, 2008, doi: 10.1109/TPS.2008.2004226.

[149] M. Belhaj, T. Tondu, V. Inguimbert, and J. P. Chardon, "A Kelvin probe based method for measuring the electron emission yield of insulators and insulated conductors subjected to electron irradiation," *Journal of Physics D: Applied Physics,* vol. 42, no. 10, p. 105309, 2009/04/30 2009, doi: 10.1088/0022-3727/42/10/105309.

[150] J. Cazaux, "About the charge compensation of insulating samples in XPS," *Journal of Electron Spectroscopy and Related Phenomena,* vol. 113, no. 1, pp. 15-33, 2000/12/01/ 2000, doi: https://doi.org/10.1016/S0368-2048(00)00190-0.

[151] I. L. Krainsky and G. G. Lesny, "Simple device for monitoring secondary electron emission of materials in the pulse mode," *Review of Scientific Instruments,* vol. 69, no. 4, pp. 1916-1917, 1998/04/01 1998, doi: 10.1063/1.1149170.

[152] A. D. Bass, P. Cloutier, and L. Sanche, "Measurements of charge accumulation induced by monochromatic low-energy electrons at the surface of insulating samples," *Journal of Applied Physics,* vol. 84, no. 5, pp. 2740-2748, 1998/09/01 1998, doi: 10.1063/1.368388.

[153] C. W. Mueller, "The Secondary Electron Emission of Pyrex Glass," *Journal of Applied Physics,* vol. 16, no. 8, pp. 453-458, 1945/08/01 1945, doi: 10.1063/1.1707614.

[154] "Kapton HN." https://www.dupont.com/products/kapton-hn.html (accessed 28 November, 2020).

[155] "Teflon." http://www.tetrachim.com/pdf/Teflon_industrialcoatingsbrochure_GB.pdf (accessed 28 November, 2020).
[156] "Ultem 1000F." https://www.sabic.com/en/products/specialties/ultem-resins/ultem-resin (accessed 28 November, 2020).
[157] W. M. Haynes, *CRC Handbook of Chemistry and Physics*. CRC Press, 2016.
[158] H. J. Hopman, H. Alberda, I. Attema, H. Zeijlemaker, and J. Verhoeven, "Measuring the secondary electron emission characteristic of insulators," *Journal of Electron Spectroscopy and Related Phenomena,* vol. 131-132, pp. 51-60, 2003/10/01/ 2003, doi: https://doi.org/10.1016/S0368-2048(03)00091-4.
[159] A. M. Donald, "The use of environmental scanning electron microscopy for imaging wet and insulating materials," *Nature Materials,* vol. 2, no. 8, pp. 511-516, 2003/08/01 2003, doi: 10.1038/nmat898.
[160] NOAA. Satellite Anomalies [Online] Available: https://www.ngdc.noaa.gov/stp/satellite/anomaly/satelliteanomaly.html
[161] C. R. Francis, "Electrostatic charging problems of spacecraft," *J. Electrost.,* vol. 11, no. 3, pp. 265-280, 1982/02/01/ 1982, doi: https://doi.org/10.1016/0304-3886(82)90017-1.
[162] N. STEVENS, A. ROSEN, and G. INOUYE, "Communication satellite experience in the seventies," in *25th AIAA Aerospace Sciences Meeting*, 1987.
[163] R. D. Leach and M. B. Alexander, *Failures and Anomalies Attributed to Spacecraft Charging*. National Aeronautics and Space Administration, Marshall Space Flight Center, 1995.
[164] J. R. Dennison, "Dynamic Interplay Between Spacecraft Charging, Space Environment Interactions, and Evolving Materials," (in English), *Ieee Transactions on Plasma Science,* Article; Proceedings Paper vol. 43, no. 9, pp. 2933-2940, Sep 2015, doi: 10.1109/tps.2015.2434947.
[165] H. Garrett and A. Whittlesey, "Guide to Mitigating Spacecraft Charging Effects," *Guide to Mitigating Spacecraft Charging Effects,* 05/04 2012, doi: 10.1002/9781118241400.
[166] A. B. Zaid, T. Paulmier, P. Sarrailh, B. Dirassen, R. Rey, and D. Payan, "Experimental and Numerical Study of Internal Charging on Spacecraft and Risks of Discharge on Floating Metallic Elements," *IEEE Transactions on Nuclear Science,* vol. 67, no. 1, pp. 191-200, 2020, doi: 10.1109/TNS.2019.2958368.
[167] P. Lundgreen and J. R. Dennison, "Strategies for Determining Electron Yield Material Parameters for Spacecraft Charge Modeling," *Space Weather,* vol. 18, no. 4, p. e2019SW002346, 2020, doi: 10.1029/2019sw002346.
[168] J. Mateo-Velez, M. Belhaj, S. Dadouch, P. Sarrailh, S. L. G. Hess, and D. Payan, "Spacecraft Worst Case Surface Charging: On the Importance of Measuring the Electron Emission Yield Under Representative Environmental Conditions," *IEEE Transactions on Plasma Science,* vol. 47, no. 8, pp. 3790-3795, 2019, doi: 10.1109/TPS.2019.2925435.
[169] D. C. Ferguson, S. P. Worden, and D. E. Hastings, "The Space Weather Threat to Situational Awareness, Communications, and Positioning Systems," *IEEE Transactions on Plasma Science,* vol. 43, no. 9, pp. 3086-3098, 2015, doi: 10.1109/TPS.2015.2412775.
[170] T. Paulmier, B. Dirassen, D. Payan, and M. V. Eesbeek, "Material Charging in Space Environment: Experimental Test Simulation and Induced Conductive Mechanisms," *IEEE Transactions on Dielectrics and Electrical Insulation,* vol. 16, no. 3, pp. 682-688, 2009, doi: 10.1109/TDEI.2009.5128506.
[171] N. Balcon, D. Payan, M. Belhaj, T. Tondu, and V. Inguimbert, "Secondary Electron Emission on Space Materials: Evaluation of the Total Secondary Electron Yield From Surface Potential Measurements," (in English), *Ieee Transactions on Plasma Science,* Article vol. 40, no. 2, pp. 282-290, Feb 2012, doi: 10.1109/tps.2011.2172636.
[172] A. Georgescu, A. V. Gheorghe, M. I. Piso, and P. F. Katina, *Critical Space Infrastructures: Risk, Resilience and Complexity*. Springer International Publishing, 2019.

[173] R. B. Horne *et al.*, "Space weather impacts on satellites and forecasting the Earth's electron radiation belts with SPACECAST," *Space Weather,* vol. 11, no. 4, pp. 169-186, 2013, doi: 10.1002/swe.20023.
[174] UCS Satellite Database [Online] Available: https://www.ucsusa.org/resources/satellite-database
[175] B. M. Jakosky, "MAVEN observations of the Mars upper atmosphere, ionosphere, and solar wind interactions," *Journal of Geophysical Research: Space Physics,* vol. 122, no. 9, pp. 9552-9553, 2017, doi: 10.1002/2017ja024324.
[176] D. F. Mitchell, "The Mars Atmosphere and Volatile Evolution mission," in *2010 IEEE Aerospace Conference*, 6-13 March 2010 2010, pp. 1-7, doi: 10.1109/AERO.2010.5446986.
[177] D. Müller, I. Zouganelis, O. C. St. Cyr, H. R. Gilbert, and T. Nieves-Chinchilla, "Europe's next mission to the Sun," *Nature Astronomy,* vol. 4, no. 2, pp. 205-205, 2020/02/01 2020, doi: 10.1038/s41550-020-1015-5.
[178] D. Müller, R. G. Marsden, O. C. St. Cyr, H. R. Gilbert, and T. The Solar Orbiter, "Solar Orbiter," *Solar Physics,* vol. 285, no. 1, pp. 25-70, 2013/07/01 2013, doi: 10.1007/s11207-012-0085-7.
[179] R. D. Lange, "Cassini-Huygens Mission Overview and Recent Science Results," in *2008 IEEE Aerospace Conference*, 1-8 March 2008 2008, pp. 1-10, doi: 10.1109/AERO.2008.4526259.
[180] N. J. Fox *et al.*, "The Solar Probe Plus Mission: Humanity's First Visit to Our Star," *Space Science Reviews,* vol. 204, no. 1, pp. 7-48, 2016/12/01 2016, doi: 10.1007/s11214-015-0211-6.
[181] A. Szabo, "Flying into the Sun," *Nature Astronomy,* vol. 2, no. 10, pp. 829-829, 2018/10/01 2018, doi: 10.1038/s41550-018-0580-3.
[182] M. F. Diaz-Aguado *et al.*, "Experimental Investigation of the Secondary and Backscatter Electron Emission from Spacecraft Materials," *Journal of Spacecraft and Rockets,* vol. 0, no. 0, pp. 1-16, doi: 10.2514/1.a34655.
[183] C. Gutton, "Sur la décharge électrique à fréquence très élevée," *Comptes-Rendus Hebdomadaires des Séances de l'Académie des Sciences,* vol. 178, 1924.
[184] J. de Lara *et al.*, "Multipactor prediction for on-board spacecraft RF equipment with the MEST software tool," (in English), *Ieee Transactions on Plasma Science,* Article vol. 34, no. 2, pp. 476-484, Apr 2006, doi: 10.1109/tps.2006.872450.
[185] J. R. M. Vaughan, "MULTIPACTOR," (in English), *Ieee Transactions on Electron Devices,* Article vol. 35, no. 7, pp. 1172-1180, Jul 1988, doi: 10.1109/16.3387.
[186] D. Gonzalez-Iglesias *et al.*, "Analysis of Multipactor RF Breakdown in a Waveguide Containing a Transversely Magnetized Ferrite," (in English), *Ieee Transactions on Electron Devices,* Article vol. 63, no. 12, pp. 4939-4947, Dec 2016, doi: 10.1109/ted.2016.2614370.
[187] S. A. Rice and J. P. Verboncoeur, "A Comparison of Multipactor Predictions Using Two Popular Secondary Electron Models," (in English), *Ieee Transactions on Plasma Science,* Article vol. 42, no. 6, pp. 1484-1487, Jun 2014, doi: 10.1109/tps.2014.2321118.
[188] R. A. Kishek, Y. Y. Lau, L. K. Ang, A. Valfells, and R. M. Gilgenbach, "Multipactor discharge on metals and dielectrics: Historical review and recent theories," (in English), *Physics of Plasmas,* Article; Proceedings Paper vol. 5, no. 5, pp. 2120-2126, May 1998, doi: 10.1063/1.872883.
[189] F. Piro and Y. Brand, "PIM and multipactor considerations for future high-RF power space missions," in *The 8th European Conference on Antennas and Propagation (EuCAP 2014)*, 6-11 April 2014 2014, pp. 1643-1646, doi: 10.1109/EuCAP.2014.6902102.
[190] S. Anza *et al.*, "Prediction of Multipactor Breakdown for Multicarrier Applications: The Quasi-Stationary Method," (in English), *Ieee Transactions on Microwave Theory and Techniques,* Article vol. 60, no. 7, pp. 2093-2105, Jul 2012, doi: 10.1109/tmtt.2012.2197021.
[191] Y. Li *et al.*, "Three-dimensional simulation method of multipactor in microwave components for high-power space application," (in English), *Chinese Physics B,* Article vol. 23, no. 4, p. 8, Apr 2014, Art no. 048402, doi: 10.1088/1674-1056/23/4/048402.

[192] Y. Li, W.-Z. Cui, and H.-G. Wang, "Simulation investigation of multipactor in metal components for space application with an improved secondary emission model," *Physics of Plasmas,* vol. 22, no. 5, p. 053108, 2015/05/01 2015, doi: 10.1063/1.4919858.
[193] E. Bronchalo *et al.*, "Secondary Electron Emission of Pt: Experimental Study and Comparison With Models in the Multipactor Energy Range," *IEEE Transactions on Electron Devices,* vol. 63, no. 8, pp. 3270-3277, 2016, doi: 10.1109/TED.2016.2580199.
[194] Y. Li, D. Wang, M. Yu, Y. He, and W. Cui, "Experimental Verification of Multipactor Discharge Dynamics Between Ferrite Dielectric and Metal," *IEEE Transactions on Electron Devices,* vol. 65, no. 10, pp. 4592-4599, 2018, doi: 10.1109/TED.2018.2865164.
[195] A. Plaçais, M. Belhaj, J. Hillairet, and J. Puech, "POTOMAC: Towards a Realistic Secondary and Backscattered Emission Model for the Multipactor," in *2019 IEEE Pulsed Power & Plasma Science (PPPS)*, 23-29 June 2019 2019, pp. 1-4, doi: 10.1109/PPPS34859.2019.9009672.
[196] I. Montero *et al.*, "Low-secondary electron emission yield under electron bombardment of microstructured surfaces, looking for multipactor effect suppression," *Journal of Electron Spectroscopy and Related Phenomena,* vol. 241, p. 146822, 2020/05/01/ 2020, doi: https://doi.org/10.1016/j.elspec.2019.02.001.
[197] E. T. Tulu, U. van Rienen, and A. Arnold, "Systematic study of multipactor suppression techniques for a superconducting rf gun," *Physical Review Accelerators and Beams,* vol. 21, no. 11, p. 113402, 11/30/ 2018, doi: 10.1103/PhysRevAccelBeams.21.113402.
[198] C. R. *et al.*, "Can low-energy electrons affect high-energy physics accelerators?," *Phys. Rev. Lett.,* vol. 93, p. 014801, 2004.
[199] C. R., G. L., L. R., D. G. A., I. G., and R. G., "Detailed investigation of the low energy secondary electron yield of technical Cu and its relevance for the LHC," *Phys. Rev. ST Accel. Beams,* vol. 18, p. 051002, 2015.
[200] C. R. and D. T., "Electron cloud in accelerators," *Int. J. Mod. Phys. A,* vol. 29, p. 1430023, 2014.
[201] O. Dominguez *et al.*, "First electron-cloud studies at the Large Hadron Collider," (in English), *Physical Review Special Topics-Accelerators and Beams,* Article vol. 16, no. 1, p. 18, Jan 2013, Art no. 011003, doi: 10.1103/PhysRevSTAB.16.011003.
[202] O. Bruning *et al.*, "Electron cloud and beam scrubbing in the LHC," in *Proceedings of the 1999 Particle Accelerator Conference (Cat. No.99CH36366)*, 27 March-2 April 1999 1999, vol. 4, pp. 2629-2631 vol.4, doi: 10.1109/PAC.1999.792885.
[203] M. A. Furman, "Electron Cloud Effects in Accelerators," 2013, doi: 10.5170/CERN-2013-002.1.
[204] G. Rumolo, F. Ruggiero, and F. Zimmermann, "Simulation of the electron-cloud build up and its consequences on heat load, beam stability, and diagnostics," *Physical Review Special Topics - Accelerators and Beams,* vol. 4, no. 1, p. 012801, 01/08/ 2001, doi: 10.1103/PhysRevSTAB.4.012801.
[205] I. Levchenko *et al.*, "Space micropropulsion systems for Cubesats and small satellites: From proximate targets to furthermost frontiers," *Applied Physics Reviews,* vol. 5, no. 1, p. 011104, 2018, doi: 10.1063/1.5007734.
[206] I. Levchenko, S. Xu, G. Teel, D. Mariotti, M. L. R. Walker, and M. Keidar, "Recent progress and perspectives of space electric propulsion systems based on smart nanomaterials," *Nature Communications,* vol. 9, no. 1, p. 879, 2018/02/28 2018, doi: 10.1038/s41467-017-02269-7.
[207] A. Olano, J. Ren, G. Zhang, H. Tang, T. Zhang, and J. Li, "Improvements in miniaturized Hall Thrusters by use of high-temperature SmCo magnets and additive manufacturing techniques," *IOP Conference Series: Materials Science and Engineering,* vol. 576, p. 012002, 2019/08/07 2019, doi: 10.1088/1757-899x/576/1/012002.
[208] S. Mazouffre, "Electric propulsion for satellites and spacecraft: established technologies and novel approaches," *Plasma Sources Science and Technology,* vol. 25, no. 3, p. 033002, 2016/04/07 2016, doi: 10.1088/0963-0252/25/3/033002.
[209] A. O. Garcia, H. Tang, and J. Ren, "Scaling Model for SPT and TAL Thrusters," *IEEE Transactions on Plasma Science,* vol. 48, no. 1, pp. 86-98, 2020, doi: 10.1109/TPS.2019.2958187.

[210] J.-P. Boeuf, "Tutorial: Physics and modeling of Hall thrusters," *Journal of Applied Physics,* vol. 121, no. 1, p. 011101, 2017, doi: 10.1063/1.4972269.
[211] V. V. Zhurin, H. R. Kaufman, and R. S. Robinson, "Physics of closed drift thrusters," *Plasma Sources Science and Technology,* vol. 8, no. 1, pp. R1-R20, 1999/01/01 1999, doi: 10.1088/0963-0252/8/1/021.
[212] D. M. Goebel and I. Katz, *Fundamentals of Electric Propulsion: Ion and Hall Thrusters*. Wiley, 2008.
[213] D. Sydorenko, A. Smolyakov, I. Kaganovich, and Y. Raitses, "Plasma-sheath instability in Hall thrusters due to periodic modulation of the energy of secondary electrons in cyclotron motion," *Physics of Plasmas,* vol. 15, no. 5, p. 053506, 2008, doi: 10.1063/1.2918333.
[214] S. Langendorf and M. Walker, "Effect of secondary electron emission on the plasma sheath," *Physics of Plasmas,* vol. 22, no. 3, p. 033515, 2015, doi: 10.1063/1.4914854.
[215] E. Ahedo and V. D. Pablo, "Combined effects of electron partial thermalization and secondary emission in Hall thruster discharges," *Physics of Plasmas,* vol. 14, no. 8, p. 083501, 2007, doi: 10.1063/1.2749237.
[216] G. D. Hobbs and J. A. Wesson, "Heat flow through a Langmuir sheath in the presence of electron emission," *Plasma Physics,* vol. 9, no. 1, pp. 85-87, 1967/01/01 1967, doi: 10.1088/0032-1028/9/1/410.
[217] Y. Raitses, A. Smirnov, D. Staack, and N. J. Fisch, "Measurements of secondary electron emission effects in the Hall thruster discharge," *Phys. Plasmas,* vol. 13, no. 1, p. 014502, 2006, doi: 10.1063/1.2162809.
[218] D. Sydorenko, A. Smolyakov, I. Kaganovich, and Y. Raitses, "Kinetic simulation of secondary electron emission effects in Hall thrusters," *Physics of Plasmas,* vol. 13, no. 1, p. 014501, 2006, doi: 10.1063/1.2158698.
[219] Y. Raitses, I. D. Kaganovich, A. Khrabrov, D. Sydorenko, N. J. Fisch, and A. Smolyakov, "Effect of Secondary Electron Emission on Electron Cross-Field Current in $E \times B$ Discharges," *IEEE Transactions on Plasma Science,* vol. 39, no. 4, pp. 995-1006, 2011, doi: 10.1109/TPS.2011.2109403.
[220] Y. Raitses, D. Staack, M. Keidar, and N. J. Fisch, "Electron-wall interaction in Hall thrusters," *Physics of Plasmas,* vol. 12, no. 5, p. 057104, 2005, doi: 10.1063/1.1891747.
[221] V. Pigeon, N. Claire, C. Arnas, K. Terasaka, and S. Inagaki, "Plasma sheath material induced dependence due to secondary electron emission," *Physics of Plasmas,* vol. 27, no. 4, p. 043505, 2020, doi: 10.1063/1.5141348.
[222] A. Tavant, V. Croes, R. Lucken, T. Lafleur, A. Bourdon, and P. Chabert, "The effects of secondary electron emission on plasma sheath characteristics and electron transport in an ${\bf{E}}\times {\bf{B}}$ discharge via kinetic simulations," *Plasma Sources Science and Technology,* vol. 27, no. 12, p. 124001, 2018/12/21 2018, doi: 10.1088/1361-6595/aaeccd.
[223] E. Ahedo, "Presheath/sheath model with secondary electron emission from two parallel walls," *Physics of Plasmas,* vol. 9, no. 10, pp. 4340-4347, 2002, doi: 10.1063/1.1503798.
[224] P. C. Stangeby, *The plasma boundary of magnetic fusion devices*. Bristol ; Philadelphia : Institute of Physics Pub., 2000.
[225] P. J. Harbour and M. F. A. Harrison, "The influence of electron emission at the divertor target of a tokamak fusion reactor," *Journal of Nuclear Materials,* vol. 76-77, pp. 513-517, 1978/09/01/ 1978, doi: https://doi.org/10.1016/0022-3115(78)90197-6.
[226] K. Ohya, "Secondary electron emission from plasma facing materials and its impact on sheath voltage," *Nuclear Instruments and Methods in Physics Research Section B: Beam Interactions with Materials and Atoms,* vol. 153, no. 1, pp. 58-63, 1999/06/01/ 1999, doi: https://doi.org/10.1016/S0168-583X(99)00037-3.
[227] S. I. Krasheninnikov, A. Y. Pigarov, and W. Lee, "Physics of the edge plasma and first wall in fusion devices: synergistic effects," *Plasma Physics and Controlled Fusion,* vol. 57, no. 4, p. 044009, 2015/03/20 2015, doi: 10.1088/0741-3335/57/4/044009.

[228] J. P. Gunn, "Evidence for strong secondary electron emission in the tokamak scrape-off layer," *Plasma Physics and Controlled Fusion,* vol. 54, no. 8, p. 085007, 2012/06/12 2012, doi: 10.1088/0741-3335/54/8/085007.

[229] J. P. Gunn *et al.*, "Scrape-off layer power flux measurements in the Tore Supra tokamak," *Journal of Nuclear Materials,* vol. 438, pp. S184-S188, 2013/07/01/ 2013, doi: https://doi.org/10.1016/j.jnucmat.2013.01.055.

[230] G. Fubiani, H. P. L. de Esch, A. Simonin, and R. S. Hemsworth, "Modeling of secondary emission processes in the negative ion based electrostatic accelerator of the International Thermonuclear Experimental Reactor," *Physical Review Special Topics - Accelerators and Beams,* vol. 11, no. 1, p. 014202, 01/08/ 2008, doi: 10.1103/PhysRevSTAB.11.014202.

[231] V. Kvon, E. Oyarzabal, E. Zoethout, A. B. Martin-Rojo, T. W. Morgan, and F. L. Tabarés, "Secondary electron emission of tin and tin-lithium under low energy helium plasma exposure," *Nuclear Materials and Energy,* vol. 13, pp. 21-27, 2017/12/01/ 2017, doi: https://doi.org/10.1016/j.nme.2017.09.005.

[232] A. J. Donné and W. Morris, *European Research Roadmap to the realisation of fusion energy*. EUROfusion, 2018.

[233] G. L. Delzanno, G. Lapenta, and M. Rosenberg, "Attractive Potential around a Thermionically Emitting Microparticle," *Physical Review Letters,* vol. 92, no. 3, p. 035002, 01/22/ 2004, doi: 10.1103/PhysRevLett.92.035002.

[234] P. K. Shukla and A. A. Mamun, "Introduction to Dusty Plasma Physics," *Plasma Physics and Controlled Fusion,* vol. 44, no. 3, pp. 395-395, 2002/03/01 2002, doi: 10.1088/0741-3335/44/3/701.

[235] J. Pelletier, "Dusty Plasmas: Physics, Chemistry and Technological Impacts in Plasma Processing," *Plasma Physics and Controlled Fusion,* vol. 42, no. 2, pp. 227-227, 2000/02/01 2000, doi: 10.1088/0741-3335/42/2/701.

[236] J. M. Jeoung *et al.*, "Characteristics of secondary electron emission coefficient and sputtering yield for MgAl2O4/MgO protective layer in AC-plasma display panels," (in English), *Japanese Journal of Applied Physics Part 1-Regular Papers Brief Communications & Review Papers,* Article vol. 45, no. 10A, pp. 7901-7904, Oct 2006, doi: 10.1143/jjap.45.7901.

[237] H. Min Sup, L. Jae Koo, K. Hyun Chul, and K. Bong Koo, "The effective coefficient of secondary electron emission in plasma display panel," *IEEE Transactions on Plasma Science,* vol. 29, no. 5, pp. 861-863, 2001, doi: 10.1109/27.964487.

[238] T. J. Vink, A. R. Balkenende, R. G. F. A. Verbeek, H. A. M. v. Hal, and S. T. d. Zwart, "Materials with a high secondary-electron yield for use in plasma displays," *Applied Physics Letters,* vol. 80, no. 12, pp. 2216-2218, 2002, doi: 10.1063/1.1464229.

[239] H. Uchiike, K. Miura, N. Nakayama, T. Shinoda, and Y. Fukushima, "Secondary electron emission characteristics of dielectric materials in AC-operated plasma display panels," *IEEE Transactions on Electron Devices,* vol. 23, no. 11, pp. 1211-1217, 1976, doi: 10.1109/T-ED.1976.18581.

[240] N. Hershkowitz, "Sheaths: More complicated than you think," *Physics of Plasmas,* vol. 12, no. 5, p. 055502, 2005, doi: 10.1063/1.1887189.

[241] S. X. Tao, H. W. Chan, and H. van der Graaf, "Secondary Electron Emission Materials for Transmission Dynodes in Novel Photomultipliers: A Review," *Materials (Basel, Switzerland),* vol. 9, no. 12, p. 1017, 2016.

[242] S. J. Jokela *et al.*, "Secondary Electron Yield of Emissive Materials for Large-Area Micro-Channel Plate Detectors: Surface Composition and Film Thickness Dependencies," *Physics Procedia,* vol. 37, pp. 740-747, 2012/01/01/ 2012, doi: https://doi.org/10.1016/j.phpro.2012.03.718.

[243] F. Yang, J. Wang, W. Liu, X. Liu, and M. Zhou, "Y2O3–Lu2O3 co-doped molybdenum secondary emission material," *Applied Surface Science,* vol. 270, pp. 746-750, 2013/04/01/ 2013, doi: https://doi.org/10.1016/j.apsusc.2013.01.147.

[244] A. S. Gilmour, *Klystrons, Traveling Wave Tubes, Magnetrons, Crossed-field Amplifiers, and Gyrotrons*. Artech House, 2011.
[245] *Photomultiplier tubes: Basics and applications*. Hamamatsu photonics, 2017.
[246] R. Hoffmann, "Electron-Induced Electron Yields of Uncharged Insulating Materials," *All Graduate Theses and Dissertations,* 01/01 2010.
[247] C. D. Wagner, W. M. Riggs, L. E. Davis, and J. F. Moulder, *Handbook of X-ray Photoelectron Spectroscopy: A Reference Book of Standard Data for Use in X-ray Photoelectron Spectroscopy*. Perkin-Elmer, 1979.
[248] A. Einstein, "Über einen die Erzeugung und Verwandlung des Lichtes betreffenden heuristischen Gesichtspunkt," *Annalen der Physik,* vol. 322, no. 6, pp. 132-148, 1905/01/01 1905, doi: 10.1002/andp.19053220607.
[249] NobelPrize.org. "Kai M. Siegbahn – Facts." https://www.nobelprize.org/prizes/physics/1981/siegbahn/facts/ (accessed 28 November, 2020).
[250] "Mathematica." https://www.wolfram.com/mathematica/ (accessed 28 November, 2020).
[251] "Comsol." https://www.comsol.com/products (accessed 28 November, 2020).
[252] "LabView." https://www.ni.com/en-us/shop/labview.html (accessed 28 November, 2020).
[253] "Borland C++." https://www.cprogramming.com/borland.html (accessed 28 November, 2020).
[254] H. Demers *et al.*, "Three-dimensional electron microscopy simulation with the CASINO Monte Carlo software," *Scanning,* vol. 33, no. 3, pp. 135-146, 2011, doi: https://doi.org/10.1002/sca.20262.
[255] Python. "Python." https://www.python.org/ (accessed 28 November, 2020).

2 Global summary of results and discussion

In this doctoral thesis, the secondary electron emission and the charging phenomena induced by incident electron irradiation on materials were studied. A special emphasis was given to studying metal/dielectric composites and dielectric materials. These materials are especially sensitive to irradiation and its effects, as they will charge locally. The study resulted in new methods of decreasing the SEY of materials under electron irradiation and of characterizing the electron emission properties of the irradiated materials.

The more relevant results of this thesis are collected in the three published scientific articles: *Publications 1, 2 and 3*. These articles are presented below after a global summary of the results discussed in them.

As mentioned before, the focus of this thesis has been to better understand the behavior of dielectric materials under electron irradiation. On the process of studying dielectric materials, an unusual phenomena observed in composite materials was also analyzed and interpreted. These composite materials featured a surface composed of dielectric and conductor domains. Under electron irradiation, their SEY was extremely low compared to the materials they are composed of. These results were published in *Publication 1:* ***"Dynamic secondary electron emission in rough composite materials"***.

Thus, the main outcome of this study was to measure the SEY of the samples and to develop a model to explain successfully why rough conductor/dielectric composites had such a low SEY (<0.2). This work was performed combining laboratory measurements and computer simulations. In the laboratory, relevant composite materials were selected and their SEY curves determined. The strong dependence of the SEY curves on the intensity of the incident electron beam was used to develop a charging model. Simulations were performed by solving with Mathematica the equations of the proposed model to analyze and confirm such charging processes.

The experimental SEY measurements confirmed that conductor and dielectric composite materials could yield very low SEY. It was found that the SEY measured using the pulsed method differed strongly from the SEY measured using the continuous method. Also, the SEY

measurement yielded different results for different intensities of the incident electron beam. Therefore, a specific charging mechanism controlling the dynamic of the measurements was proposed. SEM images were taken to confirm the different behavior of the dielectric and conductor domains located on the surface.

Computer simulations were carried out in order to explain the observed behavior of the metal/dielectric composite samples. An electric field produced by the presence of dielectric and conductor domains was calculated using Mathematica. As a first approximation the following assumptions were performed:

i) A regular distribution of consecutive conductor and dielectric domains.
ii) The domains are triangularly shaped prisms to account for the roughness of the surface.
iii) The charge is homogeneously distributed on the surface of the dielectric domains.

With these three assumptions, the simulation can be reduced to a cell where symmetric boundary conditions can be applied. In order to have an accurate electric field in the simulation cell, the electric field as a function of the surface charge density was previously calculated using 10 cells, **Figure 2.1**.

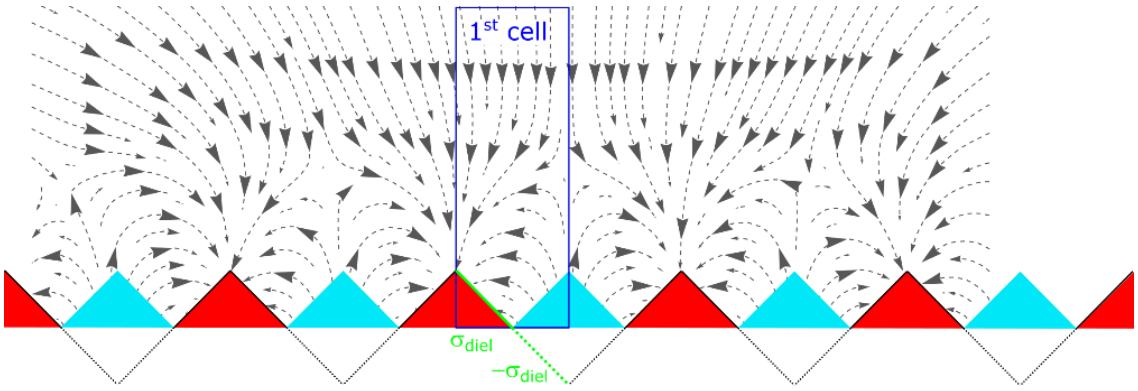

Figure 2.1. Description of the electric field produced by a metal/dielectric sample used in the computation. The simulation of the electrons is performed in the central cell with symmetric boundary conditions. The electric field is computed using a total of 10 cells to avoid spurious edge effects. Dielectric domains are shown in red and conductor domains in cyan. The electric field is produced by the surface charge density deposited on the dielectric domains and the image charge induced in the conductor domains, shown as inverted triangles below the surface. Charges and image charges are marked in green in the central cell for reference.

The trajectory of the emitted secondary electrons was computed for a range of constant surface charge densities. The coefficients of the number of emitted electrons, electrons captured in dielectric domains and electrons captured in conductor domains alongside the information of where they were generated (dielectric or conductor domains) was quantified for every selected surface charge density. After this, simulations of the SEY measurements using the continuous method on the different samples were carried out. At any point of the simulation, the surface charge density in the sample was recorded in order to use the coefficients obtained in the static simulations and the surface charge density was increased according to these coefficients.

It was found that the simulations followed the general behavior of the measurements taken in the laboratory. Therefore, it was concluded that the proposed charging mechanism controlled the observed dynamic SEY curves. These results open a new way to decreasing the SEY of surfaces by coating materials with a composite material of the kind used in the study.

Alongside the study of the behavior of composite materials under electron irradiation, pure dielectric materials were also studied. In particular, the charging curves of dielectric surfaces. Charging curves are the charge emitted by the dielectric surface under irradiation as a function of time. Studying these curves, the idea that information about the energy spectra of the emitted electrons (or EDC) was embedded in them arose. Such proposition is based on the fact that the potential barrier developed over any positively charged material will act as a retarding potential. Therefore, the emission of secondary electrons with lower energies than the potential barrier will be inhibited. As the surface potential grows, the number of emitted secondary electrons decreases. Coupling these two variables the energy spectra of materials can be obtained, **Figure 2.2**. This method is presented and tested in *Publication 2:* ***"Electron emission spectra by charging analysis"***.

In this publication, the method was applied and tested on several floating conductor samples: Cu, Ag and Au foils. As the samples were ungrounded, the charging behavior of a dielectric surface could be mimicked. Also, the EDC of conductor samples can be obtained in the laboratory using other techniques. Therefore, the results given by the proposed method were compared to the spectra acquired by conventional methods. In our case, a hemispherical electron energy analyzer (HEEA) was used. As it was shown, the spectra obtained with the proposed method closely matched the EDCs acquired with the HEEA.

The main outcome of *Publication 2* is that the proposed method uses very low total incident charge on the sample ~ 1 nC. This ensures a minimal distortion produced by charging effects

on the solid. This is especially relevant for dielectric materials, where implanted charges can be difficult to dissipate and will distort the spectra measurement. The method was applied to dielectric materials in *Publication 3*.

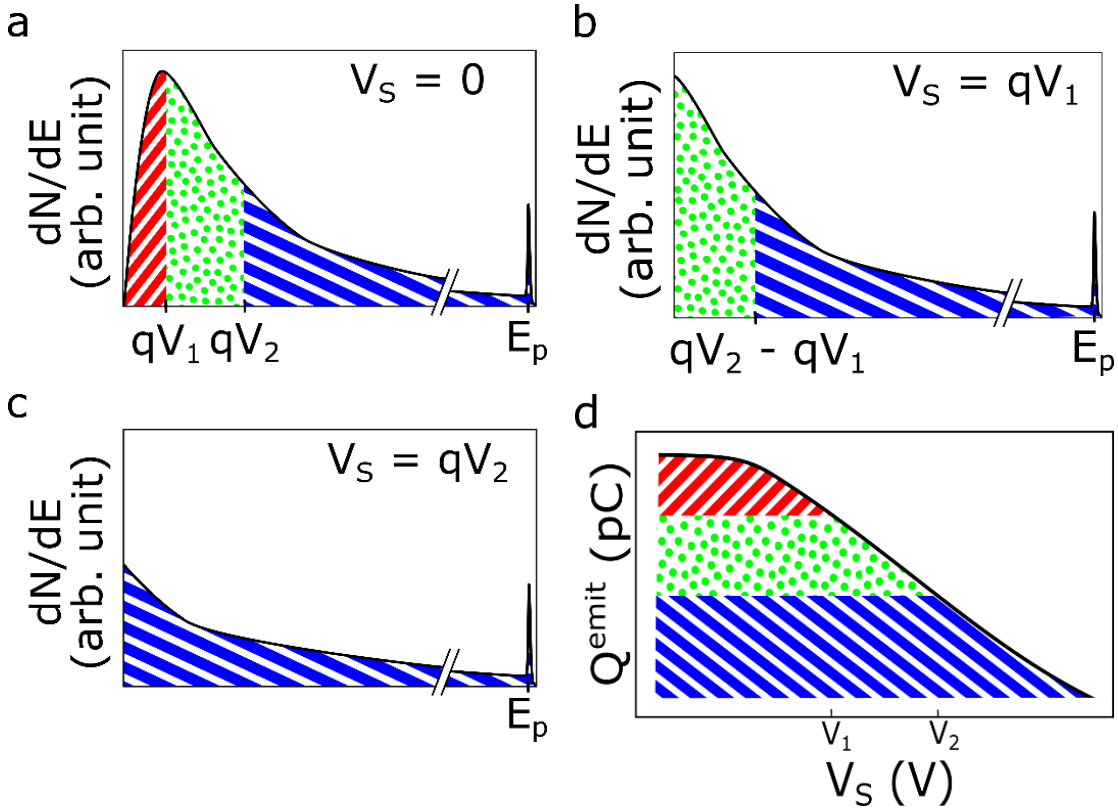

Figure 2.2. Description of the proposed method to obtain the energy spectra of secondary electrons by the analysis of the charging curves. Panels a-c, the EDC can be seen for increasing surface potentials. As the surface charges positively, SE with higher energy are trapped by the growing retarding potential. Panel d, the charging curve of the material conveys the information of the number of SE emitted at different V_S.

In *Publication 3:* ***"Energy spectra of secondary electrons in dielectric materials by charging analysis"***, the method proposed in *Publication 2* was applied to three different dielectric materials. The materials selected were Kapton, Teflon and Ultem polymers, which are extensively used in the space industry.

The main difference with the measurement on the conductors exposed in *Publication 2* was that in the case of an irradiated dielectric sample the charge does not redistribute along the surface to produce an equipotential surface. Due to this fact, two considerations had to be taken into account:

i) As the surface is not equipotential, secondary electrons emitted from different positions on the surface have to overcome different potential barriers.

ii) As the charge does not redistribute, the potential is directly over the irradiated surface and secondary electrons emitted from the edge of the irradiated surface travel with a non-zero angle respect to the normal of the potential.

To tackle this, the following was assumed: As the primary electron beam homogeneously irradiates a circular area of known radio, the charge deposited in the sample is homogeneously distributed on the irradiated area. To tackle i), computations were performed in Comsol Multiphysics to obtain the potential barriers overcame by secondary electrons emitted from different positions on the irradiated area. Likewise, to tackle ii) simulations were performed to compute the error of assuming all secondary electrons traveling through the potential at zero angle respect to its normal. This last simplification was key to reduce the complexity of the computation. A simulation of the electron trajectories in Comsol can be seen in **Figure 2.3**.

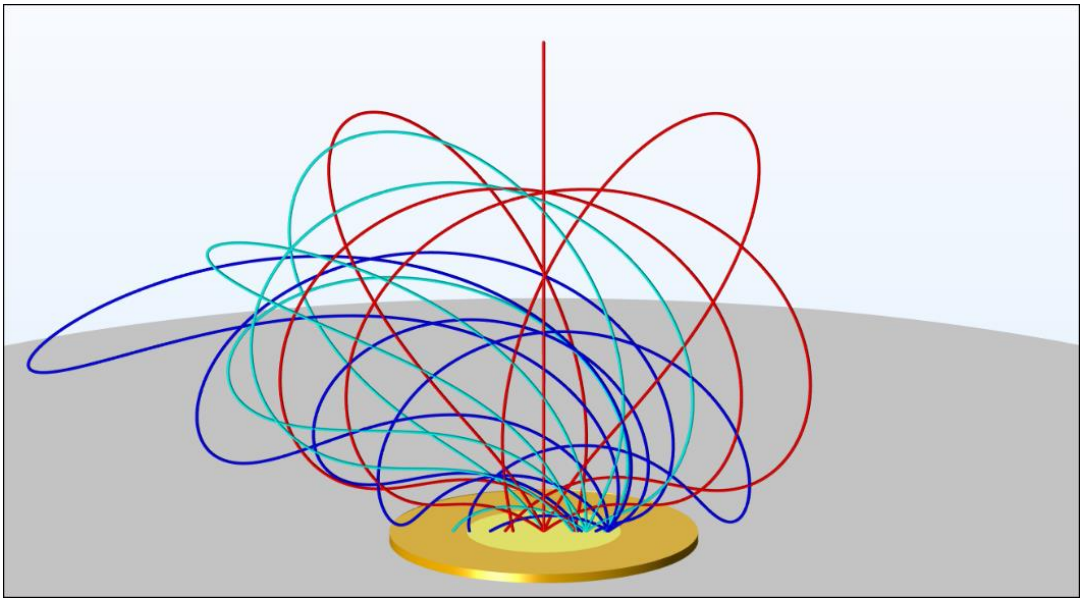

Figure 2.3. Comsol simulation of secondary electrons trapped in a positively charged sample. Electrons with 1% less energy than the potential barrier are effectively trapped by the charged material. Different colors describe the initial position of the secondary electron at emission. The bright yellow circular area in the center of the circular sample denotes the irradiated surface.

The use of the new method in dielectric samples demonstrates that the EDC of dielectric samples can be obtained by irradiating the samples with low-dose electron pulses. For each sample, only 10pC/mm^2 were used to obtain the EDC spectra of true secondary electrons. This

dose ensures a minimal distortion of the pristine condition of the material. It avoids problems that may arise if other methods with higher electron dose requirements are used.

The results developed in these scientific publications, show that the behavior of dielectric materials under electron irradiation have a great potential for discovering new applications.

It is remarkable that this charging experiments are very complex and facilities with the capabilities needed to study them are scarce. In particular, in this work, the study of composite materials has led to a new way of decreasing the SEY of surfaces exposed to incident electron irradiation. The composites can be used, for example, to coat critical surfaces in telecommunication devices to avoid Multipactor. It is equally noteworthy the new technique developed for measuring the spectra of secondary electrons emitted by dielectric surfaces. This technique uses very low doses to obtain the secondary spectra and therefore the effect on the dielectric material is negligible. Additionally, the new technique can be applied to any material (dielectric or not). This opens the way to quick and reliable secondary energy spectra measurements of dielectric materials, which are especially difficult to obtain.

3 Publications

3.1 Publication 1

SCIENTIFIC REPORTS
nature research

OPEN

Dynamic secondary electron emission in rough composite materials

Received: 2 January 2019
Accepted: 11 September 2019
Published online: 27 September 2019

Leandro Olano [1], Maria E. Dávila [1], John R. Dennison [2], Petronilo Martín-Iglesias [3] & Isabel Montero [1]

The interaction of ionizing radiation with matter is of critical importance in numerous areas of science and technology like space and vacuum technology and even medicine and biotechnology. Secondary electron emission is a consequence of electron irradiation on materials. We achieve extremely low secondary electron emission yield values smaller than 0.2, even up to incident electron energies ~1 keV, due to an undocumented synergy between neighbouring metal and dielectric domains in composite samples. To investigate this experimental discovery, we propose a simple 3D model where the dielectric and metallic domains are arranged in parallel and interleaved. The proposed surface profile has a triangular shape to model the surface roughness. We obtain a continuous equation to describe the electric field that arises between grounded conductors and charged dielectrics domains. The calculated trajectories of secondary electrons in this 3D geometry are used to predict dynamic secondary emission yield, which strongly depends on the charge accumulated in the dielectric domains. This research paves the way to design new materials of low secondary emission yield, addressing the technological problem not yet resolved to inhibit the electron avalanche in RF equipment that limit their maximum working power.

Effects of exposure to ionizing radiation is of great importance in different areas of science and technology from space and vacuum technology to even medicine and biotechnology. The effect of electron irradiation on matter is the ionization of the atoms in the material. The excited electrons travel through the material until they either lose their energy and are reabsorbed or arrive at the surface and are emitted as secondary electrons, SE.

Secondary electron Emission Yield (SEY) characterizes the number of electrons emitted by a material when an electron irradiation (primary electrons) impinges on its surface. SEY, usually denoted by , is defined as the ratio between the total number of emitted electrons and the total number of incident electrons. As well as being dependent on the material, SEY is a function of the energy (primary energy) and angle of incidence of the primary electron (PE) beam. SEY curves are generally plotted in terms of the PE energy for an electron beam normal to the surface. The shape of SEY curves, which mainly depends on the surface. The cross-over energies are defined as the energies below and above E_{max} for which 1.

SEY is a limiting factor for many vacuum-related industries and therefore has a great economic importance. For example, a high SEY is the main cause of the onset of an electron avalanche, called multipactor effect, in high-power RF devices in space [1–3], as well as the electron cloud (EC) effect in large accelerators [4–6]. It is also fundamental for other charging phenomena in satellites [7]. The multipactor effect develops when free electrons are accelerated by the electric field of an RF signal transmitted through an RF device, hitting its inner walls and consequently emitting secondary electrons. When these secondary electrons enter into resonance with the RF signal, they repeatedly hit the inner walls, increasing steadily the population of electrons if 1. The process continues as long as the signal is sustained, until an unavoidable electron avalanche occurs. The electron avalanche induce malfunctions and permanently damage RF devices. In the case of a satellite in space, it can even cause the failure of the mission.

The resonance conditions of the multipactor discharge can be inhibited by an adequate design of parameters pertaining to the RF electromagnetic field, but there always remain some critical regions where resonance conditions can only be avoided by using surfaces with low secondary electron emission. For this reason, one of the

[1]Instituto de Ciencia de Materiales de Madrid, CSIC, C/Sor Juana Inés de la Cruz 3, 28049, Madrid, Spain. [2]Utah State University Dept. of Physics, 4415 Old Main Hill, Logan, UT, 84322-4415, USA. [3]European Space Agency, ESA. Keplerlaan 1, 2201 AZ, Noordwijk, The Netherlands. Correspondence and requests for materials should be addressed to L.O. (email: l.olano@icmm.csic.es) or I.M. (email: imontero@icmm.csic.es)

maine ortsformultipactorinhibitionisbasedonreducingtheSEYofsurfacespronetomultipactordischarge [5,8–11]. Astheemissionofsecondaryelectronsisasurfaceprocess,onlytheexposedsurfaceofthematerialneedstobe modi ed.Conceptually,themostsuitablematerialsforspaceapplicationsarethosewith $_{max}$ 1.Inthiscase, thenumberofsecondaryelectronsemittedislessthanthenumberofprimaryelectronshittingthesurface,for allprimaryelectronenergies,sothattheelectronpopulationdecreasesovertimeandtheelectronavalancheis prevented.

Amorecomplexbehaviourappearswhenthematerialexposedtoelectronirradiationisdielectric.Secondary electronemissioncauseschargetobuilduponvacuum-exposeddielectricsurfaces.Additionally,high-energy PEscanpenetratethedielectricmaterial,leadingtothedevelopmentofthickerchargedregions. einteraction betweentheprimaryorsecondaryelectronswiththeelectric eldgeneratedbythedepositedchargemakesthe SEYofdielectricmaterialstendto1astheaccumulatedchargeincreases.Eventually,theinboundandoutbound charge uxescompensateeachother,stabilizingthetotaldepositedcharge.Forexample,for 1(i.e.,primary energiesbetweenE $_1$andE $_2$),someoftheemittedSEsarere-attractedbytheelectric eld. ise ectdecreasesthe numberofemittedelectrons,decreasingthee ectiveSEYandleadingto 1attheequilibriumsurfacepoten- tial.For 1(i.e.,primaryenergieslowerthanE $_1$orhigherthanE $_2$),theprimaryelectronsaresloweddownby theelectric eldduetoaccumulatedchargeuntiltheirincidentenergyyields 1oruntiltheyarerepelledfrom thesurface [12–14]. e rstcaseiscalledpositivechargingregime,whilethesecondcaseiscallednegativecharging regime. esee ectscancauseproblemswithdielectricmaterialsinvacuumexposedtoelectronirradiation. evoltagegradientscreatedcanbelarge,anddischargesbetweenchargedandgroundedcomponentscanhave seriousconsequences [15–17].

Compositematerialswithtuneablepropertiesareusedinawiderangeofindustries [18,19].SEYmeasurements forsomesmoothcompositeshavebeenreportedintheliterature [20],butnoneoftheseworksdescribeaninterac- tionbetweenmetalsanddielectricdomainstodecreasetheelectronemission.Inthisworkwepresentanundocu - mentedsynergybetweenthechargingcapacityofdielectricdomainsandtheconductivityofconductordomains, whichdecreasestheSEYofthecoatingandstabilizesSEYatlowervalues.Inessence,theelectric eldthatarises betweengroundedconductorsandchargeddielectricsdecreasestheSEY,bydrivingSEsbacktotheconducting sample.Inthisway,itispossibletoachieveextremelylowSEYsevenforhighprimaryenergies [21],whichishighly desirableforawiderangeoftechnologicalapplications.Otherstudiesintheliteraturereportlow SEYofhigh aspectratiosurfaces [9–11,22–24].Inthepresentstudywe ndevenlowerSEYvaluesformuchloweraspectratiosdue totheelectric eldbetweenthemetalanddielectricdomainsofthecoating.

Inthispaper,wedescribeexperimentalmeasurementsofSEYcurvesforthreeroughcompositematerials withverydi erentcompositionsandproperties,chosenfortheirrelevancetospaceRFdevices.Furthermore,we proposeatheoreticalmodelofthecompositesurfacethatsuccessfullydescribestheobservedexperimentalSEY behaviourandexplainshowlowSEYscanbeachievedinpracticalapplications.

SEYMeasurementProcedure

InthisworktheSEYmeasurementsofthesampleswereperformedusingtwodi erentmethods.(i)Inthecon- tinuousmethod,weirradiatethesamplecontinuouslywithanelectronbeamandincreasetheenergyofthePEs linearlywithtime. etotaldosedeliveredtothesurfacewere10nC/mm ^{2}and100nC/mm ^{2}.(ii)Inthepulse method,theprimarybeamispulsedinto170nspulses,witheachpulsedelivering~1fC/mm ^{2}.Inthiscasethe energyalsoincreaseswithtime,andasinglepulseisgeneratedforeachprimaryenergy.SEYmeasurementswere takeninanultra-highvacuum(UHV)chamberwithpressure 10 ^{9}mbar. eelectronsourceswereaKimball Physicse-guns,deliveringPEenergiesintherange0to5000eV.

Inordertoobtaintheseyofasampletheelectrongun current,Q_{eGun},ispreviouslycalibrated. en,the sampleisirradiatedandthecurrentofthesampletoground,Q_{Ground},ismeasuredbyKeithleyelectrometers(con- tinuousmethod)orafastFemtoampli erandaKeysightoscilloscope(pulsedmethod).SEYisthuscomputed asfollows

$$Q_{emit}/Q_{eGun} \quad 1 \quad Q_{Ground}/Q_{eGun} \tag{1}$$

SampleDescription

Wepreparedthreedi erenttypesofroughcompositeswithwell-di erentiatedconductoranddielectricdomains onthesurface:(i)adielectricepoxyresinmixedwithFeparticles,whichconferconductivepropertiesonthe resin(*Sample1*);(ii)zeolites(NaAlSiO $_6$-H_20)coatedwithgoldnanoparticles(*Sample2*);and(iii)amixtureof dielectricpolyimidethermosettingresinandaluminiumparticles(*Sample* 3) [21].

Sample1 wasmadefromapowderofepoxymixedwithFeparticles. emixturewasmouldedintosolidcyl- indersof30mmdiameter,thenslicedintosamples2mmthick.For*Sample2* ,zeoliteparticlesweredepositedon analuminiumsubstratethatwastotallycoveredbyadhesiveconductivegraphitetape.Goldnanoparticleswere thendepositedusingastandardsputteringmethod,resultinginpartialcoveragebyagoldlayer~2nmthick. e sameprocedurewasusedto xconductoranddielectricparticles,withasizeof1mm,in*Sample3* .

esurfacemorphologyofthesampleswasanalysedwithascanningelectronmicroscope(SEM),asshownin Fig. . eSEMisabletoqualitativelydetermineroughness,accumulatedcharge,anddi erencesincomposition. WhentheSEMisusedinbackscatteringmode,brightareasrepresentelementswithabiggeratomicnumber,Z, becausethenumberofbackscatteredelectronsincreaseswithZ. ise ectcanbeobservedintherightimageof thetoppanelofFig. 1;thebrightareasarethegold-coateddomainsof*Sample2* andthedarkareasareuncoated zeoliteregions. ecompositionwasalsoobtainedbyEnergyDispersiveX-Rayspectroscopy,EDX.WhenSEMis usedinsecondaryelectronmode,surfacemorphologyispresentedingreyscale,butbrightareascanalsobedue

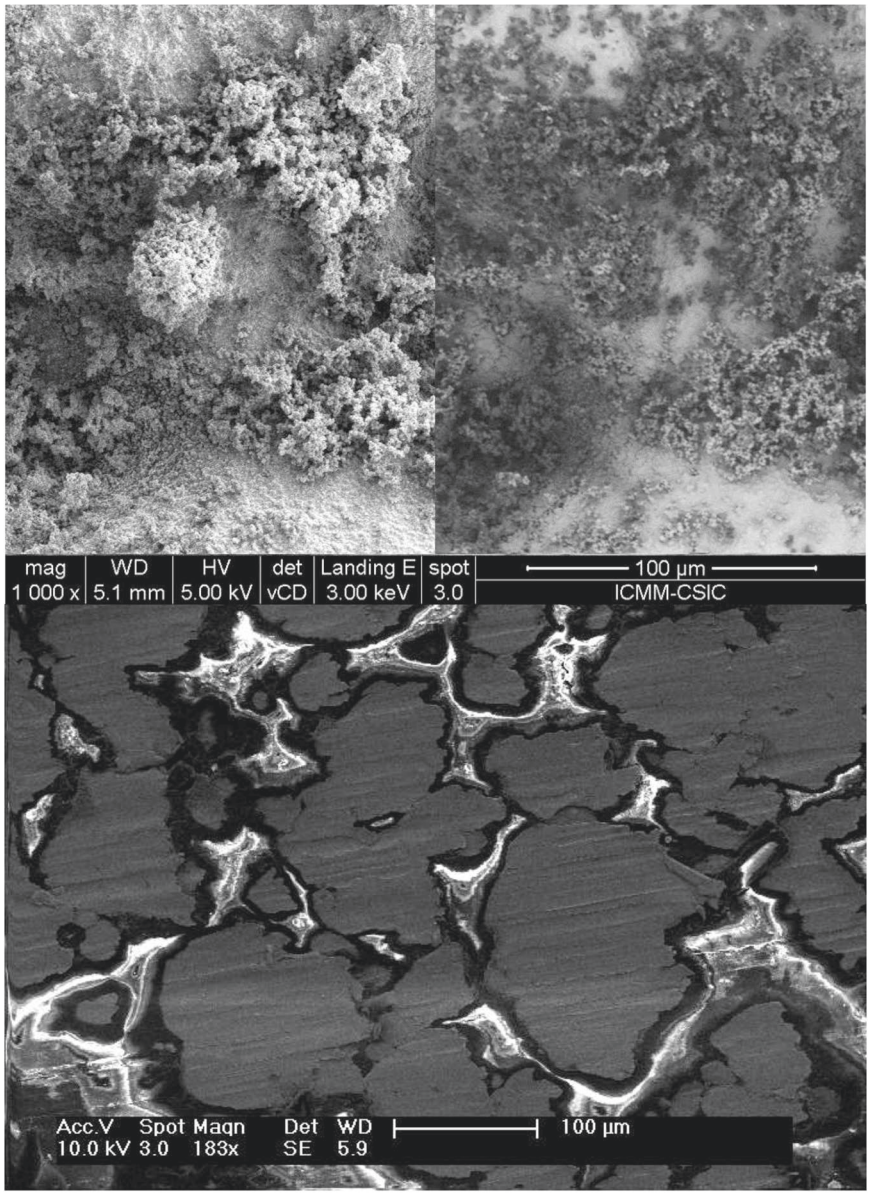

Figure1. SEMimagesofSample1andSample2.Toppanel:SEMimagesofSample2.Inbackscatteredmode (right,thebrightareasaregold-coateddomains,highZ,andthedarkareasareuncoatedzeoliteregions.In secondarymode(le),thebrightareasdenotechargingorhighregions.Bottompanel:SEMimage(secondary mode)ofSample1. ebrightareasareepoxyresinregionschargingundertheelectronirradiation,whilethe darkareasareconductingFeregions.

tochargeaccumulatinginthesample.InthebottompanelofFig. 1,chargingisthemainfactorproducingbright areas. isoperatingmodeletusdi erentiatetheconductinganddielectricdomainsinthesurfaceof*Sample1* .

SEYResults

Secondaryemissionyieldmeasurementsunderelectronbombardmentof*Samples1* , *2*and *3*,obtainedbythecontinuousandpulsedmethods,areshowninFig. 2 andTable 1. ereisanoticeabledi erenceinthevaluesofthe rst cross-overenergy,energyatwhich 1,measuredbythepulsedandcontinuousmethods.WenametheseparametersE_1andE_1^Crespectively,wheretheCstandsfor"continuous".AswecanobserveinFig. 2,E_1^C E_1forthese samples.Speci cally,for *Sample1* ,E_1^C increaseswiththedose.Itisespeciallyremarkablethat SEYvalueslower than1andcloseto0.2weremeasuredinallsamples,andevenforprimaryenergiesuptoabout1keVin*Sample3* .

Severalchargerelaxationmechanismscantakeplaceinadielectricsample,suchashoppingchargetransport, space-charge-limitedconduction,andohmicconduction [25]. edischargingprocesscanbemeasuredbydelivering enoughchargetothesampleandcontrollingtheSEYasitdischargestowardstheunchargedvalue. e resultingSEYdecaycurveiswell tedbyasingleexponentialfunctionwithatimeconstantforchargerelease, 100s.

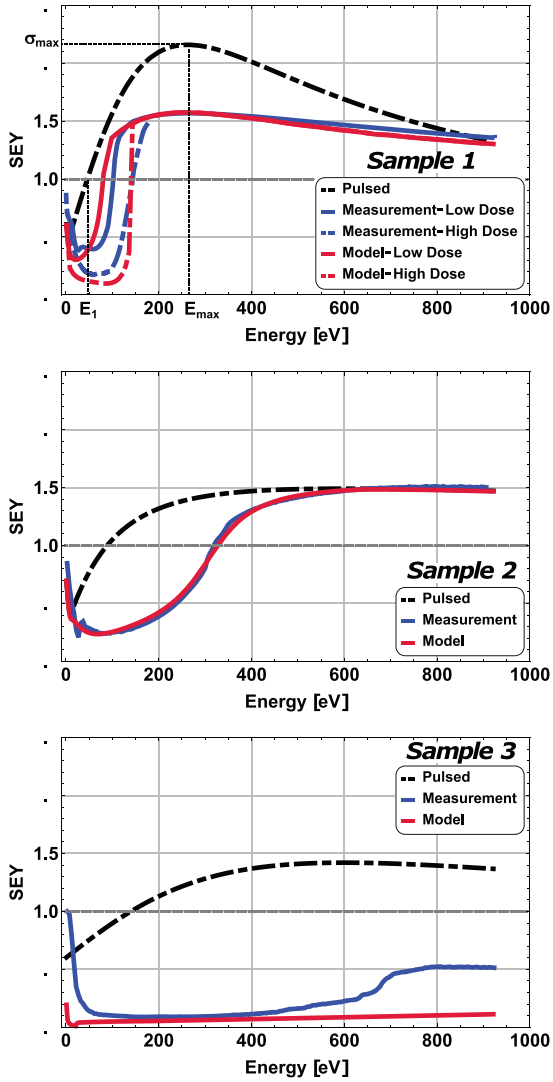

Figure 2. SEY measurements and model predictions. SEY as a function of the primary electron energy for *Samples* 1, *2*, and *3*. The measured SEY is given in blue, the SEY given by the model is in red, and the measured uncharged SEY is given in black. In the top figure the SEY parameters, E_1, E_{max} and σ_{max}, are shown.

Dynamic SEY Model

To describe the SEY behaviour of the rough metal/dielectric coatings, we present here a unique model where the conductor and dielectric domains have the shape of infinitely long triangular prisms. The dielectric and conductor domains are arranged alternatively and in parallel on the sample plane of the sample substrate. The way the coating has a triangular profile that simulates the roughness of the samples. The model allows to easily change the roughness by using different prism shapes to represent the different domains. We chose an aspect ratio of 0.5 as a simple way of representing the general quality of surface roughness, and to avoid complexity.

The electric field is computed assuming that charge only accumulates on the surfaces of the dielectric domains. The image charge method is used to account for the grounded conductor domains. For simplicity, we use a nearest-neighbour approximation, where only the single conductor domain nearest to a given dielectric domain contributes to the mirror image charge. Under these assumptions, the source distribution is approximated as a set of infinitely long, uniformly charged strips placed on the external surfaces of the dielectric domains and their corresponding image charges. $E_{Strip}(r)$ is the electric field of a horizontal infinite strip, Eq. (2), with surface charge density σ_{Diel} and unit width, with its center located at the origin of the coordinate system. Equation (3) represents the electric field, $E(r)$, obtained by adding several infinite strips, with their directions and positions specified by the rotation and translation transformations $\mathcal{R}$ and $\mathcal{T}_{r^0_{Diel/Image}}$ corresponding to the orientations and positions of dielectric and image strips, r^0_{Diel} and r^0_{Image}. Five pairs of conductor and dielectric consecutive domains were used in the computation.

	Dose(nC/mm ^{2})	E_1/E_1^C (eV)	$E_1^{model}/E_1^{C,model}$ (eV)	$_{max}$	$_{max}^{model}$	E_{max} (eV)	E_{max}^{model} (eV)
Sample1	1·10 ^{6}(pulsed)	40.3	40.3	2.16	2.16	263.5	263.5
	10	101.9	80.0	1.57	1.57	276.2	256.0
	100	144.0	141.3	1.51	1.57	276.2	259.0
Sample2	1·10 ^{6}(pulsed)	88.6	88.6	1.49	1.49	601.0	601.0
	10	318.7	322.9	1.51	1.48	871.4	666.0
Sample3	1·10 ^{6}(pulsed)	140.0	140.0	1.42	1.42	601.0	601.0
	10	(a)	(a)	0.52	0.11	803.1	918.5
	Constituents(b)	E_1 **(eV)**		$_{max}$		E_{max}**(eV)**	
Sample1	*Fe*	17.8		3.00		260.0	
	Epoxy	30.1		3.05		263.6	
Sample2	*Au*	20.4		2.50		425.0	
	Zeolite	132.0		1.70		702.8	
Sample3	*Al*	27.0		2.50		593.0	
	TMM	55.6		1.49		649.1	

Table1. Dose,E $_1$, $_{max}$andE $_{max}$parametersofthesamplesanditsconstituents. epulsedmeasurements aregiventothemodelasinputs;therefore,theparametersofthepulsedmeasurementsarethesameasthose usedinthemodel.(a) 1forallprimaryenergies.(b)SEYparametersoftheconstituentsofcompositesfor primaryelectronincidenceat45°anda erexposuretoair [26,29].

$$E_{Strip}(r) \quad \frac{Diel}{4\ _0} Log\ 1 \quad \frac{8x}{(1\quad 2x)^2 \quad 4z^2}\ ,\ 0,\ 2\ ArcCot\ \frac{2z}{1\quad 2x} \quad ArcCot\ \frac{2z}{1\quad 2x} \tag{2}$$

$$E(r) \quad _{\{r^0_{Diel},\ \}} \quad r^0_{Diel} \quad E_{Strip}(r\ ) \quad _{\left\{r^0_{Image},\ \right\}} \quad r^0_{Image} \quad E_{Strip}(r\ ) \tag{3}$$

Asthechargedstripshavein nitelength,theelectric eldisindependentofthedepthcoordinateandthe problemsimpli estotwodimensions(seeFig. 3).However,simulatingtheSEYin2Dignoresanysecondary electronsleavingthesurfacewithavelocitycomponentparalleltotheprismaxis. eelectric eldwillhavea biggerin uenceonsuchelectrons,sincetheystayclosetothesurfacelonger. us,weexpectthe2Dsimulation tounderestimatethein uenceofsurfacechargeonSEY.Toavoidedgee ectsduetousinga nitenumberof domainsinthesimulation,weapplyperiodicboundaryconditionsaroundthevalleyde nedbythecentralpairof domains. iscentralareaisdelimitedbytheverticaldashedlinesinFig. 3. e gurelengthscaleisnormalized totheprismwidth,W.Duringthesimulation,onceanoutboundSErisestoadistancewheretheelectric eldis normaltothesurface(thedashedareaatthetopofFig. 3),itsvelocityiscomparedtotheescapevelocity,calcu- latedasthevelocityatwhichtheelectronwouldescapeconsideringtheaccelerationatitsposition.Ifthisvelocity ishigher,theelectronisconsideredtohavebeenemittedbythesample.Otherwise,thecomputationcontinues untiltheSEful lstheescapeconditionorhitsadielectricorconductorsurface.Inprinciple,thelattercasecould producemoreSEs.However,suchsecond-generationortertiarySEsareunlikelyforlowincidentenergySEsand areneglectedinthemodel. isisfurtherdiscussedbelow.

Itisusefultostateexplicitlythattheelectricpotentialofthisgeometryisinvariantifthesurfacechargedensity isinverselyproportionaltothedomainsize. isrelationshipismadeexplicitinEq.(4),where $r \quad r/W$and $E \quad E \quad (4 \quad _0/ \quad _{Diel})$arethedimensionlessspatialpositionandelectric eld.

$$V \quad E \quad dr \quad \frac{W \quad _{Diel}}{4 \quad _0} \quad E \quad dr \tag{4}$$

Asthepotentialonlydependson Wand _{Diel}oncethegeometryisset,wecancomputeageneralpotentialfor thesystem. ispotentialisgraphedinFig. 4,wherewenormalizeitby $\overline{V_S}$(meanvoltagealongthedielectricsur - face).Notethattheshapeoftheexternalelectricpotentialdoesnotdependonthemagnitudeandsignof $\overline{V_S}$.Note alsothat,if $\overline{V_S}$ 0,thevaluesofVarealsonegativeandtheshapeofthenon-normalizedfunction $V(x/W,\ y/W)$is re ectedaroundthehorizontalplane($V/\overline{V_S}$ 0)comparedtothenormalizedfunctionshowninFig. 4.

Aperiodicpotentialwellfortheoutgoing SEsalwaysdevelopsclosetothesurface.For _{Diel} 0(negative chargingofthedielectric),thepotentialwellsappearovertheconductordomains,asseeninthetoppanelof Fig. 4.However,if _{Diel} 0(positivechargingofthedielectric),thepotentialwellsarelocatedoverthedielectric domains.Inbothcases,thepotentialwellsareseparatedbyadistanceof2Wandthepotentialapproacheszeroas thedistancefromthesurfaceincreases;seethebottompanelofFig. 4.A sstatedabove,thevalueoftheelectric potentialdependsonlyonWand $\overline{V_S}$.Forexample,thepotentialataverticaldistanceof10Wwillalwaysbe one-fourthof $\overline{V_S}$. isalsomeansthattheelectricpotentialatacertaindistancefromthesurfaceforaspeci c _{Diel}canbecontrolledbyadjustingthedomainsizeofthecoating.

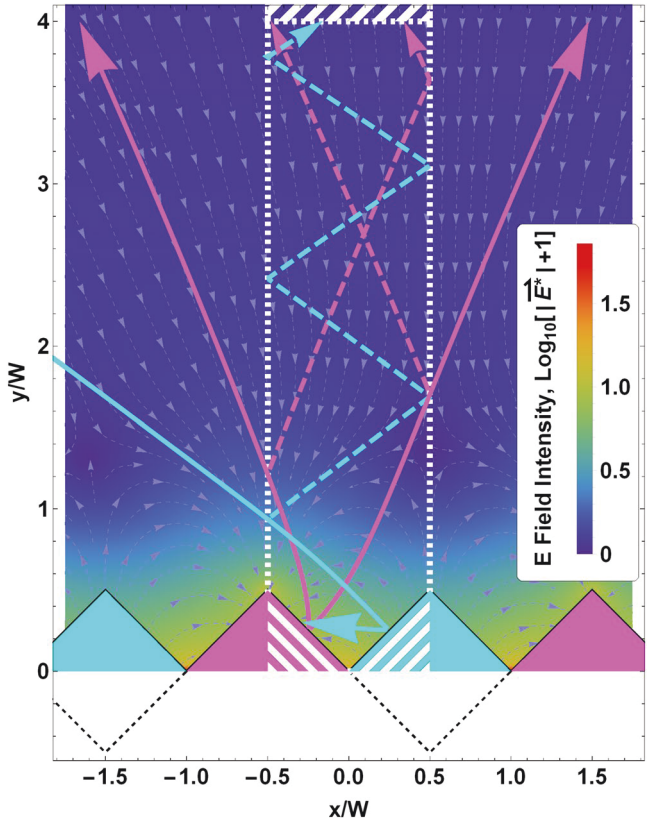

Figure3. Transversalcross-sectionofthecoatingandtheexternalelectric eld. espatialdimensionsare normalizedtotheprismwidth,W(seetext).Magenta(cyan)trianglesrepresentdielectric(conductor) domains. epositionsoftheimagechargesareshownasdashedblacklinesbelowtheconductordomains. e verticaldashedlinesrepresenttheboundariesofthecentralregionwhereboundaryconditionsareapplied,and thewhitestripedareaatthetopiswhereaSEisconsideredeligibleforemissionifitsvelocityishighenough. elightbluestreamlinesinthebackgroundrepresenttheelectric elddirectionbutnotitsintensity. e backgroundcoloursrepresentthedimensionlesselectric eld $|\overline{E}|$ 4 $_0$/ $_{Diel}$ $|\overline{E}|$inlogarithmicscale. Magenta(cyan)colouredarrowsrepresentSEtrajectoriesgeneratedindielectric(conductor)domainsas computedbythemodel.

Foranyvalueof $\overline{V_S}$,thepotentialatthesurfaceofthedielectricdomainswillpeakat $2\overline{V_S}$,duetoitsalmost lineargrowthalongthesurfaceofthedielectric. isrelationshipisshownintheinsetofthebottompanelof Fig. 4.Asstatedabove,weuseanearest-neighbourapproximationtocomputetheelectric eldgeneratedbythe dielectricandconductordomains. ee ectofthisapproximationisthattheequipotentialsurfacesdi er slightly fromtheconductorsurface,seeinsetatthebottompanelinFig. 4.

elandingenergyofelectronsincidentonthedielectricdomainsisthedi erencebetweentheenergygener - atedbythee-gunand $e\overline{V_S}$.Asweconsiderconductordomainstobegrounded,theenergyofincidentelectronson theconductordomainsissimplythee-gunenergy. etrajectoriesoftheprimaryelectronscanalsobemodi ed bythesurfacechargeofthesample.AscanbeseeninFig. 4(topandbottompanels),whenthesurfacevoltageis negative(noticethatthe $V/\overline{V_S}$ratioisalwayspositive),potentialbarriersandpotentialwellsdevelopoverthe dielectricandconductordomainsrespectively.Iftheprimaryelectronenergyislowerthantheenergybarrieron thedielectricdomains,allprimaryelectronsimpactontheconductordomains.

epositionswhereSEsaregeneratedarehomogeneouslydistributedoverthesurfaceoftheirradiated domains. eoutgoingdirectionsaregeneratedfollowingthegenerallyassumedangulardistributionofSEs(the Lambertcosinedistribution) [26]. eenergyspectrumoftheSEisgivenby

$$(E) \quad {}_0\frac{E}{(E \quad)^4}, \tag{5}$$

where $_0$isanormalizationfactorand istheworkfunction/a nityofthemetal/dielectricdomains [27].Forsim- plicity,weused 2eVand4eVforboththeconductorandthedielectricdomains,whichmeansthattheSE energydistributionpeaksat~1-5eV.

A ereachpulseofPEs,thesurfacechargedensityaccumulatedonthedielectricdomainschangesaccordingto

$$_{Diel} \quad [(\ _{Diel} \quad 1) \quad _{Diel} \quad _{DD} \quad _{Cond} \quad _{DC}] \quad _{Pulse} \tag{6}$$

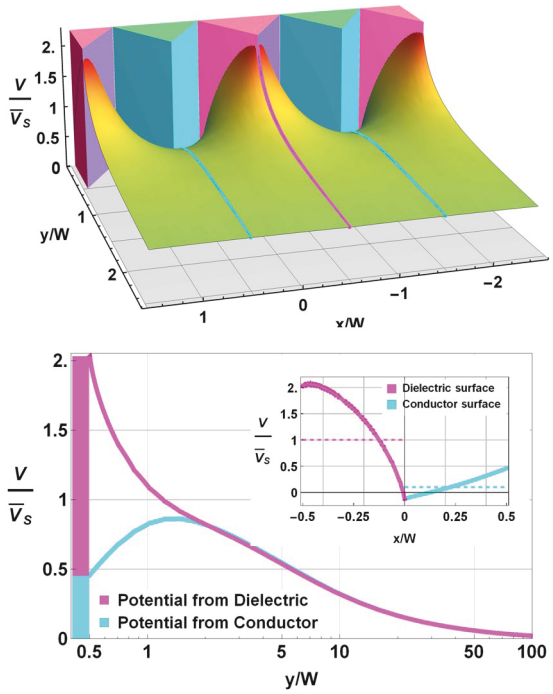

Figure4. Potentialwellproducedbyasurfacechargedensityinthemetal/dielectriccomposite. espatial dimensionsarenormalizedtotheprismwidth,W.Magenta(cyan)trianglesrepresentdielectric(conductor) domains.(Toppanel)Normalizedexternalpotential.Apotentialwellappearsovertheconductor(dielectric) domainsifthesignof $\overline{V_S}$isnegative(positive).(Bottompanel)Pro leofthenormalizedpotentialfromthetop edgeofthedielectricandconductordomains,asafunctionofthenormalizeddistanceoverthesample. e pro leshapecorrespondstothemagentaandcyancolouredgridlinesinthetoppanel.Notethatthevoltage vanishesquickly.Insetshowsthenormalizedvoltagepro lealongthesurfaceofthedomains(solidline). Dashedlinesarethemeansurfacevoltagesforthedielectricandconductorsurfaces.

Pulse isthechargedensityoftheincidentpulse,and Diel and Cond aretheunchargedsecondaryemission yieldsofthedielectricandconductordomainsforagivenprimaryenergy. DD(DC)isthefractionofsecondary electronsthathitdielectricdomainsa erbeingemittedbydielectric(conductor)domains.Similarly, CD(CC) isthefractionofSEsthathitconductordomainsa eremergingfromdielectric(conductor)domains.Finally, D (C)isthefractionofsecondaryelectronsthatescapedthesamplefromdielectric(conductor)domains. etime constant, ,wasusedtocomputethechargeremaininginthedielectricdomainsbetweenconsecutivepulses.

Thetotal SEY ofthesample iscomputed astheaverage of Dand Cmultiplied bythecorresponding uncharged Diel and Cond atagivenprimaryenergy. Dand Caredescribed inFig. 5asafunctionof $\overline{V_S}$.Wecan seethatbothparametersexhibitapeakwhenthesampleisuncharged. ereasonwhyitdoesnotrisetooneis thattheroughnessofthesampleinhibitsapartoftheSEemission.Atpositivesurfacepotentials, $\overline{V_S}$ 0,the emissionofSEsfromthecompositecoatingcanbeinhibited. isisalsothecaseforapuredielectricsurface,as shownintheinsetofFig. 5,whereSEsarecapturedwhenpositivechargeaccumulatesinthesurface.When $\overline{V_S}$ 0,SEsfromconductordomainsaree ectivelytrapped,butsomeSEsfromdielectricdomainscanstillbe emitted. isisverydi erentfromthepuredielectriccase,whereallSEsareemittedifthesurfacehasnegative charge.Forcomparison,resultsforworkfunctions(a nityinthecaseofdielectrics) 2eVand4eVareshown inFig. 5.Wecanappreciatethatthewidthofthepeaklocatedat $\overline{V_S}$ 0 Vincreaseswiththeworkfunction/a n - ity,buttheshapeofthecurveremainssimilar.

AscanbeobservedinFig. 5,thehigherthepositivesurfacevoltage(ornegativesurfacevoltage),thebetter thecoatinge ciencyatcapturingSEsemittedbydielectricandconductivedomains. us,bythetimetertiary electronscouldstarttobeimportant,moreofthemarede ectedtowardthesampleduetotheaccumulated charge. erefore,itisexpectedthattertiaryelectronsmakeanegligiblecontributiontothetotalemittedcurrent.

InFig. 6wecanobservecomputedtrajectoriesofthesecondaryelectronsemittedfromboththeconductor anddielectricdomainsfor $\overline{V_S}$ 2 $V$and $\overline{V_S}$ 2 V.Inthecaseof $\overline{V_S}$ 0,theSEsemittedfromthedielectric domains(tople panel)follownearlylineartrajectoriesclosetothetopofthesedomains.Duetothesurface roughness,someSEsfromthedielectricdomainsimpactheconductordomains.Noticeably,for $\overline{V_S}$ 0,an importantfractionofSEsfromtheconductordomains(toprightpanel)returntotheconductingsurface. isis duetotheelectric eldthatarisesinthegroovesofthecoatingbetweenneighbouringchargeddielectricand groundedconductordomains. eradiusofcurvatureoftheoutgoingSEtrajectoriesincreaseswiththeirenergy, andsodoestheirescapeprobability.

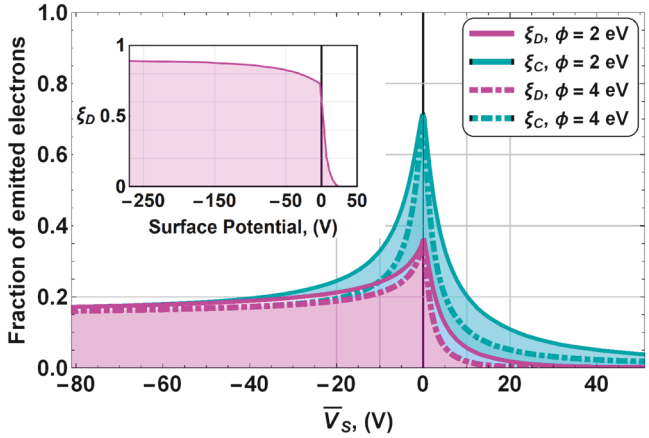

Figure5. Fractionofemittedsecondaryelectronsfromdielectricdomains $_D$(magenta)andconductive domains $_C$(cyan)asafunctionofthemeansurfacepotentialfortwodi erentworkfunctions 2,4 eV. Wecanseethatforbothdielectricandconductingdomains,thewidthofthepeakincreaseswiththework-function/a nityvalue,buttheoverallshapeofthecurveisthesame.Inset:fractionofemittedelectronsina puredielectricmaterialasafunctionofthesurfacepotential.

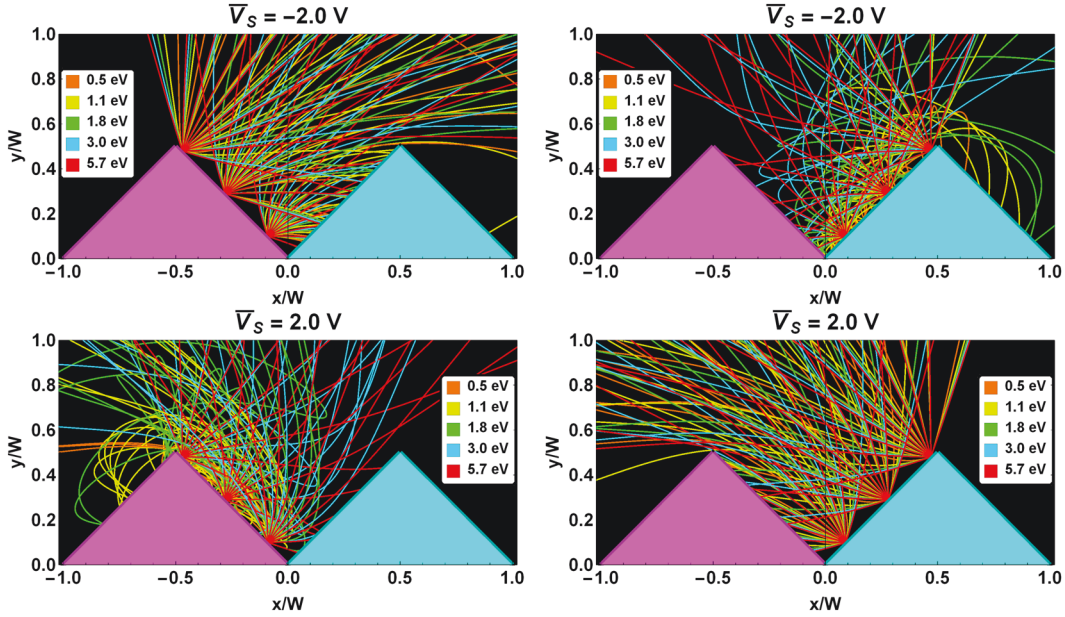

Figure6. Potentialwellandelectrontrajectories. espatialdimensionsarenormalizedtotheprismwidth,W (seetext).Magenta(cyan)trianglesrepresentdielectric(conductor)domains.Computedtrajectoriesof secondaryelectronsemittedbythedielectricandconductordomains.Forclarity,onlythreeemissionpointsare displayed. etoprowshowstrajectoriesforthenegativesurfacepotential, $\overline{V}_S$ 2 V,andthebottomrow trajectoriesforthepositivesurfacepotential, $\overline{V}_S$ 2 V. eenergiesoftheSEs(fromlessthan1eVto6eV)are givenbythetrajectorycolours.

InFig. 6,wecanalsoobservethatthetrajectoriesofSEsemittedfromthedielectricat $\overline{V}_S$ 0aresimilarto thoseemittedfromtheconductorat $\overline{V}_S$ 0,andviceversa.

Discussion

WeperformsimulationsoftheSEYcurvesfor*Samples1* , *2*and3,usingboththecontinuousandpulsedmethods. esimulationparametersaretheSEYsoftheunchargeddielectricandconductordomains $_{Diel}$and $_{Cond}$,the timeconstant ofthedischargingprocess,thesizeWofbothdielectricandmetalsdomains,theprimaryelectron ux,andthetotaldose.

AsdescribedinSEYResultssection,thedischargingprocesshasatimeconstantof~100s.Weuseadomain sizeof1mmfor*Sample3* ,and1 mfor*Sample* 1and*Sample2* . esevaluescorrespondapproximatelytothe diametersofthedielectricdomainsseeninSEMimages(Fig. 1). eincidentelectron ux forthecontinuous

methodis2nA/cm ^{2}forallthreesamples,andthetotaldoseis10nC/mm ^{2}forallsimulations.Asecondmeasurementandsimulationwithtotaldoseof100nC/mm ^{2}wasalsoperformedin*Sample* 1.The SEYvaluesoftheunchargedsamplesandconstituentsareshowninTable 1.Theresultsofthesimulationsbasedonthisgeometricmodel(red)areverysimilartotheexperimentallymeasuredSEYcurves(blue),asseeninFig. 2.

Themodelcorrectlypredictsthedropin SEYatlowprimaryenergiesinthethreesamples.AsSEY 1at primaryenergieslowerthan E_1,thedielectricdomainschargenegatively.AscanbeseeninFigs 5and 6negative surfacepotentialsreduceconsiderablytheemittedsecondaryelectronsexplainingtheaforementioneddropin theSEY.

Themodelexplainswhy E_1 ^{C}shiftedtowardshigherenergieswhenweusedahigherincidentdosein *Sample1*, Fig.2.The higherthedose,themorenegativechargebuildsupinthedielectricdomains;thisslowsdownthePEs,sotheincidentenergystaysinthe $_{\text{Diel}}$ 1domainlonger.Alargersurfacechargealsocreatesdeeper,moreeffectivepotentialwells,allowingthematerialtoachievelowerSEYvalues.Thedegreetowhich E_1 ^{C}differsfrom E_1dependsonthisinterplaybetweentheincidentflux,thetotaldose,thedifferentSEYvaluesofthedomains,andtheconductivityofthedielectricmaterial

Theextremelylowyieldsmeasuredin*Sample3*,evenathighprimaryenergies,canbealsoreproducedbyourmodel(seeFig. 2).Asdiscussedinrelationto Eq.(4),forasimilarincidentelectronfluxhighervoltagescanbeobtainedifthedomainsizeislargerasin*Sample3* (about1mm).Inthiscase, $e\overline{V_S}$ isabletofollowcloselythePEenergyuntiltheendofthemeasurement.Thus,itsdielectricdomainsarealwayschargingnegatively,sotheSEsareefficientlytrappedbypotentialwellsanddissipatedthroughtheconductordomains.

Dielectricbreakdownisnotconsideredinthismodel.Breakdownisnotexpectedforelectricfieldsweaker than10MV/m [28].Inthesimulations,themaximumvoltagesexperiencedby*Sample1* and *Sample*2are~10V;a particlesizeof~1 mgivesafieldstrengthof~10MV/m,closetobutstillbelowthetypicaldielectricbreakdownlimit. *Sample*3experiencedevenlowerelectricfields,~1MV/m,(potentialsupto1000V,particlesize~1mm).

Conclusions

WeachievedextremelylowSEYvaluesforroughmetal/dielectriccoatings, 0.2,evenforprimaryelectronenergiesnear1keV.WemeasuredSEYcurvesforthreeverydifferentcompositecoatingswithwell-differentiateddielectricandconductordomains.

Weproposedauniquemodelofsecondaryelectronemissionthatexplainsphysicalexperimentsandgivesinsightintotheextremelylow SEYvaluesobtainedintheexperimentformetal/dielectriccompositecoatings.Themodelisbasedonbothsurfaceroughnessandtheelectricfieldthatarisesbetweenchargeddielectricandgroundedconductordomainsofthecompositecoating.Thedynamic SEYbehaviourofthesecoatingsdependsonthesizeofthedomains,thetimeconstantofthedischargingprocess,theincidentelectronflux,andtheSEYoftheunchargedconstituentsofthecomposite.

OneofthemainpracticaloutcomesofthemodelisthatitexplainsthatanimportantdecreaseintheSEYofthemetal/dielectriccoatingscanbeachievedbyonlyasmallvoltagedifference(2V)betweenthedielectricandconductordomains.Thisbehaviour,alongwiththeobservedquickdecayofthegeneratedexternalpotential,pavesthewaytolow-SEYcompositecoatingswithconductingpropertiessuitableformanycriticaltechnologicalapplications.

DataAvailability

AllexperimentalSEYdatagenerateduringthisstudyisincludedinthispublishedarticle(anditsSupplementary Informationfiles).

References

1. Vaughan,J.M.Multipactor.*IEEETrans.ElectronDevices*.**35**,1172–1180,https://doi.org/10.1109/16.3387(1988).
2. Fishe,N.A.,Lau,Y.Y.,Ang,L.,Valfells,A.&Gilgenbach,R.M.Multipactordischargeonmetalsanddielectrics:Historicalreviewandrecenttheories.*Phys.Plasmas*. **5**,2120–2126,https://doi.org/10.1063/1.872883(1998).
3. Gonzalez-Iglesias,D.*etal* .AnalysisofmultipactorFbreadownawaveguidecontainingatransverselymagnetizedferrite.*IEEE Trans.ElectronDevices*. **63**,4939–4947,https://doi.org/10.1109/ted.2016.2614370(2016).
4. Dominguez,O.*etal* .Firstelectron-cloudstudiesatthelargehadroncollider.*Phys.Rev.Accel.Beams*. **16**,18,https://doi.org/10.1103/PhysRevSTAB.16.011003(2013).
5. Valizadeh,R.*etal* .Reductionofsecondaryelectronyieldfore-cloudmitigationbylaserablationsurfaceengineering.*Appl.Surf.Sci.* **404**,370–379,https://doi.org/10.1016/j.apsusc.2017.02.013(2017).
6. Cimino,R.*etal* .Canlow-energyelectronsafflecthigh-energyphysicsaccelerators?*Phys.Rev.Lett*.**93**,014801(2004).
7. Garrett,H.B. Echargingofspacecraftsurfaces.*Rev.Geophys*.**19**,577–616,https://doi.org/10.1029/RG019i004p00577(1981).
8. deLara,J. *etal* .Multipactorpredictionforon-boardspacecraftFequipmentwiththeMESTsoftwaretool. *IEEETPLASMASCI.* **34**,476–484,https://doi.org/10.1109/tps.2006.872450(2006).
9. Montero,I.*etal* .Secondaryelectronemissionunderelectronbombardmentfromgraphenenanoplatelets.*Appl.Surf.Sci.* **291**, 74–77, https://doi.org/10.1016/j.apsusc.2013.10.045(2014).
10. Nistor,V. *etal* .Multipactorsuppressionbymicro-structuredgold/silvercoatingsforspaceapplications.*Appl.Surf.Sci.* **315**,445–453, https://doi.org/10.1016/j.apsusc.2014.05.049(2014).
11. Aguilera,L. *et al* . CuO nanowires for inhibiting secondary electron emission. *J. Phys. D: Appl. Phys.* **46**,6, https://doi.org/10.1088/0022-3727/46/16/165104(2013).
12. Dennison,J.R.,Sim,A.&Thomson,C.D.Evolutionoftheelectronyieldcurvesofinsulatorsasafunctionofimpingingelectronfluenceandenergy.*IEEETPLASMASCI.* **34**,2204–2218,https://doi.org/10.1109/tps.2006.883398(2006).
13. Cazaux,J.e-Inducedsecondaryelectronemissionyieldofinsulatorsandchargingeffects.*Nucl.Instrum.MethodsPhys.Res.,Sect.B.* **244**,307–322,https://doi.org/10.1016/j.nimb.2005.10.006(2006).
14. Ashri,B.,Baouadi,R.,Renoud,R.&Yangui,B.Timedependenceofsecondaryelectronyieldandofsurfacepotentialduringchargingofamorphoussilicatarget.*J.Electrost.* **67**,695–702,https://doi.org/10.1016/j.elstat.2009.03.006(2009).
15. Dennison,J.R.Dynamicinterplaybetweenspacecraftcharging,spaceenvironmentinteractions,andevolvingmaterials.*IEEET PLASMASCI.* **43**,2933–2940,https://doi.org/10.1109/tps.2015.2434947(2015).

16. Ba□er,D.N.□ eoccurrenceofoperationalanomaliesinspacecra□andtheirrelationshiptospaceweather. *IEEETPLASMASCI.* **28**,2007–2016,https://doi.org/10.1109/27.902228(2000).
17. Balmain,□.G.Arcpropagation,emissionanddamageonspacecra□dielectrics-Areview.*J.Electrost.* **20**,95–108,https://doi.org/10.1016/0304-3886(87)90088-x(1987).
18. Al-Oqla,F.M.,Sapuan,S.M.,Anwer,T.,Jawaid,M.&Hogue,M.E.Natural□berreinforcedconductivepolymercompositesas functionalmaterials:Areview.*Synth.Met.* **206**,42–54,https://doi.org/10.1016/j.synthmet.2015.04.014(2015).
19. □a□que,I.,□ausar,A.,Anwar,Z.&Muhammad,B.Explorationofepoxyresins,hardeningsystems,andepoxy/carbonnanotube compositedesignedforhighperformancematerials:Areview.*Polym.-Plast.Technol.Eng.***55**,312–333,https://doi.org/10.1080/03602559.2015.1070874(2016).
20. Li,J. *etal* .Electron-inducedsecondaryelectronemissionpropertiesofMgO/Aucompositethin□lmpreparedbymagnetron sputtering. *J.Electron.Mater.* **46**,1466–1475,https://doi.org/10.1007/s11664-016-5178-x(2017).
21. Montero,I. *etal* .Extremely-lowsecondaryelectronemissionfrommetal/dielectricparticulatecoatings1 *4thSpacecra□Charging TechnologyConference* , *ESA/ESTEC*, https://digitalcommons.usu.edu/cgi/viewcontent.cgi?article 1030&context mp_conf .
22. Swanson,C.&□aganovich,I.D.Modelingofreducedsecondaryelectronemissionyieldfromafoamorfuzzsurface.*J.Appl.Phys.* **123**,6,https://doi.org/10.1063/1.5008261(2018).
23. Jin,C.G.,Ottaviano,A.&□aitses,Y.Secondaryelectronemissionyieldfromhighaspectratiocarbonvelvetsurfaces.*J.Appl.Phys.* **122**,5,https://doi.org/10.1063/1.4993979(2017).
24. Huerta,C.E.,Patino,M.I.&Wirz,□.E.Secondaryelectronemissionfromtexturedsurfaces.*J.Phys.D.* **51**,8,https://doi.org/10.1088/1361-6463/aab1ac(2018).
25. Chiu,F.C.Areviewonconductionmechanismsindielectric□lms. *Adv. Mater. Sci. Eng.*,18, https://doi.org/10.1155/2014/578168 (2014).
26. □eimer,L. *ImageFormationInLow-voltageScanningElectronMicroscopy*.(SPIEOpticalEngineeringPress,1993).
27. Chung,M.S.&Everhart,T.E.Simplecalculationofenergy-distributionoflow-energysecondaryelectronsemittedfrommetals underelectron-bombardment.*J.Appl.Phys.* **45**,707–709,https://doi.org/10.1063/1.1663306(1974).
28. Haynes,W.M.C□*CHandboo□OfChemistryAndPhysics*.(C□Cpress,2014).
29. Hilleret,N.,Scheuerlein,C.&Taborelli,M.□ esecondary-electronyieldofair-exposedmetalsurfaces. *Appl.Phys.A-Mater.Sci. Process.* **76**,1085–1091,https://doi.org/10.1007/s00339-002-1667-2(2003).

Acknowledgements

□ isworkwassupportedbytheSpanishMinistryofEconomy,IndustryandCompetitivenessofSpainunder "ProgramaEstataldeFomentodelaInvestigaciónCientí□cayTécnicadeExcelencia".ProjectsNoESP2015-67842-P,RTI2018-095903-B-I00andAYA2012-39832-C02-01.L.O.acknowledgesupportfromtheSpanish MinistryofEconomy,IndustryandCompetitiveness,NoBES-2013-063612.

AuthorContributions

I.M.designedandsupervisedtheproject.L.O.andI.M.performedtheexperiment,analysedthedataand developedthemodel.Allauthorsdiscussedtheresults.I.M.andL.O.dra□edthemanuscript,J.R.D.,M.E.D.and P.M.I.contributedtothewritingofthemanuscript.

AdditionalInformation

Supplementaryinformationaccompaniesthispaperat https://doi.org/10.1038/s41598-019-50353-3.

CompetingInterests :□ eauthorsdeclarenocompetinginterests.

Publisher'snote SpringerNatureremainsneutralwithregardtojurisdictionalclaimsinpublishedmapsand institutionala□ liations.

3.2 Publication 2

Results in Physics 17 (2020) 103050

Contents lists available at ScienceDirect

Results in Physics

journal homepage: www.elsevier.com/locate/rinp

Electron emission spectra by charging analysis

L. Olano, I. Montero*

Instituto de Ciencia de Materiales de Madrid, CSIC, C/Sor Juana Inés de la Cruz 3, 28049 Madrid, Spain

ARTICLE INFO

Keywords:
Electron energy spectra
Secondary electron emission
Surface charging
Electron irradiation

ABSTRACT

The energy spectra of electrons emitted due to electron irradiation are essential in relevant scientific and technological fields. While the energy spectra of conductor materials are generally acquired using hemispherical electron energy analyzers, technical difficulties remain in the acquisition of these spectra when dielectric materials are involved, as these materials charge due to electron irradiation. In this work, the energy spectra were obtained taking advantage of the unavoidable effect of charging on the energy of the secondary electrons emitted from non-conductive surfaces. A novel time-resolved low-dose irradiation method was applied for the first time to obtain the energy spectra of copper, silver, and gold samples, with the results compared with the spectra measured by the hemispherical energy analyzer. This new method could be promising for obtaining the energy spectra of dielectric materials.

Introduction

Secondary electron emission (SEE) is a phenomenon that occurs when materials are irradiated with electrons, ions, or photons of sufficient energy in a vacuum. In the case of electron bombardment, the incident (primary) electrons lose energy by inelastic scattering inside the material undergoing electrons excitations. This excitation is dominated by the decay of surface and volume plasmons produced by the incident electrons [1,2]. The kinetic energy spectrum of the emitted electrons or secondary electrons (SE) is generally known as the energy distribution curve (EDC). Fig. 1a shows the EDC of silver obtained at an incident or primary energy $E_p = 300$ eV using a hemispherical electron energy analyzer. The electrons emitted with energies lower than 50 eV (marked in red) are termed true secondary electrons (by convention) when the incident electrons have energies higher than 100 eV. Electrons emitted with energies between 50 eV and the energy of the incident electrons are called inelastically backscattered electrons (highlighted in blue), while the elastically backscattered electrons correspond to those leaving the surface with negligible energy loss (shown in green).

The EDC of the secondary electrons has important technological applications, as these curves help predict the microwave discharge in devices aboard satellites, termed as the multipactor effect [3–7]. Typically, multipactor breakdown occurs in microwave components operating under high-power conditions in vacuum. The ideal situation involves having surfaces with low-SEE to prevent multipactor discharge. This can be generally achieved by roughening the surface [8–13] but also, as recently shown, by using composite materials with conducting and isolating domains in their surfaces [14]. In the case of large particle accelerators, it is also fundamental to decrease the SEE of inner surfaces to prevent the “electron cloud” effect [15–18]. Even in Hall thrusters, which are becoming the dominant technology of electrical propulsion in space and are being further developed to decrease their size and improve their efficiency, low SEE is an important feature that determines the performance of the thruster [19–21]. Energy spectra are also relevant in high secondary electron-emission materials, which are appropriate for example, in equipment for radiation therapy, industrial processing, photon detectors, and radar systems [22–24]. These spectra are usually obtained by irradiating a sample with electrons at a fixed incident energy and using a hemispherical energy analyzer. However, this method is not well suited for measuring the EDCs of electrical insulators, as they will charge under electron bombardment. Different mathematical functions have been proposed to describe the EDCs of true SEs [25,26]. Eq. (1) was derived by a phenomenological approach [25] as follows:

$$\frac{dN(E)}{dE} = \rho_0 \frac{E}{(E+\phi)^4} \tag{1}$$

where E is the energy of the secondary electrons, ϕ is the work function of the material, and ρ_0 is a normalization factor. A Gaussian function with a logarithmic argument was proposed in [26] based on an empirical approach, as defined in Eq. (2).

* Corresponding author.
E-mail addresses: l.olano@icmm.csic.es (L. Olano), imontero@icmm.csic.es (I. Montero).

https://doi.org/10.1016/j.rinp.2020.103050
Received 16 January 2020; Received in revised form 27 February 2020; Accepted 3 March 2020
Available online 10 March 2020

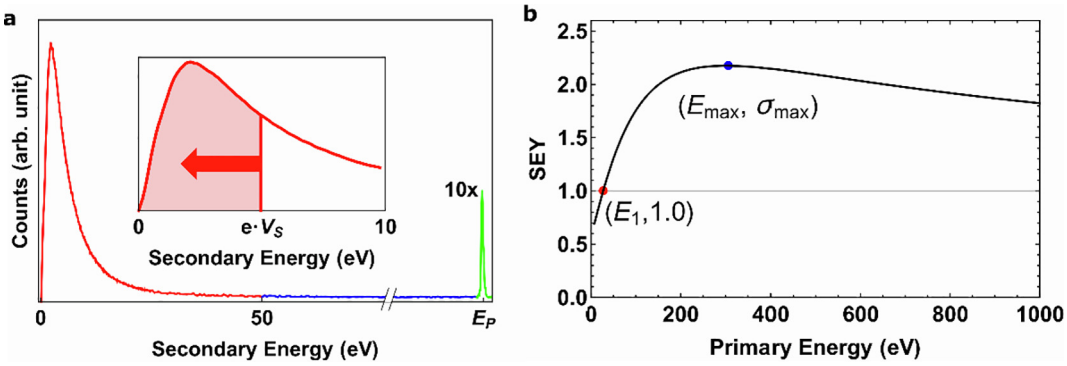

Fig. 1. Secondary electron emission (SEE) properties. Panel a, energy spectra of silver. Two peaks can be observed, with one broad peak at low energies (red) corresponding to the true secondary electrons (E < 50 eV) and a second narrow peak at the primary energy E_P (green) corresponding to the elastically backscattered electrons. These two peaks are linked by a small number of inelastically backscattered electrons (blue) that populate the intermediate energies. Inset, secondary electrons with energies lower than the surface potential, $e{\cdot}V_S$, are trapped by the electric field after being emitted and forced back to the sample. V_S acts as a retarding potential inhibiting the emission of the lowest energy electrons, reducing the number of SEs, and consequently decreasing the energy of the emitted secondary electrons. Panel b, SEY curve of silver. The main parameters used to describe the SEY curves, namely E_1 (red dot) and E_{max} and σ_{max} (blue dot) can be observed. E_1 and E_2 (not shown on the graph) delimit the primary energies at which the sample emits more radiation than it receives, thus delimiting the primary energies in the positive charging regime.

$$\frac{dN}{dE} = \rho_0 \exp\left(-\frac{1}{2\tau^2}\left(Ln\frac{E}{E_0}\right)^2\right) \quad (2)$$

Here, E represents the energy of the emitted electrons, ρ_0 is a normalization factor, and E_0 and τ are fitting parameters, with E_0 being the energy of the SEs at which the EDC peaks. This formula might be preferable as it decouples the width of the distribution and position of the maximum, yielding a better fit to the experimental results [26].

SEE is mainly characterized by the secondary emission yield (SEY, denoted by σ) parameter. SEY is defined as the ratio of the number of secondary electrons leaving the surface per primary electron. Therefore, at a specific primary energy, the SEY is proportional to the integral of the EDC divided by the total amount of incident electron radiation. The SEY depends on the properties of the irradiated material, such as the surface roughness and aging process. It also depends on the radiation properties, such as the energy of the primary electrons and incident angle. A specific material can be generally characterized with the SEY as a function of the primary energy at the normal incident angle. The main parameters of the SEY as a function of E_p, called the SEY curve, are its maximum value (σ_{max}) and energy at which it occurs (E_{max}) and the first and second crossover energies (E_1 and E_2) at which $\sigma = 1$. At these two primary energies (E_1 and E_2) the number of secondary electrons equals the number of incident electrons. Fig. 1b shows the SEY curve of Ag, with $\sigma_{max} = 2.2$, $E_{max} = 300$ eV, and $E_1 = 25$ eV.

In the case of electron irradiation of electrical insulators and ungrounded metals, two charging regimes can be discerned, namely the positive and negative charging regimes, which mainly depend on the energy of the primary electrons [27,28]. (i) Positive charging regime (SEY > 1): In this case, more secondary electrons are emitted than the primary electrons arriving at the sample. This charging regime is bounded by the first and second crossover energies, $E_1 < E_p < E_2$. In this regime, the surface of the irradiated material is positively charged and therefore, low-energy secondary electrons are deflected back to the surface once emitted, particularly those with energies lower than the potential barrier (inset in Fig. 1a). During this process, the total number of emitted electrons decreases until an equilibrium is achieved when the number of emitted secondary electrons equals the number of primary electrons. (ii) Negative charging regime (SEY < 1): In this case, the surface of a dielectric or ungrounded metal will charge negatively as there are more electrons impinging on the material than those leaving it. The primary electrons are then decelerated by the negatively charged surface. An equilibrium will be achieved once the primary electrons hit the surface with an energy at which the number of secondary electrons equals the number of incident electrons (if $E_p > E_2$) or when all incident electrons are deflected (if $E_p < E_1$).

In this work, we present a novel method to obtain the EDCs of materials through the analysis of SEE and the associated charging process under monoenergetic electron irradiation in the positive charging regime. The EDCs obtained for Cu, Ag, and Au foils (Goodfellow, UK) were compared with the spectrums acquired using a hemispherical energy analyzer. The proposed method can also be used to obtain the EDCs of electrical insulators for which other experimental methods are not suitable due to charging.

Materials and methods

SEE measurement system

The experimental measurements for the charging analysis, SEY, and secondary emission spectra were performed at the facility for space applications at the ICMM, CSIC. Three connected UHV (Ultra-High Vacuum) chambers are available to perform different electron spectroscopic techniques at a pressure $< 10^{-9}$ mbar. The electron sources were electron guns (e-guns) from Kimball Physics that can yield energies ranging from 0 to 5000 eV. The e-guns were used in either a continuous or a pulsed mode for EDC acquisition with the hemispherical energy analyzer and charging analysis, respectively. The pulsed mode delivers square pulses of 180 ns with a total incident charge per pulse, $Q^{egun} \sim 0.5$ pC at a constant energy of 300 eV. The sample was irradiated with one train of ~1000 pulses with a period of ~10 μs. An example of the recorded incident current as a function of time delivered in one pulse by the electron gun is illustrated in Fig. 2. The total charge was obtained by integrating each pulse individually. The total incident charge of the train (summation of the charge of each incident pulse, Q^{egun}) was ~500 pC, while the total accumulated charge, $Q^{acc} < 50$ pC. The duration of the charging measurement was only ~10 ms. The samples were mounted on a sample holder, and the sample current to ground was measured with an oscilloscope, which was previously amplified using a fast FEMTO amplifier as shown in Fig. 2. In these measurements, it is necessary for the sample to remain ungrounded. Therefore, the charge measured by the oscilloscope represents the image charge of the electrons deposited on the sample by one pulse, Q^{dep}. In addition, the incident charge was independently measured using a Faraday cup.

Therefore, three main parameters were considered in this work: the incident charge per pulse, Q^{egun}, deposited charge per pulse, Q^{dep}, and accumulated charge in the sample, Q^{acc}. The incident charge is

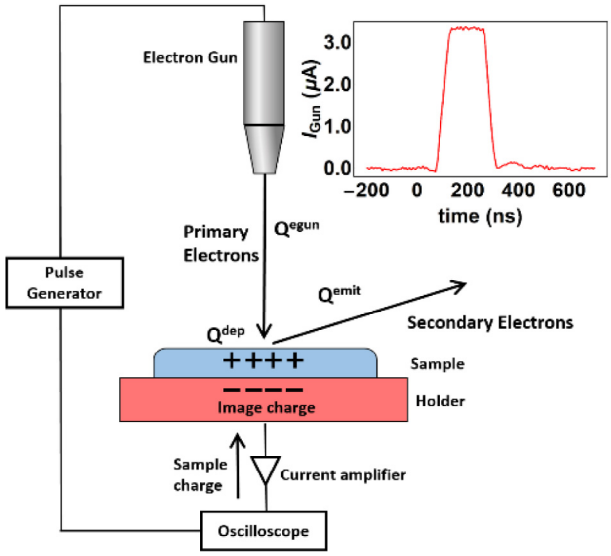

Fig. 2. Schematic of the secondary electron emission (SEE) measurement system. A pulse generator is used to reduce the total incident charge, while an amplifier and oscilloscope are used to record the fast and low sample currents. For dielectric and ungrounded metal samples, the sample current registered by the oscilloscope represents the image charge of the electrons deposited on the sample by each pulse. The arrows represent electron flows. Inset, incident electron current as a function of time delivered in one pulse by the electron gun, as registered by the oscilloscope with total delivered charge, $Q^{egun} \sim 0.5$ pC. Approximately 1000 pulses are generated and registered each time a train of pulses is measured.

constant, while the deposited charge corresponding to each pulse of a train of pulses depends on the surface potential. The accumulated charge can be calculated as the sum of the deposited charges of all previous pulses, $Q^{acc} = \sum_{pulses} Q^{dep}$.

To discharge the samples between subsequent measurements, the samples were grounded through the system, bypassing the electrical insulator after each train of incident electrons. This ensured that the potential of the sample was always initially set to 0 V, with the Fermi level used as the energy reference in the presented results.

Hemispherical energy analyzer.

A hemispherical energy analyzer was used to measure the energy spectra of the secondary electrons of materials under continuous irradiation with a monoenergetic primary electron current of 300 eV and ~10 nA. To avoid charging, the samples must be conductors and be connected to ground.

Sample preparation

The Cu, Ag, and Au samples were fixed to the sample holder with an intermediary dielectric layer using an UHV conductive double-sided adhesive carbon tape. A foil of Rexolite® [29] was used as a dielectric due to its good properties such as a negligible leakage current, relative permittivity of $\varepsilon_r = 2.53$, and volume resistivity of $\rho > 10^{16}$ Ω·cm, which results in R·C > 2000 s. The Rexolite thickness was 0.90 ± 0.05 mm and matched the area of the conductor. The sizes of the Cu, Ag, and Au samples were 2.5 ± 0.1, 2.5 ± 0.1, and 2.8 ± 0.1 cm^2, respectively, with thicknesses of 0.1 mm (Cu), 0.035 mm (Ag), and 0.0125 mm (Au). Thus, for example, for a voltage of 10 V sustained over a 10 ms measurement interval, the leakage charge of Rexolite is 0.1 fC, which is < 0.001% of the total accumulated charge on the samples. Therefore, SEE was measured as a function of the accumulated charge on the conductor sample using Rexolite as a dielectric intermediate layer.

Results and discussion

Calculations

When a material is under electron irradiation with a constant primary energy in the range of the positive charging regime, a positive voltage will develop on its surface. Thus, secondary electrons emitted with energies lower than e·V_S, where V_S is the surface potential, will be deflected back towards the surface, as shown in the inset in Fig. 1a. V_S can be interpreted as a retarding potential, which inhibits the emission of the lowest energy electrons while slowing down the rest. Consequently, the total emitted charge from a positively charged surface is smaller than that emitted in its uncharged state. This can be expressed by Eq. (3):

$$Q^{emit}(V_S) = Q_0^{emit} - \int_0^{V_S} \frac{dN}{dE} dE = \int_0^{\infty} \frac{dN}{dE} dE - \int_0^{V_S} \frac{dN}{dE} dE \quad (3)$$

where $Q^{emit}(V_S)$ is the emitted charge at the surface potential V_S, Q_0^{emit} is the emitted charge at $V_S = 0$ V, E is the kinetic energy of the secondary electrons, and $\frac{dN}{dE}$ is the number of electrons emitted as a function of their energy, i.e. the EDC. Deriving Eq. (3) with respect to V_S, the EDC can be obtained as defined in Eq. (4).

$$EDC = \frac{dN}{dE} = -\frac{1}{e} \frac{dQ^{emit}(V_S)}{dV_S} \quad (4)$$

Therefore, according to Eq. (4), the EDCs can be obtained directly from the rate of change of the emitted charge as a function of the surface voltage or retarding potential.

The emitted charge can be computed as $Q^{emit} = Q^{egun} - Q^{dep}$, as indicated in Fig. 2. As Q^{egun} (charge delivered by the electron gun) remains constant throughout the duration of the train of pulses, the derivative in Eq. (4) therefore only depends on the experimentally obtained Q^{dep}, as defined in Eq. (5).

$$\frac{dQ^{emit}(V_S)}{dV_S} = \frac{dQ^{dep}(V_S)}{dV_S} \quad (5)$$

The surface voltage of the sample, V_S, depends on the accumulated charge, which can be computed as $Q^{acc} = \sum_{pulses} Q^{dep}$. The deposited charge on the floating conductor sample distributes all over its surface to maintain an equipotential surface. This distribution depends on both the sizes of the sample and holder and their relative positions. As the relationship between the accumulated charge in a conductor and the associated surface voltage is not straightforward, a method to derive this relationship was devised. The experimental results of the measurement system were verified with the simulations performed in COMSOL Multiphysics 5.3a® [30].

Fig. 3a shows the charge deposited on the Ag sample by each electron pulse, Q^{dep} (blue line), along with the total accumulated charge, Q^{acc} (red line), as a function of the irradiation time. The charging curve $Q^{dep}(Q^{acc})$ can be subsequently obtained straightforwardly, as shown in Fig. 3b.

Relationship between Q^{acc} and V_S

The sample was charged to a known V_S^0 by irradiating the sample over a sufficient time interval (several seconds) with low primary energy electrons of 4, 8, 12, and 16 eV. As these low primary energies belong to the negative charging regime, a negative surface potential is generated in the sample up to the energy of the primary electrons (−4, −8, −12, and −16 V).

After charging the sample at each of the above-mentioned negative voltages, the samples were irradiated with a 300 eV train of pulses, and the deposited charge as a function of time was recorded. From these measurements, the charging curves, $Q^{dep}(Q^{acc})$ can be obtained, which

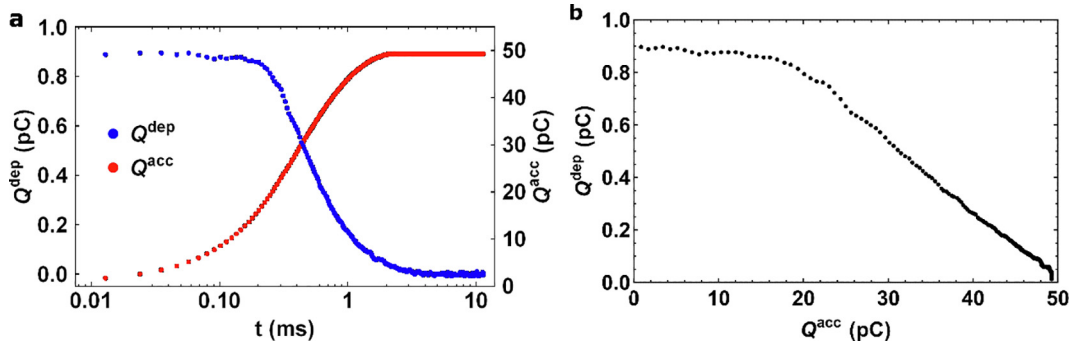

Fig. 3. Measurements performed on the Ag sample. Panel a) Deposited charge, Q^{dep}, by each pulse as a function of time (blue) and total accumulated charge in the sample, Q^{acc}, as a function of time (red). Panel b) The charging curves Q^{dep} (Q^{acc}), given by the deposited charge as a function of the accumulated charge, can be calculated straightforwardly from a).

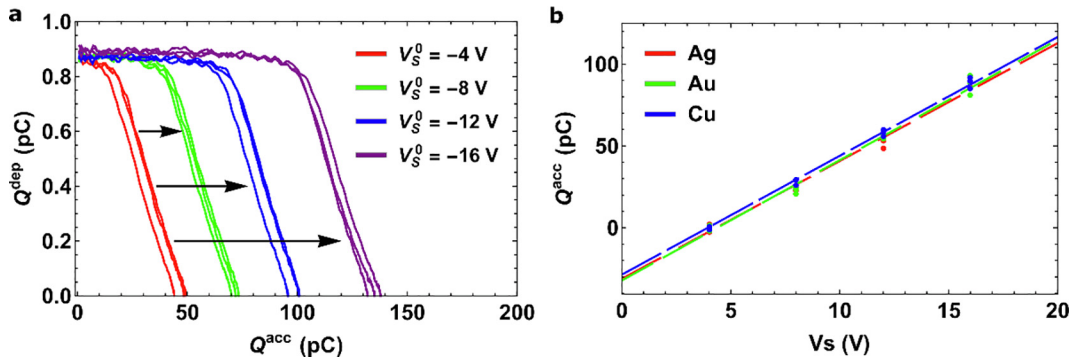

Fig. 4. Computation of the Q^{acc} (V_s) relationship. Panel a, charging curves Q^{dep} (Q^{acc}) of the Ag sample for different initial surface voltages, V_S^0. It can be seen that the curves are pushed towards higher accumulated charge values at higher initial negative surface potentials, V_S^0. Each measurement was repeated several times to verify the reproducibility. Panel b, displacement of the charging curves in terms of the accumulated charge as a function of the initial negative surface voltage (−4, −8, −12, and −16 V). A linear relationship was obtained for the Cu, Ag, and Au materials.

are shown in Fig. 4a for each of the different initial surface potentials in the Ag sample. As the SEYs of Cu, Ag, and Au were greater than 1 at E_p = 300 eV, the initial accumulated negative charge dissipated with each pulse. While the voltage in the sample remained negative, the charge deposited by each pulse remained constant. When the initial accumulated charge had completely dissipated (i.e. V_s = 0), the sample began charging positively with a decreasing Q^{dep}. Each measurement was performed several times to verify the reproducibility of the results. As shown in Fig. 4a, the charging curves, $Q^{dep}(Q^{acc})$, are displaced along the X axis (Q^{acc}) to higher accumulated charge the higher the initial negative surface potential, V_S^0. Furthermore, it can be seen in Fig. 4b that a linear relationship between the accumulated charge and surface voltage was obtained for the copper, silver, and gold samples. The slopes of the linear fits were 7.4 ± 0.1 pC/V (Cu), 7.2 ± 0.2 pC/V (Ag), and 7.4 ± 0.3 pC/V (Au). These linear relationships $Q^{acc}(V_S)$ allowed us to obtain the $Q^{dep}(V_S)$ charging curves of each sample. It should be noted that, as discussed above, only $Q^{dep}(V_S)$ is needed to obtain the EDCs defined in Eq. (4).

For comparison, the relationship between Q^{acc} and V_S was obtained in Comsol via a simulation of the measurement system with the charged ungrounded conductor samples and grounded holder and UHV chamber, as shown in Fig. 5. The specific potentials in the samples and associated charge were simulated using the electrostatic module of Comsol. The most important parameters determined in the $Q^{acc}(V_S)$ relationship included the size of the conductor samples and thickness of the intermediate insulating layer (Rexolite). Considering the measurement errors in both parameters, estimates could be provided for the simulation results. The slopes of the $Q^{acc}(V_S)$ relationship obtained in the simulation were 7.2 ± 0.6 pC/V (Cu), 7.2 ± 0.6 pC/V (Ag), and 8.0 ± 0.6 pC/V (Au), indicating a remarkably good agreement between the experimental and simulation results.

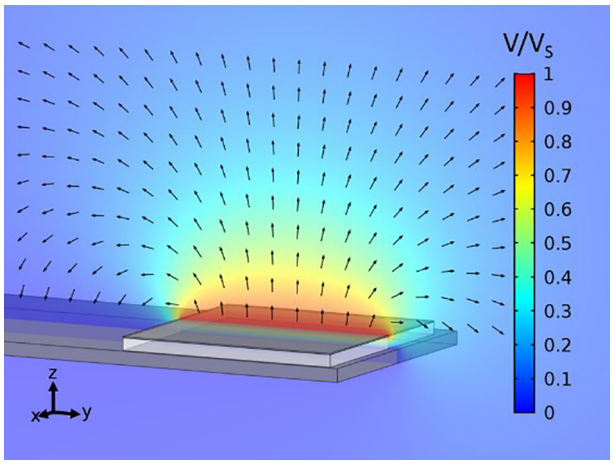

Fig. 5. Simulations in Comsol® of the potential profile due to a sample charged to a specific voltage, Vs, and grounded holder and UHV chamber. The color bar represents the magnitude of the voltage normalized to the surface voltage. The Rexolite layer between the sample and holder is shown in white. This simulation was performed to compute the relationship between V_S and the associated Q^{acc}.

Obtaining the EDCs

Eq. (4) can be used to obtain the EDC. However, as the first derivative of the experimental charging results Q^{emit} (V_S) is very sensitive to noise, the EDC can be best obtained by fitting the curve Q^{emit} (V_S) to the integral of the phenomenological and empirical EDC functions shown in Eqs. (1) and (2) [25,26]. Fig. 6 shows the EDC fits of the copper, silver,

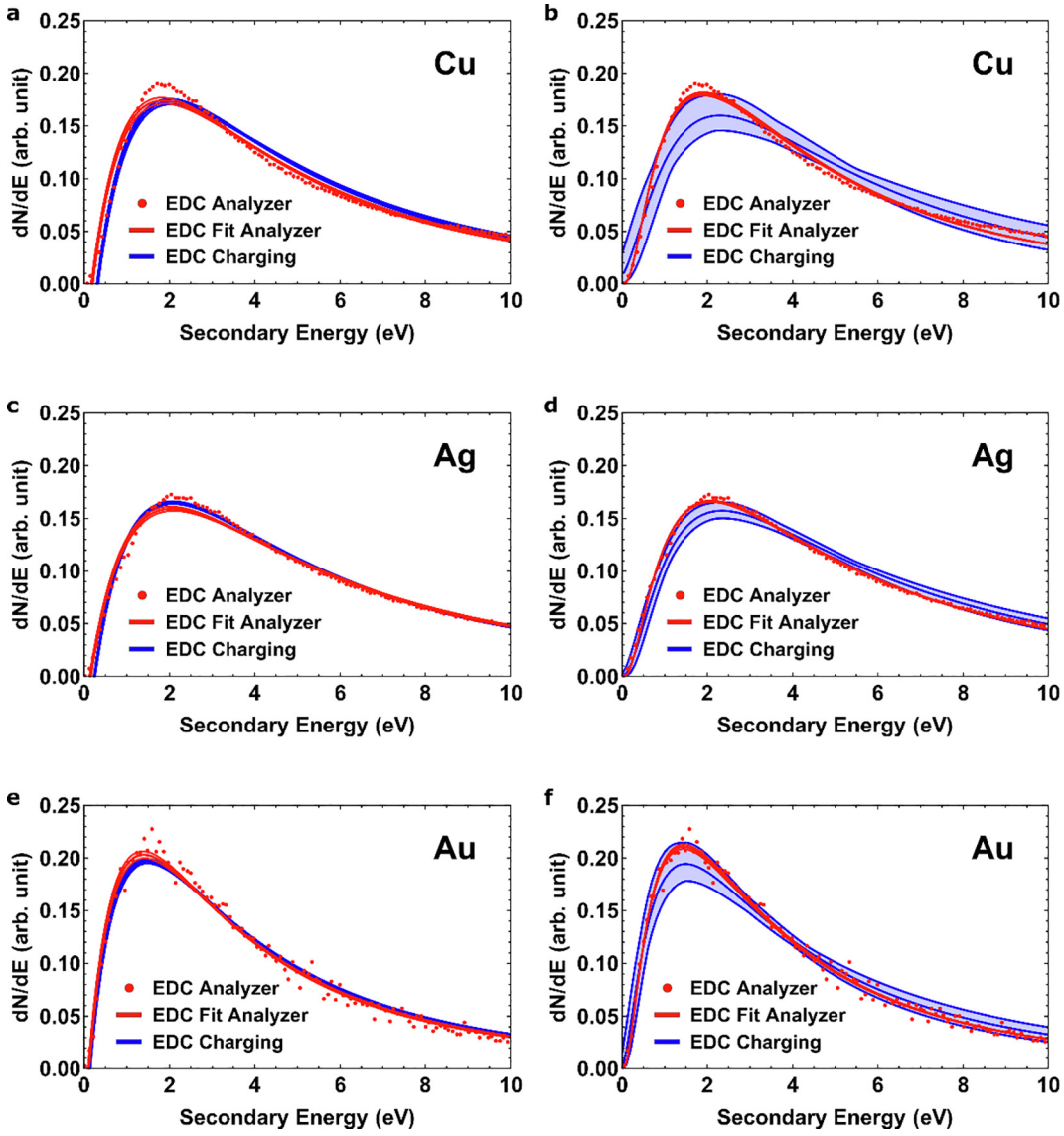

Fig. 6. EDCs of Cu (top panels), Ag (center panels), and Au (bottom panels) measured using both methods, namely the hemispherical energy analyzer (red) and charging (blue) methods. All EDCs were normalized to the range of 0–10 eV to facilitate comparison. The red dots indicate the EDC measured by the hemispherical energy analyzer; the red lines show the fits of this data to Eq. (1) (left panels) and Eq. (2) (right panels). The narrow area in light red represents the 0.95 confidence interval of the estimated values. The blue line indicates the EDC obtained by fitting the integral of Eq. (1) (left panels) and Eq. (2) (right panels) to the charging curves, $Q^{dep}(V_S)$ (see main text). The area in light blue represents the 0.95 confidence interval of each fit.

Table 1
Parameters of the fits to Eqs. (1) and (2) corresponding to the charging method and energy analyzer measurements. The errors represent the standard errors obtained from the fits to the measurements. The values of the work function reported in Ref. [32] are also provided to aid comparison.

Sample	Method	Eq. (1)		Ref. [32]	Eq. (2)	
		ϕ(eV)	E_{peak} (eV)	ϕ(eV)	$E_0 \equiv E_{peak}$ (eV)	τ
Cu	Charging	5.2 ± 0.1	2.0 ± 0.1	5.4	2.3 ± 0.2	0.87 ± 0.04
	Analyzer	5.0 ± 0.1	1.8 ± 0.1		1.9 ± 0.1	0.94 ± 0.01
Ag	Charging	5.5 ± 0.1	2.1 ± 0.1	4.4	2.3 ± 0.1	0.94 ± 0.02
	Analyzer	5.7 ± 0.1	2.0 ± 0.1		2.1 ± 0.1	0.96 ± 0.01
Au	Charging	4.1 ± 0.1	1.5 ± 0.1	4.7	1.5 ± 0.1	0.98 ± 0.03
	Analyzer	3.9 ± 0.1	1.4 ± 0.1		1.4 ± 0.1	0.97 ± 0.01

and gold samples (blue lines) to the phenomenological function, Eq. (1) (left panels), and to the empirical function, Eq. (2) (right panels). The light blue area represents the 0.95 confidence interval. The error estimates were larger for Eq. (2) than for Eq. (1) owing to having more parameters. For Eq. (1), the best estimates for the positions of the peaks, or kinetic energies at which emission was higher, were 2.0 ± 0.1 eV (Cu), 2.1 ± 0.1 eV (Ag), and 1.5 ± 0.1 eV (Au). For Eq. (2), these values corresponded to the parameter E_0, which was equal to 2.3 ± 0.2 eV (Cu), 2.3 ± 0.1 eV (Ag), and 1.5 ± 0.1 eV (Au). Furthermore, using the phenomenological derivation of Eq. (1), the

work function estimates corresponding to Cu, Ag, and Au were 5.2 ± 0.1, 5.5 ± 0.1, and 4.1 ± 0.1 eV, respectively, as presented in Table 1. The error estimation accounted for the standard deviation of the fit and standard error of the slopes $Q^{acc}(V_S)$.

In addition, Fig. 6 shows the measurements from the hemispherical energy analyzer (red dots) and best curve fits to Eq. (1) (left panels, red lines) and Eq. (2) (right panels, red lines). The considerably narrower area depicted in light red represents the 0.95 confidence interval. It can be seen that Eq. (2) fitted the measurements from the hemispherical energy analyzer slightly better than Eq. (1), mainly due to the decoupling of the width and peak position discussed above. The best peak position estimates to the energy analyzer data were 1.8 ± 0.1 eV (Cu), 2.0 ± 0.1 eV (Ag), and 1.4 ± 0.1 eV (Au) for Eq. (1), and 1.9 ± 0.1 eV (Cu), 2.1 ± 0.1 eV (Ag), and 1.4 ± 0.1 eV (Au) for Eq. (2) as indicated by the E_0 parameter. The best work function estimates given by Eq. (1) were 5.0 ± 0.1, 5.7 ± 0.1, and 3.9 ± 0.1 eV for Cu, Ag, and Au, respectively, as presented in Table 1. The error estimation considered the standard deviation of the fit.

It can be seen that the EDCs obtained via charging analysis by both Eqs. (1) and (2) were very similar to the EDC data from the hemispherical energy analyzer, being always compatible with their respective fits to the analyzer data. In addition, it can be seen that the best-fit parameters of both Eqs. (1) and (2) were compatible with each other. This makes the results independent of the EDC equation proposed to fit the charging curves; however, Eq. (2) in particular achieved a better fit to the data acquired by the hemispherical energy analyzer. To compare the EDC measurements obtained by both techniques (at a primary energy of 300 eV), the EDCs were normalized to the range of 0–10 eV. The SEY of each sample was also relevant. For the samples considered in this work, the SEYs of 2.0 ± 0.1 (Cu), 2.2 ± 0.1 (Ag), and 2.2 ± 0.1 (Au) showed reasonable agreement with other published literature [31,32].

The EDC results obtained in this work are in good agreement with other published results such as in [25,32–36]. For example, our estimation of the Au peak showed good agreement with that measured by M. S. Chung and T. E. Everhart [25] at 1.6 eV. Furthermore, Azzolini et al. [32] measured the peak of the copper spectra at ~2 eV for 250 eV incident electrons, also in agreement with our results. When comparing our estimated values of the work function with those reported in [32,35,36], we found the possible values to range from 4.3 to 5.6 eV for copper, from 3.1 to 4.9 eV for silver, and from 4.0 to 5.5 eV for gold. For example, in reference [32], the reported work function values of 5.4 eV (Cu), 4.4 eV (Ag), and 4.7 (Au) showed reasonable agreement with our predicted values. Both the work function estimates of Cu and Au were in agreement with the range of values reported in the above-mentioned literature.

The difference between our estimates of the work function values and those reported in the literature could be due to the effect of using different conditioning methods for the sample surfaces. As SEE is a surface phenomenon, different exposure to air, carbon contamination, or even variations in the roughness of the sample surfaces might have resulted in different EDCs. However, remarkably good agreement was achieved between the EDCs from the charging method and hemispherical energy analyzer for each sample. These results validate the EDC measurement method based on the charging analysis of the sample. This method can also be potentially employed to measure the EDCs of dielectric materials. However, in such materials, measurement with a hemispherical energy analyzer leads to a multitude of problems associated with the significant amount of charge required. Dissipation techniques such as flood guns and UV radiation can be employed but are not always entirely satisfactory [37] as only the most superficial charge tends to get dissipated.

It is remarkable that this method is only applicable in the positive charging regime, i.e. between the crossover energies E_1 and E_2. In this positive regime, the surface voltage of the sample will be positive and acts as a retarding potential. The final surface voltage is also important, as the higher the value of V_S, the more energetic electrons will be captured, with more information conveyed by the charging curve.

Conclusions

In this work, the energy spectra of the secondary electrons of metals and their work functions were obtained using a new method that involves registering the charging curves, $Q^{emit}(V_S)$, as the samples are irradiated by a controlled train of electron pulses. The proposed new method measured the peak positions of the EDCs at 2.2 ± 0.2, 2.2 ± 0.1, and 1.5 ± 0.1 eV corresponding to Cu, Ag, and Au, respectively. These results were compatible with the EDCs obtained by a hemispherical energy electron analyzer with peak positions of 1.9 ± 0.1 eV (Cu), 2.1 ± 0.1 eV (Ag), and 1.5 ± 0.1 eV (Au). These results were also compatible with that reported in published literature. The values of the work functions obtained with the charging method were 5.2 ± 0.1 eV (Cu), 5.5 ± 0.1 eV (Ag), and 4.1 ± 0.1 eV (Au), which displayed good agreement with those obtained with the hemispherical analyzer, i.e. 5.0 ± 0.1 eV (Cu), 5.7 ± 0.1 eV (Ag), and 3.9 ± 0.1 eV (Au).

These results establish the basis for measuring the EDCs of electrically insulating materials. For these materials, the usual hemispherical energy analyzer method is not adequate, as the sample tends to strongly charge under continuous irradiation. This results in most of the secondary electrons being not emitted or having modified energy. This even applies when charge dissipation techniques are in play, as any remnant potential will modify the acquired spectra. With the charging method, the precise control of the charging process helps discern the energies of the secondary electrons that cease to be emitted as the surface voltage increases, similar to the application of a retarding potential, to obtain the EDC.

CRediT authorship contribution statement

L. Olano: Conceptualization, Methodology, Formal analysis, Investigation, Writing - original draft, Writing - review & editing. **I. Montero:** Supervision, Conceptualization, Methodology, Investigation, Validation, Resources, Writing - original draft, Writing - review & editing.

Declaration of Competing Interest

The authors declare that they have no known competing financial interests or personal relationships that could have appeared to influence the work reported in this paper.

Acknowledgments

This work was supported by the Spanish Ministry of Science, Innovation and Universities of Spain under the “Proyectos de I+D+I Retos de la Investigación”. Project No RTI2018-095903-B-I00.

Appendix A. Supplementary data

Supplementary data to this article can be found online at https://doi.org/10.1016/j.rinp.2020.103050.

References

[1] Werner WSM, et al. Contribution of surface plasmon decay to secondary electron emission from an Al surface. Appl Phys Lett 2011;99(18):184102.
[2] Werner WSM, et al. Role of surface and bulk plasmon decay in secondary electron emission (in English). Phys Rev B 2008;78(23):4. 233403.
[3] Gonzalez-Iglesias D, et al. Analysis of multipactor RF breakdown in a waveguide containing a transversely magnetized ferrite (in English). IEEE Trans Electron Devices 2016;63(12):4939–47.
[4] de Lara J, et al. Multipactor prediction for on-board spacecraft RF equipment with

the MEST software tool (in English). IEEE Trans Plasma Sci 2006;34(2):476–84.
[5] Anza S, et al. Prediction of multipactor breakdown for multicarrier applications: the quasi-stationary method (in English). IEEE Trans Microw Theory Tech 2012;60(7):2093–105.
[6] Vaughan JRM. "MULTIPACTOR," (in English). IEEE Trans Electron Devices 1988;35(7):1172–80.
[7] Kishek RA, Lau YY, Ang LK, Valfells A, Gilgenbach RM. Multipactor discharge on metals and dielectrics: Historical review and recent theories (in English). Phys Plasmas 1998;5(5):2120–6. Proceedings Paper.
[8] Aguilera L, et al. CuO nanowires for inhibiting secondary electron emission. J Phys D Appl Phys 2013;46(16):165104.
[9] Montero I, et al. "Secondary electron emission under electron bombardment from graphene nanoplatelets," (in English). Appl Surf Sci 2014;291:74–7.
[10] I Montero, L Aguilera, U Wochner, D Raboso, Antimultipactor Coating; 2014.
[11] Valizadeh R, Malyshev OB, Wang S, Sian T, Cropper MD, Sykes N. "Reduction of secondary electron yield for E-cloud mitigation by laser ablation surface engineering," (in English). Appl Surf Sci 2017;404:370–9.
[12] Nistor V, et al. Multipactor suppression by micro-structured gold/silver coatings for space applications (in English). Appl Surf Sci 2014;315:445–53.
[13] Pivi M, King FK, Kirby RE, Raubenheimer TO, Stupakov G, Le Pimpec F. Sharp reduction of the secondary electron emission yield from grooved surfaces (in English). J Appl Phys 2008;104(10):10. 104904.
[14] Olano L, Dávila ME, Dennison JR, Martín-Iglesias P, Montero I. Dynamic secondary electron emission in rough composite materials. Sci Rep 2019;9(1):13967.
[15] Cimino R, et al. Can low-energy electrons affect high-energy physics accelerators? Phys Rev Lett 2004;93(1):014801.
[16] O Brüning et al., Electron cloud and beam scrubbing in the LHC. In: Proceedings of the 1999 particle accelerator conference, New York.
[17] Dominguez O, et al. First electron-cloud studies at the Large Hadron Collider," (in English). Phys Rev Spec Topics-Acc Beams 2013;16(1):18. 011003.
[18] Cimino R, Gonzalez LA, Larciprete R, Di Gaspare A, Iadarola G, Rumolo G. Detailed investigation of the low energy secondary electron yield of technical Cu and its relevance for the LHC. Phys Rev Spec Top Accel Beams 2015;18(5):051002.
[19] E Ahedo, VD Pablo, Effects of electron secondary emission and partial thermalization on a Hall Thruster plasma. In: 42nd AIAA/ASME/SAE/ASEE Joint Propulsion Conference & Exhibit.
[20] F Taccogna, R Schneider, S Longo, M Capitelli, Effect of surface roughness on secondary electron emission in a Hall discharge. In: 42nd AIAA/ASME/SAE/ASEE Joint Propulsion Conference & Exhibit.
[21] Garcia AO, Tang H, Ren J. Scaling model for SPT and TAL thrusters. IEEE Trans Plasma Sci 2020;48(1):86–98.
[22] Tao SX, Chan HW, Van der Graaf H. Secondary electron emission materials for transmission dynodes in novel photomultipliers: a review. Materials 2016;9(12):1017.
[23] Yang F, Wang J, Liu W, Liu X, Zhou M. Y2O3–Lu2O3 co-doped molybdenum secondary emission material. Appl Surf Sci 2013;270:746–50.
[24] Shih A, Yater J, Hor C, Abrams R. Secondary electron emission studies. Appl Surf Sci 1997;111:251–8.
[25] Chung MS, Everhart TE. Simple calculation of energy-distribution of low-energy secondary electrons emitted from metals under electron-bombardment," (in English). J Appl Phys 1974;45(2):707–9.
[26] Scholtz JJ, Dijkkamp D, Schmitz RWA. Secondary electron emission properties. Philips J Res 1996;50(3):375–89.
[27] Cazaux J. "e-Induced secondary electron emission yield of insulators and charging effects (in English). Nucl Instrum Methods Phys Res Sect B-Beam Inter Mater Atoms 2006;244(2):307–22.
[28] Dennison JR, Sim A, Thomson CD. "Evolution of the electron yield curves of insulators as a function of impinging electron fluence and energy (in English). IEEE Trans Plasma Sci 2006;34(5):2204–18. Proceedings Paper.
[29] (16 January 2019). Rexolite. Available: http://www.rexolite.com/.
[30] (16 January 2019). Comsol 5.3a. Available: https://www.comsol.com/release/5.3a.
[31] Gonzalez LA, Angelucci M, Larciprete R, Cimino R. The secondary electron yield of noble metal surfaces. AIP Adv 2017;7(11):115203.
[32] Azzolini M, et al. Secondary electron emission and yield spectra of metals from Monte Carlo simulations and experiments. J Phys: Condens Matter 2018;31(5):055901.
[33] Lawton JJ, Pulisciano A, Palmer RE. Local secondary-electron emission spectra of graphite and gold surfaces obtained using the Scanning Probe Energy Loss Spectrometer (SPELS). J Phys Condens Matter 2009;21(47):474206.
[34] Ding ZJ, Tang XD, Shimizu R. Monte Carlo study of secondary electron emission. J Appl Phys 2000;89(1):718–26.
[35] Fomenko VS, Samsonov GV. Handbook of thermionic properties: electronic work functions and Richardson constants of elements and compounds. Plenum Press Data Division [Consultants Bureau Enterprises]; 1966.
[36] Haynes WM. CRC handbook of chemistry and physics. CRC Press; 2014.
[37] R Hoffmann, Electron-induced electron yields of uncharged insulating materials, All Graduate Theses and Dissertations; 2010.

3.3 Publication 3

Results in Physics 19 (2020) 103456

Contents lists available at ScienceDirect

Results in Physics

Energy spectra of secondary electrons in dielectric materials by charging analysis

L. Olano, I. Montero *

Instituto de Ciencia de Materiales de Madrid, CSIC, Calle Sor Juana Ines de la Cruz, 3, 28049 Madrid, Spain

ARTICLE INFO

Keywords:
Electron energy spectra
Charging effects
Electron irradiation
Secondary emission
Dielectrics
Polymers

ABSTRACT

Measurement of electron energy spectra of dielectrics is a challenge due to charging issues. This article presents experimental results of electron energy spectra of dielectric materials under electron irradiation obtained by transforming the charging process into a spectroscopic tool. The technique was verified on conductive materials in a previous paper. This method is based on capturing the charging transient of the secondary electron emission current. Dielectric materials are irradiated with a single train of pulses of monoenergetic electrons. The evolution of the number of emitted electrons as a function of time is measured. The rate of this evolution coupled to the arising potential on the surface of the material conveys the energy at which the secondary electrons are emitted. The total incident dose used in this method is about 10 pC/mm^2, in contrast to the high doses required when other common methods are utilized. The use of low doses ensures a minimal distortion of the pristine state of the dielectric material by avoiding radiation damage, deep charging, defects, aging and other electron induced phenomena in the insulator. This method was applied to obtain the secondary electron energy spectra of the Kapton, Teflon, and Ultem polymers.

Introduction

Secondary electron emission occurs when materials are irradiated with electrons, ions or photons of sufficient energy. In the case of electron irradiation, the incident electrons are usually called primary electrons, PE, and the emitted electrons secondary electrons, SE. SEs are both electrons emitted from the solid through the interaction with the primary electrons (true secondary electrons) and electrons that are elastically and inelastically backscattered from the PE. The generation of the SE and the interactions that produce them inside the solids are still currently under study [1]. The electron energy spectrum or energy distribution curve (EDC) of silver irradiated with an electron beam of 300 eV can be seen in Fig. 1a. Three distinct regions of secondary electrons can be distinguished in every EDC [2,3]. Elastically backscattered electrons (green), inelastically backscattered electrons (blue) and true secondary electrons (red). True secondary electrons have low energies and appear as an intense broad peak. By convention, true secondary electrons are considered those emitted with energies 50 eV [2].

The ratio between the number of SE and PE is called Secondary Emission Yield, SEY or . SEY mainly depends on the energy of the incident electrons but it also depends on the incident angle of the electron beam, the composition and the roughness of the sample. A high SEY can be undesirable since it is the main cause of unwanted phenomena, such as Multipactor [4 9] and the electron cloud [10 13]. A low SEY is also necessary for pursuing the miniaturization and high performance of Hall Thrusters, which are becoming the dominant technology of electrical propulsion in space [14 19]. By increasing the roughness of a surface under certain conditions, the quantity of emitted SE diminishes as some of them are recaptured after emission due to the interaction of secondary electrons with the surface protrusions, decreasing the SEY [20 35]. Rough metal-dielectric composite materials can also achieve a strong SEY reduction as local electric fields between metal and dielectric domains on the surface inhibit the SE emission [36]. However, there are other relevant applications where high SEY materials are needed, such as in photomultipliers, detectors, industrial processing, radar systems and equipment for radiation therapy [37 40].

To measure the SEY of insulator and semiconductor materials as a function of the primary energy, it is necessary to avoid charging, mainly by decreasing the dose of PE. For this purpose, a single low-dose electron pulse for each primary energy can be used [36,41 43]. Fig. 1b shows the SEY curve of a Teflon sample obtained under negligible charging conditions and exposed to the environment. SEY curves can be

* Corresponding author.
E-mail addresses: l.olano@icmm.csic.es (L. Olano), imontero@icmm.csic.es (I. Montero).

https://doi.org/10.1016/j.rinp.2020.103456
Received 4 May 2020; Received in revised form 18 September 2020; Accepted 27 September 2020
Available online 1 October 2020

parameterized by $_{max}$, which is the maximum value of the SEY, E_{max}, the energy at $_{max}$, and E_1 and E_2, the first and second crossover energies, at which SEY 1. Three different regions can be defined attending to the SEY 1 value. Region (i) E_P E_1 where SEY is less than 1, therefore the number of SEs is lower than the number of PEs. Region (ii) E_1 E_P E_2 where SEY 1. In this region the maximum value of SEY, $_{max}$, is attained. Region (iii) E_P E_2 where SEY is less than 1 again. It should be noticed that it exists some materials where SEY 1 throughout the primary electron energy range and consequently E_1 and E_2 cannot be defined [22,32,44].

Under intense electron irradiation of dielectric materials, charge builds up on them due to their low electrical conductivity and a distortion of the SEY curves and energy spectra of dielectrics can be observed, see Fig. 1b. The sign of the charging will be positive or negative attending to E_P.

Region (i): negative charge will be accumulated until the incident electron radiation is repelled before reaching the surface.

Region (ii): positive charging is expected as SEY 1. A potential barrier, V_S, arises due to the net positive deposited charge. Those SEs that do not have sufficient energy to overcome this barrier will return to the dielectric, decreasing the SEY. Accordingly, the energy of the emitted SE will be decreased. The surface potential will increase due to charging until an equilibrium is obtained where SEY 1.

If E_P E_2 where E_2 is the energy at which R r, being R the penetration range of incident electrons and r the maximum escape depth of secondary electrons, a unique superficial charge layer, where SE are extracted, will be developed [45 47].
If E_P E_2 (or R r), alongside the positive top layer a deep negative charge layer will develop where PE are implanted [47,48]. Therefore, a dipolar-like electric field arises inside and outside the dielectric material that contributes to the evolution of charging and secondary electron emission. It is remarkable that, when R r, the sign of charging can reverse as the negative charge increases to slow down incident electrons up to the energy E_2 [45 47].

Region (iii): negative charge will be accumulated under sustained irradiation as SEY 1. A negative surface potential arises that is able to slow down the PE to E_2 and SEY 1 is attained.

Studies on the EDC of dielectric materials are very scarce and deal with high SEY dielectric materials or use DC methods [41,49,50]. This is due to the difficult issue of dealing with charging while acquiring energetic measurements. Some ways of dissipating accumulated charge are flood electron guns, UV radiation, low-energy ions or heating the samples to increase their conductivity. Most of these dissipation techniques achieve a zero net charge but may not dissipate all locally implanted charges. Decreasing the total incident charge facilitates its dissipation. In addition, it is important to diminish deep charging and radiation damage on the sample, which could modify its electron energy spectra. The study of the EDC of dielectric materials is needed, for example, in simulations for the Multipactor effect [4 9].

In the present paper, the charging curves of the irradiated dielectric samples are used to obtain their corresponding energy spectra by applying a recently published low-dose method [51]. This method is based on the measurement of the decrease of the emission of SEs as the SEs are trapped by the positive potential barrier that arises in the positive charging regime E_1 E_P E_2 . These charging curves can be also used to study the charge transport and the trapping phenomena in insulators [52]. The energy spectra of Kapton, Teflon and Ultem polymers were obtained in the present work.

Materials and methods

SEE measurement system

The experimental measurements were performed in the facility of secondary electron emission measurements for space applications at *Instituto de Ciencia de Materiales de Madrid - CSIC*. The experiment was carried out in an ultra-high vacuum system composed of interconnected UHV chambers at a pressure lower than 10 ^{7} Pa, where several spectroscopic techniques, such as secondary electron emission measurements (EDC, SEY), X-ray Photoemission Spectroscopy (XPS) or Auger Electron Spectroscopy (AES), are available, see Fig. 2a [53]. Kimball Physics electron guns (EGL-2022 and ELG-2) were used in this experiment, which are able to produce electrons with energies from 0 to 5000 eV. In this work, the electron gun was used in its pulsed mode.

To study the charging process and to obtain the energy spectra of the dielectrics, the samples were homogeneously irradiated by a train of 1000 squared pulses of 180 ns in length, a period of ~10 s, at an incident energy E_P 300 eV with a radius of the spot beam R_{beam} 5 mm. The incident charge (Q^{egun}) and the primary energy were constant throughout the measurement. The total incident charge density of the train of pulses on the samples was ~10 pC/mm^2 and the incident charge density per pulse ~10 fC/mm^2. An example of the recorded incident

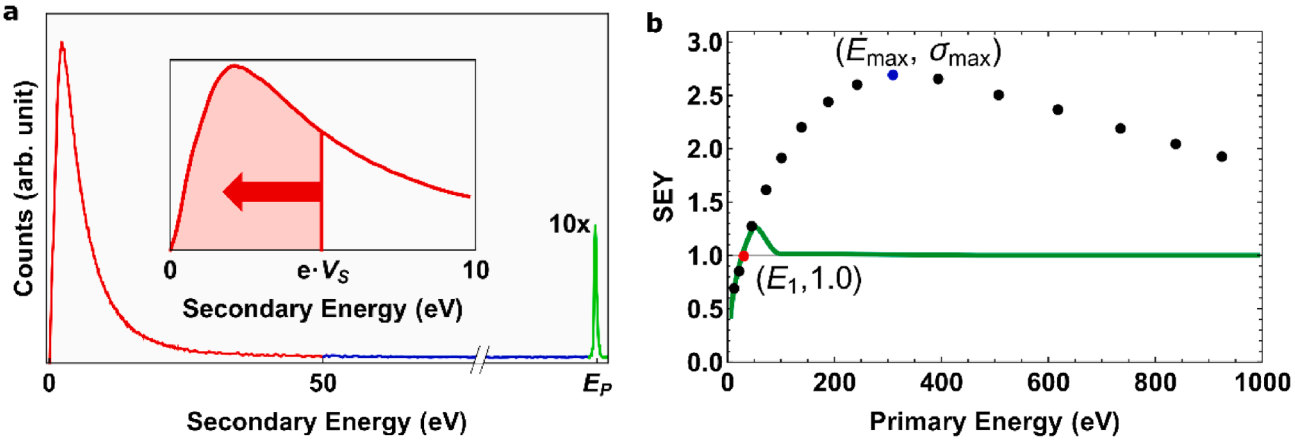

Fig. 1. Secondary electron emission properties of materials. Panel a) secondary electron spectra of silver. Three distinctive regions are shown. The peaks of true secondary electrons, backscattered electrons and inelastically backscattered electrons are drawn in red, green and blue respectively. Inset, all secondary electrons emitted with less energy than the sample surface potential, V_S, fall back to the surface (red shadowed region). Electrons emitted with more energy than V_S overcome the potential barrier but have their energy reduced consequently. Panel b) SEY curve of Teflon. The parameters of the SEY curve (E_1, 1) red dot and (E_{max}, $_{max}$) blue dot are shown. A SEY curve measured under high incident doses is shown in green. (For interpretation of the references to colour in this figure legend, the reader is referred to the web version of this article.)

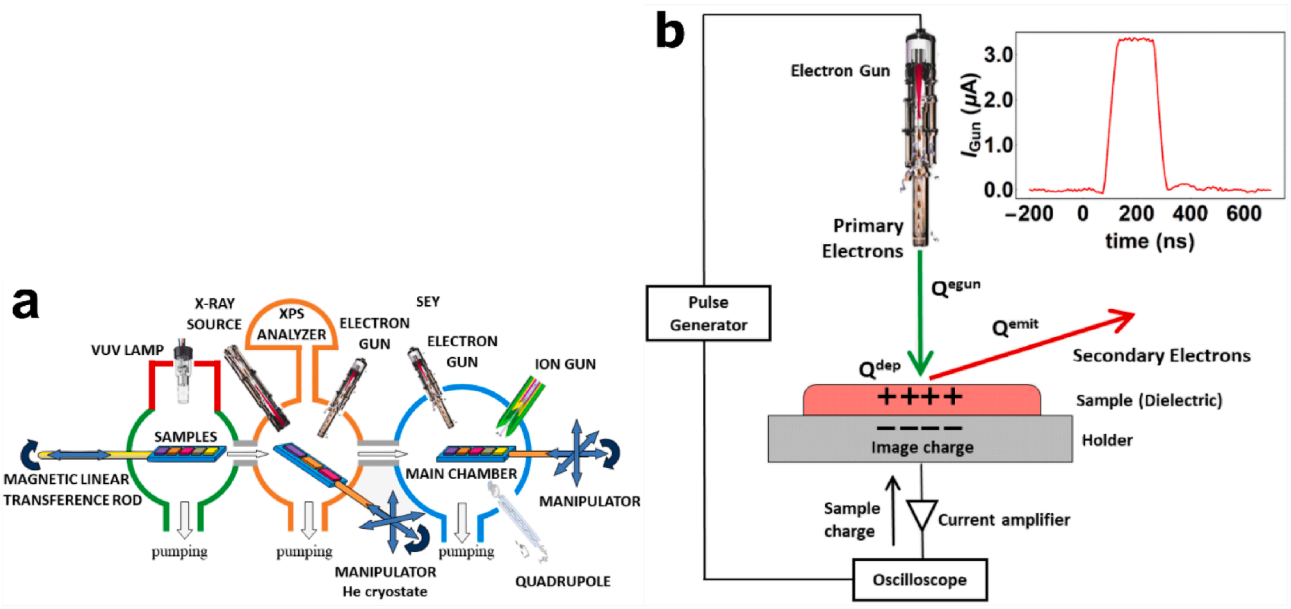

Fig. 2. Sketches of the experimental system and measurement method. Panel a) Sketch of the experimental system showing the characterization capabilities at the *Instituto de Ciencia de Materiales de Madrid - CSIC*. Panel b) Detail of the secondary electron emission measurement system. A pulse generator is used to pulse an electron gun and reduce the delivered charge, Q^{egun}. The incident charge induces a secondary electron emission charge (Q^{emit}) from the sample. The charge deposited (Q^{dep}) obeys the charge conservation laws and induces an image charge on the sample holder that is amplified by a current amplifier and registered by an oscilloscope. Arrows in the figure represent electron flows. Inset, a real signal of the deposited charge by one single pulse registered by the oscilloscope.

pulses is shown in the inset of Fig. 2b where the low noise of these signals can be observed.

The experimental set up measures the image charge induced by the charge deposited by each pulse (Q^{dep}) in the dielectric sample. This signal is amplified by a fast FEMTO amplifier and acquired in a Keysight oscilloscope as shown in Fig. 2b. The accumulated charge (Q^{acc}) is calculated as the sum of all the Q^{dep} previously deposited, Q^{acc} $_{pulses}Q^{dep}$. The total Q^{acc} ranges from ~30 pC to 300 pC, depending mainly on the thickness and the electron emission properties of the samples. Therefore, the maximum accumulated charge density on the solid was in the range of ~0.4 to 4 pC/mm^2.

After each measurement, the samples were allowed to discharge for at least 6 times the time constant of the samples, (Table 1), until the initial uncharged state was again achieved. Therefore, the vacuum level is the energy reference for all the energy measurements. To evaluate the repeatability of the measurements and improve the accuracy of the final results each sample was measured at least 5 times.

Sample preparation

Kapton HN (Polyimide, PI) [54], Teflon (Polytetrafluoroethylene, PTFE) [55] and Ultem 1000F (Polyetherimide, PEI) [56] commercial polymers were selected to obtain their electron energy spectra. These polymers have broad chemical resistance, heat resistance and high strength, which enables them to be widely used in applications as diverse as electrical, electronics, automotive, transportation, food service, healthcare, telecommunication, aerospace and affiliated industries. In particular, they are often used in thermal and electrical insulation, structural support and anti-static control on spacecraft [7,57 59]. The most relevant electrical properties of these materials for this study can be seen in Table 1. For instance, the smallest discharging time at room temperature belongs to the Ultem, which is 5 min and the longest to Teflon ~2 days. Since the total acquisition time of the measurement takes less than 10 ms, the discharge of the samples will be negligible during this time.

Samples were prepared with dimensions ~20 20 mm and mounted on the sample carrier of a XYZ micrometric manipulator using UHV conductive double-sided adhesive carbon tape. To select the constant primary energy to irradiate the samples, the SEY curves of the samples were measured. The SEY curves indicate that the E_{max} of Kapton, Teflon and Ultem are ~250 eV, ~300 eV and ~300 eV, respectively. Then, the primary energy E_P 300 eV is used in all experiments to fulfill the condition SEY 1 and E_1 E_P E_{max} E_2. In this way, a unique positive top layer of deposited charge can be considered [45 47]. Also, under this condition the signal to noise ratio is optimal because SEY is maximum. The larger the signal-to-noise ratio, the smaller the measurement error. This will decrease the statistical error associated to the measurement results. The signal-to-noise ratio at the selected primary energy is 100, see inset of Fig. 2b.

Results and discussion

Calculations

Several mathematical functions have been proposed to describe the energy spectra or energetic distribution of the true secondary electrons, [60,61]. Eq. (1) was derived by a phenomenological approach [60]:

Table 1
Dielectric properties of the Kapton, Teflon and Ultem samples [54 56,69].

	Thickness d (mm)	Resistivity (cm)	Relative permittivity $_r$	Discharging time R C (s)	d $_0$ $_r$A(V/pC)	Dielectric breakdown (MV/m)	Maximum attained surface voltages (V)
Kapton	0.07	1.4 10^{17}	3.5	43 10^3	0.03	389 430	9
Teflon	0.07	10^{18}	2.1	186 10^3	0.05	87 173	7
Ultem	0.90	10^{15}	2.9	257	0.45	437 565	15

(1)

where is the work function of the material, E the energy of the emitted electrons and $_0$ a normalization factor. The work function might be replaced straightforwardly by the electron affinity, as in insulator materials, the electron affinity is the parameter that gives the energy separation between the lowest possible state for any excited electron in the solid and the vacuum level. Other approach is to empirically decouple the position of the maximum and the width of the distribution using a Gaussian function with a logarithmic argument [61], Eq. (2):

(2)

where E is the energy of the true secondary electrons, $_0$ a normalization factor, E_0 the position of the peak, and a fitting parameter. In this work, Eqs. (1) and (2) are used to fit the experimentally obtained energy spectra.

The method used in this work to obtain the electron energy spectra of dielectric materials under electron irradiation is based on the fact that a positively charged surface will emit less electrons than the same uncharged surface, i.e. the surface potential acts as a retarding potential, inset Fig. 1a. As the surface potential (V_S) grows during electron irradiation, less electrons will be emitted attending to their energy (E_{SE}) and angle of emission respect to the surface normal ( ). Eq. (3) shows Q^{emit} V_S as a function of the energetic and angular distribution $\frac{dN\ E}{dE}$ of SE.

(3)

where Q_0^{emit} is the emitted charge at V_S 0 V, is the angle between the SE direction and the electric field generated by charging, $f(\ ,\ )$ a function relating to , E the energy of the secondary electrons and e the electron charge. It can be seen elsewhere [62] that the condition of SE emission is:

. . (4)

The potential produced by a homogeneously charged dielectric sample was studied using COMSOL Multiphysics [63], Fig. 3a. The AC/DC module of COMSOL uses the finite element method to solve the Maxwell equations and obtain the 3D potential for given boundary conditions. Fig. 3b shows the normalized surface potential profiles (V_S/V_S^C) along the normalized radial coordinate (r/R_{beam}) being V_S^C the value of the surface potential at the center of the irradiated area, r the radial coordinate and R_{beam} the radius of the irradiated area. The results indicate that the surface potential profile is independent on the size of the sample and only depends on the R_{beam}/d ratio, where d is the thickness of the sample. It can be seen that the surface potential always reaches its maximum at the center of the sample, V_S^C, and falls to half that value at the boundary of the irradiated area. For the same irradiated area, the rate at which the surface potential decays depend on the thickness of the sample. For the thinner samples, the potential is almost constant along the surface. As the charge is homogeneously distributed on the surface of the thin sample, the potential is approximately constant along the surface; there is a broad plateau centered at the maximum

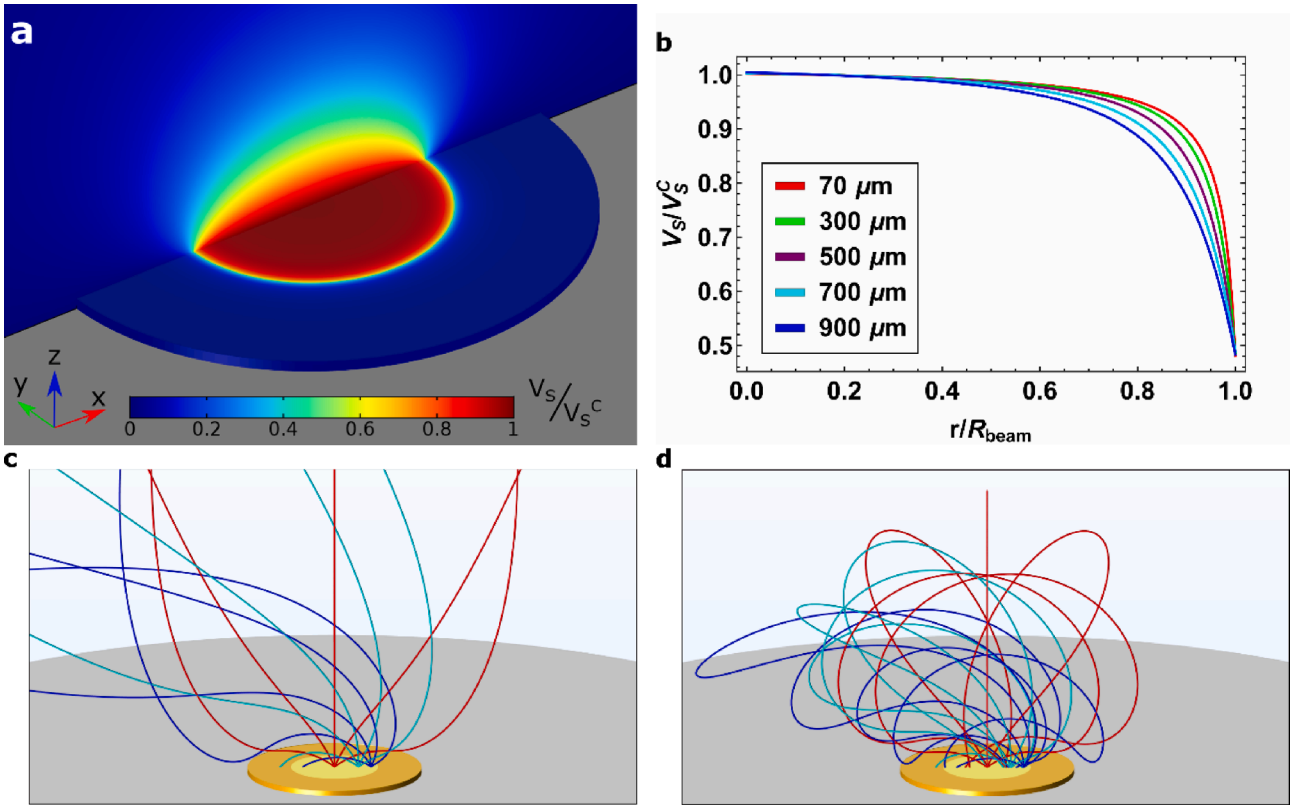

Fig. 3. Description of the charging of a dielectric sample. The thicknesses of the samples are 70 m (Ultem, Kapton) and 900 m (Teflon). Panel a) simulation in COMSOL of the 3D potential of a dielectric sample of thickness 300 m, radius 1 cm and a homogenous irradiation area of radius R_{beam} 5 mm. The potential is normalized to the maximum surface potential (potential at the center of the sample, V_S^C). Panel b) normalized surface potential profile of samples with different thickness in the range 70 900 m. Panel c) Secondary electron trajectories with 1% more energy than the potential barrier. Dielectric sample is depicted in yellow with the irradiated area drawn brighter. The gray plane is the plane where the dielectric sample rests. Trajectories are colored attending to their initial distance respect to the center of the sample. Panel d) Secondary electron trajectories with 1% less energy than the potential barrier.

value which only falls at the edge of the irradiated area. The equipotential surfaces out of the sample are shaped as a flattened semi-sphere or lentil-shaped as can also be seen in Fig. 3a.

Secondary electrons leaving the surface from the center of the irradiated area will always ascend the potential barrier with an angle 0 as the potential is approximately semispherical. Therefore, following Eq. (4), all SE that are emitted from the center, or close to the center, overcome the potential barrier, independently of their angle of emission if their energy is over the potential barrier. On the other hand, is maximized for secondary electrons emitted from the edge of the irradiated area with a trajectory towards the center of the sample. To evaluate the influence of on the electron trapping, secondary electron trajectories have been computed in Comsol with 1% energy over and below the energy barrier. The result is that ~90% of the electrons with 1% more energy than the potential barrier are emitted and 100% of the SE with 1% less energy are trapped. An example of these simulations is shown in Fig. 3c-d, where SE trajectories are displayed. As the relation between and is not straightforward due to the complex geometry of this potential, the approximation 0 for all SE is done. Therefore, an error of 10% is assumed in these calculations because, accordingly to the COMSOL simulations, 10% of electrons are trapped when we consider them as emitted with the 0 approximation. Furthermore, the simulations were performed assuming a cosine distribution for the SE angular distribution. However, for low incident energies the distribution of SE can be sharper [64] and therefore more SE can overcome the potential barrier and the committed error when considering 0 would decrease. Eq. (5) shows the expression of Q^{emit} V_S after the 0 approximation.

— — — (5)

Deriving Eq. (5) the EDC can be obtained, Equation (6).

— – ——— (6)

As the emitted charge is $Q^{emit}(V_s)$ Q^{egun} $Q^{dep}(V_s)$ and Q^{egun} remains constant in the experiment, the derivative in Eq. (6) will only depend on Q^{dep}, which is the variable that is measured, Fig. 2b. Therefore, obtaining Q^{dep} as a function of V_S is all that is needed to obtain the energy spectra (EDC) of the sample.

Relationship between Q^{acc} and V_S

In our previous publication [51], the energy spectra were obtained on conductive samples. There, a method was developed to obtain the relationship between the surface potential and the accumulated charge, $V_S(Q^{acc})$. When a metallic sample is not electrically grounded, the accumulated charge is redistributed throughout its entire surface, producing an equipotential surface, see [51]. However, in the case of dielectric materials, the charge will not redistribute. Since the irradiated area is finite, the surface will not be equipotential as the charge is localized. As the surface of a thin sample is almost equipotential, see Fig. 3b, it can be considered that in the limit d/R_{beam} 0, then V_S V_S^C cte and is described by the parallel plate capacitor equation, Eq. (7).

—— —— (7)

where Q^{acc} is the charge accumulated on the irradiated surface, C the capacitance, d the thickness of the dielectric in the capacitor, *A* the plate area, $_r$ the relative permittivity of the dielectric and $_0$ the vacuum permittivity, see Table 1. Eq. (7) was used to calculate the surface potential values at the center of the sample (V_S^C) where A is the irradiated area and d the thickness of the sample. Fig. 4a shows a comparison of V_S^C obtained by the Eq. (7) and by the COMSOL simulation (V_{sim}). The deviation between these two values is less than ~4% for the sample dimensions used in this study. Thus, Eq. (7) was used as a simple method to estimate the maximum value of the surface potential, V_S^C, under the assumption of a unique charge layer and a flat sample.

As seen in Fig. 3b, the surface of the irradiated insulator is not equipotential. In this situation, secondary electrons emitted from different positions of the irradiated area will have to overcome different potential barriers. Such potential barrier will be closer to V_S^C the closer the position of emission is to the center of the irradiated area. Since the profile of the surface potential is known, Fig. 3b, the radial distribution of electrons that cease being emitted at any V_S^C can be computed. Fig. 4b shows this radial distribution as a function of E_{SE}/eV_S^C, being E_{SE} the energy of the SEs. The radial distributions in Fig. 4b are normalized to their area. As we can observe, the shape of the curves is similar, all distributions exhibit a peak at E_{SE}/eV_S^C 1. As the thickness of the sample increases, the intensity of the peak decreases and the full width at half maximum increases. It was confirmed that considering the potential profile was necessary to calculate the energy spectrum in the case of the Ultem (with a ratio d/R_{beam} 0.18). However, in the case of Kapton and Teflon (with a ratio d/R_{beam} 0.014) the spectra can be obtained using just Eq. (7).

Obtaining the energy spectra

Fig. 5a shows the evolution of both Q^{dep} (the deposited charge by each pulse) and Q^{acc} (the accumulated charge in the surface) as a

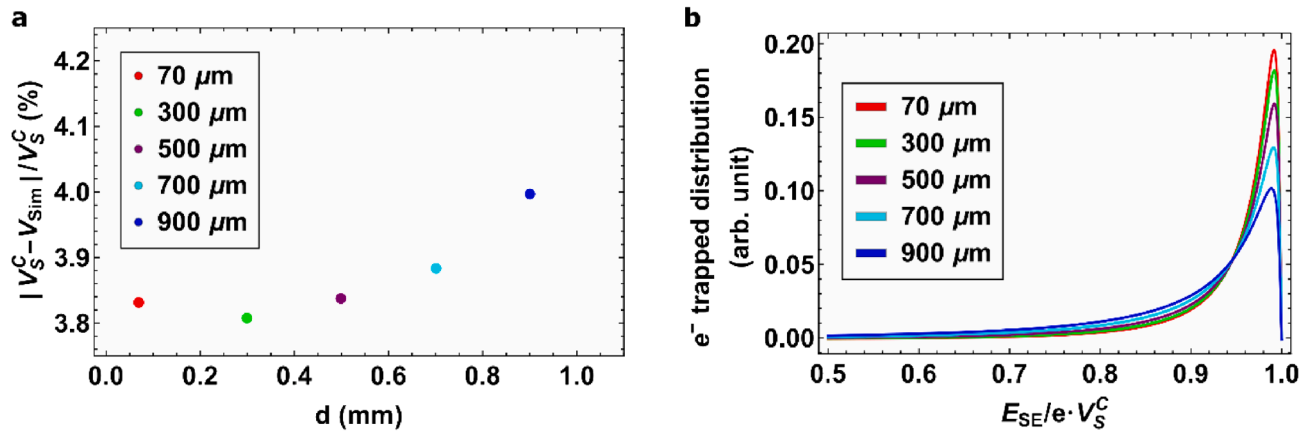

Fig. 4. Charging of a dielectric sample. The thicknesses of the samples are 70 m (Ultem, Kapton) and 900 m (Teflon). Panel a) divergence on the surface potential on the center of the sample given by the parallel plate Eq. (7) (V_S^C) respect to the COMSOL simulations (V_{sim}) as a function of the thickness of the sample (d). Panel b) energy of the electrons (E_{SE}) that cease being emitted at V_S^C. The curves shown are normalized to the area.

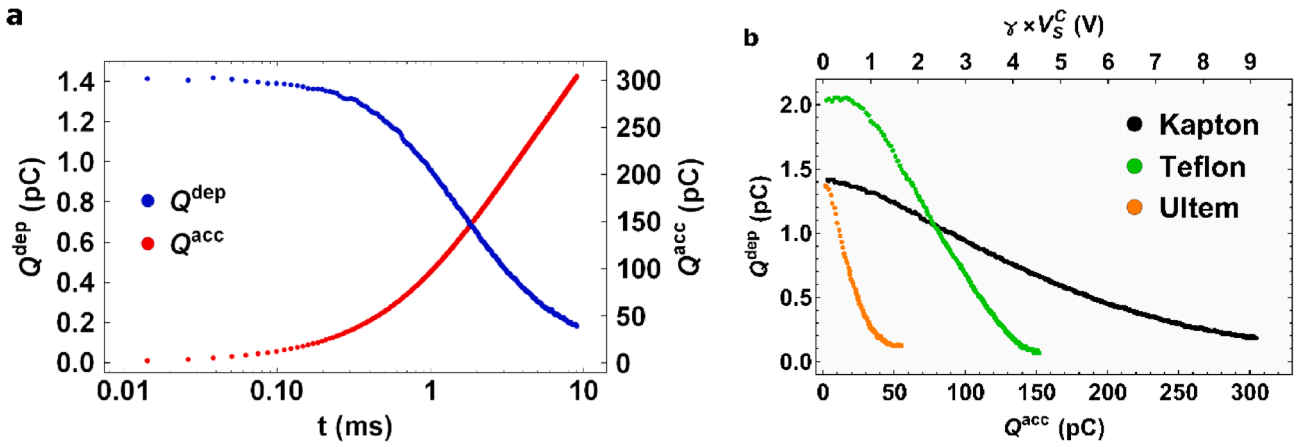

Fig. 5. Measurements performed on the Kapton, Teflon and Ultem samples. Panel a) deposited charge (Q^{dep}) by each pulse (blue) and total accumulated charge on the sample (Q^{acc}, red), as a function of time. Panel b) charging curves $Q^{dep}(Q^{acc})$ for Kapton, Teflon and Ultem obtained from combining the corresponding data of each sample, as shown in panel a). $Q^{dep}(V_S^C)$ is shown for Kapton, Teflon and Ultem calculated by Eq. (7). For visual purposes a unique V_S^C axis is shown at the top of the figure with the proportionality constant , being equal to 1, 1.67 and 15.5, for Kapton, Teflon and Ultem, respectively. (For interpretation of the references to colour in this figure legend, the reader is referred to the web version of this article.)

function of time for Kapton. In Fig. 5b the charging curves $Q^{dep}(Q^{acc})$ of Kapton, Teflon and Ultem are shown. The charging curves were obtained from combining $Q^{dep}(t)$ and $Q^{acc}(t)$ data shown in Fig. 5a. Then, V_S^C can be calculated with the Q^{acc} values using Eq. (7), also shown in Fig. 5b. Finally, the energy spectra of the dielectrics are computed using Eq. (6), that is, $dQ^{dep}(V_S^C)/dV_S^C$ and taking into account the radial distribution of the energies of the electrons captured at a specific V_S^C, shown in Fig. 4b.

The energy spectra of true secondary electrons of Kapton, Teflon and Ultem along with the best fit curves to Eq. (1) (left panels) and Eq. (2) (right panels) are displayed in Fig. 6. The value of the affinity given by Eq. (1) for Kapton, Teflon and Ultem are shown in Table 2. These results can be compared to the affinity values available in the literature obtained by first-principles calculations using Density Functional Theory. The reported affinity for Teflon is 3.75 eV and for Kapton is in the range of 1.4 to 4.1 eV [65 68].

The values of the peak position, E_{peak}, or the most likely energy at which SEs are emitted, given by the fit to Eqs. (1) and (2) for Kapton, Teflon and Ultem are shown in Table 2. Both models, Eqs. (1) and (2), gave a very similar goodness of fit for the data of Kapton. In the case of the energy spectra of Teflon and Ultem, the low-energy region of the spectra is also satisfactorily fitted by the two Eqs. (1) and (2). For higher energies than E_{peak}, Eq. (2) fits better than Eq. (1) as happened also in our previous measurements on conductive samples [51]. It can be seen that E_{peak} of the Teflon spectra is also best estimated by Eq. (2). The error estimation accounts for the standard deviation of the fits as well as the error committed by the approximation 0.

The proportionality constant in Eq. (7), i.e. 1 d $_0$ $_r A$, controls the sparseness of the experimental data. In Table 1 we can observe that it ranges from 0.03 to 0.45 V/pC, meaning that for each picocoulomb that is deposited on the surface of the sample, the potential barrier increases that many volts. Therefore, the ideal situation is maintaining this parameter as low as possible to facilitate the measurement of the energy spectra in small step increments of V_S. This can be done by reducing the total incident dose, decreasing the thickness of the sample or increasing the irradiated area.

In Fig. 6, we can also observe that the most energetic true SEs are emitted from Ultem. According to the results of the best fit of Eq. (2) to the energy spectra, 50% of them have less than 8.7 eV, 90% less than 25.4 eV and the most probable emission energy at 4.3 eV. Teflon have 50% of SEs with less than 3.2 eV, 90% with less than 6.9 eV and the most probable energy at 2.3 eV. Finally, Kapton has 50% of SEs with less energy than 5.4 eV, 90% with less than 18.9 eV and the most probable energy of emission at 1.9 eV. See Table 3.

A major strength of this experimental method to measure electron energy spectra resides in the low dose of incident radiation that is needed for its measurement. The thicker the sample, the less charge is needed to obtain the spectra, see Eq. (7) where V_S^C is directly proportional to the thickness of the sample. In contrast, under the same incident radiation the best resolution in energy is obtained for thin samples. The small dose coupled with the fact that a complete measurement is obtained without intermediate charge dissipation steps makes it a robust method. The average electric field inside the dielectric will depend on the total accumulated charge and the thickness of the sample. Since the SE energy spectra of Kapton, Teflon and Ultem samples are obtained with a total deposited charge of 300 pC, 140 pC and 34 pC, the corresponding V_S are 9 V, 7 V and 16 V, then the average electric field inside the dielectrics are 0.1 MV/m, 0.1 MV/m and 0.02 MV/m, respectively. This electric field is extremely low to produce the dielectric breakdown as the dielectric strength for these materials is ~400 MV/m (Kapton), ~100 MV/m (Teflon) and ~500 MV/m (Ultem) [69], see Table 1.

Conclusions

The electron energy spectra of Kapton, Teflon and Ultem polymers under electron irradiation were obtained by making use of the surface potential arising in the sample as a retarding field. The measurement of the charging curve $Q^{dep}(V_S)$ of an initially uncharged dielectric material conveys the energy spectra of true secondary electrons. It was found that the peak position of the distributions is 1.9 0.1 eV for Kapton, 2.3 0.1 eV for Teflon and 4.3 0.2 eV for Ultem. In general, the empirical Eq. (2) fits the energy spectrum better than the phenomenological Eq. (1), but the difference was mostly seen at energies well above the peak of the distribution. Nevertheless, it is remarkable that Eq. (1) with only 1 parameter and physical meaning for it was able to fit the data remarkably well. This method also avoids problems that can arise due to the required higher electron doses in other spectroscopic techniques, such as radiation damage, deep charging, defects, aging and other electron induced phenomena. The low dose used in this work, 10 pC/mm^2, produces a minimal distortion of the original state of the material leading to a clean measurement of the energy spectra of secondary electrons.

CRediT authorship contribution statement

L. Olano: Conceptualization, Methodology, Investigation, Formal

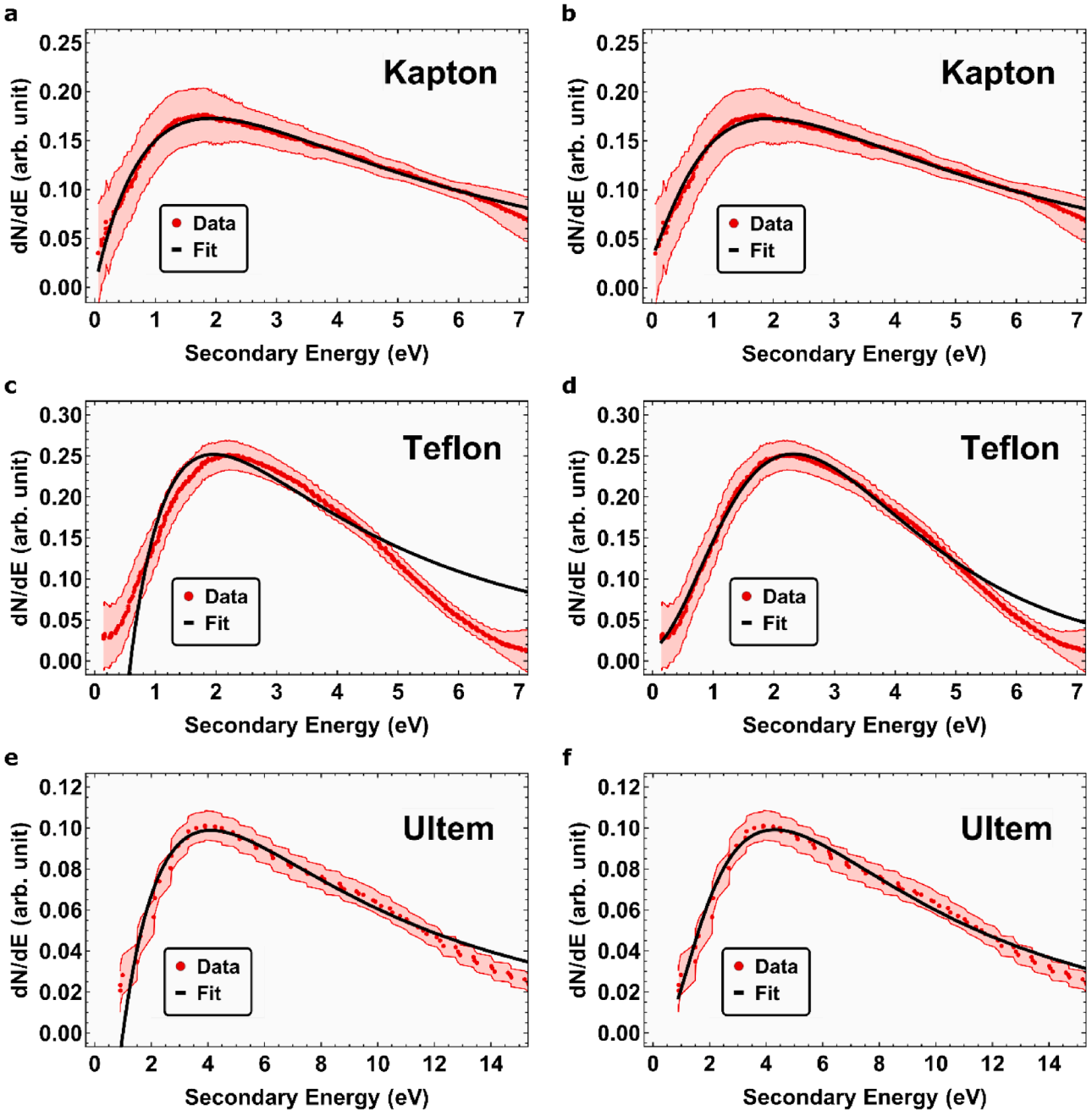

Fig. 6. EDCs of Kapton (top panels), Teflon (center panels) and Ultem (bottom panels) measured by the charging method. Red dots are the smoothed data obtained from the derivative of the charging curves $Q^{dep}(V_S^C)$, Eq. (6), and the distribution of electrons captured at a specific V_S^C. The data is shown alongside its error bands, calculated from the dispersion of the data. The best fit to the data (black line) of Eq. (1) (left panels) and Eq. (2) (right panels) is shown. The best fit parameters are shown in Table 2.

Table 2
Best fit parameters of the energy spectra of true secondary electrons to Equations (1) and (2) for Kapton, Teflon and Ultem irradiated at 300 eV PE. The estimated error represents the standard errors obtained from the fits to the data and the approximation 0.

	Equation (1)				Equation (2)			
	Electron Affinity (eV)		E_{peak} (eV)		E_{peak} (eV)			
Kapton	5.8	0.6	1.9	0.2	1.9	0.2	0.95	0. 10
Teflon	4.1	0.4	1.4	0.2	2.3	0.3	0.49	0.05
Ultem	9.2	0.9	3.1	0.3	4.3	0.5	0.84	0.08

Table 3
Secondary electron energy (E_{SE}). Energy at which 50% and 90% of the total population of emitted electrons fulfills E_{SE} E (where E_{SE} is the secondary electron energy) according to Equation (2).

	E @ 50% (eV)	E @ 90% (eV)
Kapton	5.4	18.9
Teflon	3.2	6.9
Ultem	8.7	25.4

analysis, Writing - original draft, Writing - review & editing. **I. Montero:** Supervision, Conceptualization, Methodology, Resources, Investigation, Writing - original draft, Writing - review & editing, Funding acquisition.

Declaration of Competing Interest

The authors declare that they have no known competing financial interests or personal relationships that could have appeared to influence the work reported in this paper.

Acknowledgments

This work was supported by the Spanish Ministry of Science and Innovation under *Proyectos de I D I Excelencia y Retos de la Investigacion,* Projects No ESP2015-67842-P and RTI2018-095903-B-I00.

References

[1] Bellissimo A, Pierantozzi GM, Ruocco A, Stefani G, Ridzel OY, Astasauskas V, Werner WSM, Taborelli M. Secondary electron generation mechanisms in carbon allotropes at low impact electron energies. J Electron Spectrosc Relat Phenom 2019;241:146883.
[2] Goldstein JI, Newbury DE, Michael JR, Ritchie NWM, Scott JHJ, Joy DC. Scanning electron microscopy and X-ray microanalysis. New York: Springer; 2017.
[3] Kirby R, Artifacts in Secondary Electron Emission Yield Measurements, 07/06 2004, DOI:10.2172/827328.
[4] Gonzalez-Iglesias D, et al. Analysis of Multipactor RF breakdown in a waveguide containing a transversely magnetized ferrite. IEEE Trans Electron Devices 2016;63 (12):4939 47. https://doi.org/10.1109/ted.2016.2614370.
[5] de Lara J, et al. Multipactor prediction for on-board spacecraft RF equipment with the MEST software tool. IEEE Trans Plasma Sci 2006;34(2):476 84. https://doi.org/10.1109/tps.2006.872450.
[6] Tulu ET, van Rienen U, Arnold A. Systematic study of multipactor suppression techniques for a superconducting rf gun. Phys Rev Accel Beams 2018;21(11). https://doi.org/10.1103/PhysRevAccelBeams.21.113402.
[7] Vague J, et al. Multipactor effect characterization of dielectric materials for space applications. IEEE Trans Microwave Theory Techn 2018;66(8):3644 55. https://doi.org/10.1109/TMTT.2018.2845869.
[8] Li Y, Cui W-Z, Wang H-G. Simulation investigation of multipactor in metal components for space application with an improved secondary emission model. Phys Plasmas 2015;22(5):053108. https://doi.org/10.1063/1.4919858.
[9] Bronchalo E, et al. Secondary electron emission of Pt: experimental study and comparison with models in the multipactor energy range. IEEE Trans Electron Devices 2016;63(8):3270 7. https://doi.org/10.1109/TED.2016.2580199.
[10] Cimino R, et al. Can low-energy electrons affect high-energy physics accelerators? Phys Rev Lett 2004;93(1):014801.
[11] Domínguez O, et al. First electron-cloud studies at the Large Hadron Collider. Phys Rev ST Accel Beams 2013;16(1):18. https://doi.org/10.1103/PhysRevSTAB.16.011003. 011003.
[12] Cimino R, Gonzalez LA, Larciprete R, Di Gaspare A, Iadarola G, Rumolo G. Detailed investigation of the low energy secondary electron yield of technical Cu and its relevance for the LHC. Phys Rev ST Accel Beams 2015;18(5):051002. https://doi.org/10.1103/PhysRevSTAB.18.051002.
[13] Valizadeh R, Malyshev OB, Wang S, Sian T, Cropper MD, Sykes N. Reduction of secondary electron yield for E-cloud mitigation by laser ablation surface engineering. Appl Surf Sci 2017;404:370.
[14] Olano A, Ren J, Zhang G, Tang H, Zhang T, Li J. Improvements in miniaturized Hall Thrusters by use of high-temperature SmCo magnets and additive manufacturing techniques. IOP Conf Series: Mater Sci Eng 2019;576:012002. https://doi.org/10.1088/1757-899x/576/1/012002.
[15] Garcia AO, Tang H, Ren J. Scaling model for SPT and TAL thrusters. IEEE Trans Plasma Sci 2020;48(1):86 98. https://doi.org/10.1109/TPS.2019.2958187.
[16] Levchenko I, Xu S, Teel G, Mariotti D, Walker MLR, Keidar M. Recent progress and perspectives of space electric propulsion systems based on smart nanomaterials. Nature Commun 2018;9(1):879. https://doi.org/10.1038/s41467-017-02269-7.
[17] Langendorf S, Walker M. Effect of secondary electron emission on the plasma sheath. Phys Plasmas 2015;22(3):033515. https://doi.org/10.1063/1.4914854.
[18] Pigeon V, Claire N, Arnas C, Terasaka K, Inagaki S. Plasma sheath material induced dependence due to secondary electron emission. Phys Plasmas 2020;27(4):043505. https://doi.org/10.1063/1.5141348.
[19] Tavant A, Croes V, Lucken R, Lafleur T, Bourdon A, Chabert P. The effects of secondary electron emission on plasma sheath characteristics and electron transport in an ${\bf{E}}\times {\bf{B}}$ discharge via kinetic simulations. Plasma Sources Sci Technol 2018;27(12):124001. https://doi.org/10.1088/1361-6595/aaeccd.
[20] Aguilera L, et al. CuO nanowires for inhibiting secondary electron emission. J Phys D-Appl Phys 2013;46(16):6. https://doi.org/10.1088/0022-3727/46/16/165104 (in English) Art no. 165104.
[21] Montero I, Aguilera L, Davila ME, Nistor VC, Gonzalez LA, Galan L, Raboso D, Ferritto R. Secondary electron emission under electron bombardment from graphene nanoplatelets. Appl Surf Sci 2014;291:74 7. https://doi.org/10.1016/j.apsusc.2013.10.045.
[22] Montero I, et al. Low-secondary electron emission yield under electron bombardment of microstructured surfaces, looking for multipactor effect suppression. J Electron Spectrosc Relat Phenom 2020;241:146822. https://doi.org/10.1016/j.elspec.2019.02.001.
[23] Nistor V, et al. Multipactor suppression by micro-structured gold/silver coatings for space applications. Appl Surf Sci 2014;315:445 53. https://doi.org/10.1016/j.apsusc.2014.05.049.
[24] Lu Qi, et al. Surface roughness evolution induced low secondary electron yield in carbon coated Ag/Al substrates for space microwave devices. Appl Surf Sci 2020; 501:144236. https://doi.org/10.1016/j.apsusc.2019.144236.
[25] Pivi M, King FK, Kirby RE, Raubenheimer TO, Stupakov G, Le Pimpec F. Sharp reduction of the secondary electron emission yield from grooved surfaces. J Appl Phys 2008;104(10):104904. https://doi.org/10.1063/1.3021149.
[26] Jin C, Ottaviano A, Raitses Y. Secondary electron emission yield from high aspect ratio carbon velvet surfaces. J Appl Phys 2017;122(17):5. https://doi.org/10.1063/1.4993979. 173301.
[27] Swanson C, Kaganovich ID. Modeling of reduced secondary electron emission yield from a foam or fuzz surface. Art no. 023302 J Appl Phys 2018;123(2):6. https://doi.org/10.1063/1.5008261.
[28] Wood B, Lee J, Wilson G, Shen T-C, Dennison JR. Secondary electron yield measurements of carbon nanotube forests: dependence on morphology and substrate. IEEE Trans Plasma Sci 2019;47(8):3801 9. https://doi.org/10.1109/TPS.2019.2921505.
[29] Huerta CE, Patino MI, Wirz RE. Secondary electron emission from textured surfaces. J Phys D: Appl Phys 2018;51(14):8. https://doi.org/10.1088/1361-6463/aab1ac. Art no. 145202.
[30] Ye Ming, Feng Peng, Li Yun, Wang Dan, He Yongning, Cui Wanzhao. The total secondary electron yield of a conductive random rough surface. J Appl Phys 2019; 125(4):043301. https://doi.org/10.1063/1.5023769.
[31] Bajek D, et al. Role of surface microgeometries on electron escape probability and secondary electron yield of metal surfaces. Sci Rep 2020;10(1):250. https://doi.org/10.1038/s41598-019-57160-w.
[32] Wang Dan, He Yongning, Ye Ming, Peng Wenbo, Cui Wanzhao. Secondary electron emission characteristics of nanostructured silver surfaces. J Appl Phys 2017;122 (15):153302. https://doi.org/10.1063/1.4989965.
[33] Swanson C, Kaganovich ID. Feathered fractal surfaces to minimize secondary electron emission for a wide range of incident angles. J Appl Phys 2017;122(4): 043301. https://doi.org/10.1063/1.4995535.
[34] He YN, et al. Thermal evaporated hyperbranched Ag nanostructure as an effective secondary-electron trapping surface coating. AIP Adv 2016;6(2):025122. https://doi.org/10.1063/1.4943050.
[35] Wu D, Ma J, Bao Y, Cui W, Hu T, Yang J, Bai Y. Fabrication of porous Ag/TiO2/Au coatings with excellent multipactor suppression. Sci Rep 2017;7(1):43749. https://doi.org/10.1038/srep43749.
[36] Olano L, Davila ME, Dennison JR, Martín-Iglesias P, Montero I. Dynamic secondary electron emission in rough composite materials. Sci Rep 2019;9(1):13967. https://doi.org/10.1038/s41598-019-50353-3.
[37] Tao SX, Chan HW, Van der Graaf H. Secondary electron emission materials for transmission dynodes in novel photomultipliers: a review. Materials 2016;9(12): 1017.
[38] Yang F, Wang J, Liu W, Liu X, Zhou M. Y2O3 Lu2O3 co-doped molybdenum secondary emission material. Appl Surf Sci 2013;270:746 50. https://doi.org/10.1016/j.apsusc.2013.01.147.
[39] Photomultiplier tubes: Basics and applications. Hamamatsu photonics, 2017.
[40] Gilmour AS. Klystrons, traveling wave tubes, crossed-field amplifiers, and gyrotrons. Magnetrons: Artech House; 2011.
[41] Dennison JR, Sim A, Thomson CD. Evolution of the electron yield curves of insulators as a function of impinging electron fluence and energy. IEEE Trans Plasma Sci 2006;34(5):2204 18. https://doi.org/10.1109/tps.2006.883398.
[42] Belhaj M, Tondu T, Inguimbert V, Elsafi B, Fakhfakh S, Jbara O. Electron emission yield and charging process of alkali-silicate glass submitted to an electron beam under the varying temperature condition. Nucl Instrum Methods Phys Res, Sect B 2012;270:120 7. https://doi.org/10.1016/j.nimb.2011.09.010.
[43] Chen Yu, Wu J, Kunimitsu R, Gray A, Toyoda K, Cho M. Total electron emission yield of solar cell coverglass and optical solar reflector. IEEE Trans Plasma Sci 2013;41(12):3558 64. https://doi.org/10.1109/TPS.2013.2288575.
[44] I. Montero, L. Aguilera, D. Raboso, and U. Wochner, Anti-multipactor device, Patent WO2016042192 A1, 2016-03-24, 2016. [Online]. Available: http://hdl.handle.net/10261/135730.
[45] Cazaux J. Secondary electron emission and charging mechanisms in Auger Electron Spectroscopy and related e-beam techniques. J Electron Spectrosc Relat Phenom 2010;176(1-3):58 79. https://doi.org/10.1016/j.elspec.2009.06.004.
[46] Cazaux J. About the secondary electron yield and the sign of charging of electron irradiated insulators. Eur Phys J AP 2001;15(3):167 72. https://doi.org/10.1051/epjap:2001178.
[47] Cazaux J. e-Induced secondary electron emission yield of insulators and charging effects. Nucl Instrum Methods Phys Res, Sect B 2006;244(2):307 22. https://doi.org/10.1016/j.nimb.2005.10.006 (in English).
[48] Melchinger A, Hofmann S, and W. W., Dynamic double layer model: Description of time dependent charging phenomena in insulators under electron beam irradiation, Journal of Applied Physics, vol. 78, no. 10, pp. 6224-6232, 1995, DOI: 10.1063/1.360569.

[49] Whetten N Rey, Laponsky AB. Energy distribution of secondary electrons from MgO single crystals. Phys Rev 1957;107(6):1521 4. https://doi.org/10.1103/PhysRev.107.1521.
[50] R. Hoffmann, Electron-Induced Electron Yields of Uncharged Insulating Materials, All Graduate Theses and Dissertations, 01/01 2010.
[51] Olano L, Montero I. Electron emission spectra by charging analysis. Results Phys 2020;17:103050. https://doi.org/10.1016/j.rinp.2020.103050.
[52] Ghorbel N, Kallel A, Damamme G. Analytical model of secondary electron emission yield in electron beam irradiated insulators. Micron 2018;112:35 41. https://doi.org/10.1016/j.micron.2018.06.002.
[53] J. Dennison et al., ABSOLUTE ELECTRON EMISSION CALIBRATION: ROUND ROBIN TESTS OF Au AND GRAPHITE. 2016.
[54] Kapton HN. https://www.dupont.com/products/kapton-hn.html (accessed 8 July, 2020).
[55] Teflon. http://www.tetrachim.com/pdf/Teflon_industrialcoatingsbrochure_GB.pdf (accessed 8 July, 2020).
[56] Ultem 1000F. https://www.sabic.com/en/products/specialties/ultem-resins/ultem-resin (accessed 8 July, 2020).
[57] Perrin C et al., Space charge detection in Kapton (R) and PTFE polymer films by the open Pulsed Electro-Acoustic method, (in English), High Perform. Polym., Article; Proceedings Paper vol. 20, no. 4-5, pp. 535-548, Aug-Oct 2008, DOI: 10.1177/0954008308089714.
[58] Bungay CL, Tiwald TE, Devries MJ, Dworak BJ, Woollam JA. Characterization of UV irradiated space application polymers by spectroscopic ellipsometry. Polym. Eng. Sci. 2000;40(2):300 9. https://doi.org/10.1002/pen.11163.
[59] Plis E, Engelhart D, Cooper R, Johnston W, Ferguson D, Hoffmann R. Review of radiation-induced effects in polyimide. Appl Sci 2019;9:1999. https://doi.org/10.3390/app9101999.
[60] Chung MS, Everhart TE. Simple calculation of energy distribution of low-energy secondary electrons emitted from metals under electron bombardment. J Appl Phys 1974;45(2):707 9. https://doi.org/10.1063/1.1663306.
[61] Scholtz JJ, Dijkkamp D, Schmitz RWA. Secondary electron emission properties. Philips J Res 1996;50(3):375 89. https://doi.org/10.1016/S0165-5817(97)84681-5.
[62] Nickles N, Davies R, and Dennison J, Applications of Secondary Electron Energy-and-Angular-Distributions to Spacecraft Charging, 01/01 2000.
[63] Comsol 5.3a. https://www.comsol.com/release/5.3a (accessed 31 March 2020.
[64] Reimer L. Image formation in low-voltage scanning electron microscopy. SPIE Optical Engineering Press; 1993.
[65] W. Wang, T. Takada, Y. Tanaka, and S. Li, Space charge mechanism of polyethylene and polytetrafluoroethylene by electrode/dielectrics interface study using quantum chemical method, IEEE Transactions on Dielectrics and Electrical Insulation, vol. 24, no. 4, pp. 2599-2606, 2017, doi: 10.1109/TDEI.2017.006417.
[66] Kafafi SA. The ionization potential, electron affinity and energy gap of polyimide. Chem Phys Lett 1990;169(6):561 3. https://doi.org/10.1016/0009-2614(90)85647-U.
[67] Kleiman J. Protection of materials and structures from the space environment: ICPMSE-11. Springer International Publishing; 2017.
[68] Stellman JM and I L. Office, Encyclopaedia of Occupational Health and Safety (no. v. 2). International Labour Office, 1998.
[69] Haynes WM. CRC handbook of chemistry and physics. CRC Press; 2016.

4 Conclusions

The main results of this thesis can be found below:

Research on a new way to decrease the SEY of surfaces.

- Composite materials with very low SEY have been investigated in the laboratory.
- A hypothesis of the process that renders low SEY to composite surfaces has been proposed.
- Computer simulations have been performed to proof the hypothesis of the model and also physical insight has been extracted.
- The charging process is dependent on several factors:
    - Size of the metal/dielectric domains. The bigger the domains the higher the surface voltage that is achieved for a constant incident electron flux.
    - Incident electron flux. The higher the electron flux, the higher the achieved surface voltage.
    - Time constant of the discharging process. If the time constant is low, the charge easily dissipates and the surface voltage reaches lower values.
- Surfaces with SEY lower than 0.2 up to incident energies around 1 keV were characterized. It was shown that this was directly produced by the synergistic effect between the charging of the dielectric domains and the surface roughness.
- The potential difference between conductor and dielectric domains needed to considerably decrease the SEY is smaller than 2 V.
- The potential quickly vanishes over the surface and therefore do not produce any effect outside the closer volume of space over the surface.
- Conductive composite materials with dielectric and conductor domains can be designed. These would be suitable to coat surfaces to avoid the Multipactor effect.

New technique to measure the electron energy spectra of dielectric materials

- The charging process of flat dielectric samples was studied.
- It was proposed that the charging process conveys information of the energetic nature of the emitted electrons. As the dielectric surface charges positively, a

potential barrier will grow over the surface. The emitted secondary electrons will have to overcome this potential barrier, with electrons with not enough energy falling back to the surface.

- This hypothesis was first put into practice in floating conductor samples. Energy spectra of conductor samples can be obtained using a Hemispherical Electron Energy Analyzer (HEEA). Therefore, the energy spectra of the samples measured by the proposed method was contrasted with the HEEA measurement.
- The method takes into account that the surface voltage in conductors is homogeneous in all the surface therefore, all the secondary electrons have to overcome the same potential barrier.
- The proposed method was able to measure the energy of the true secondary electrons (those emitted with lower energies) which contribute to most of the secondary electron population.
- The proposed method accurately measures the lowest peak of the secondary spectra and the FWHM of the distribution.
- The method was then applied to dielectric samples whose energy spectra is not easy to obtain by other methods. The dielectric samples were Kapton, Teflon and Ultem.
- The method takes into account that, the deposited charge on a dielectric surface is homogeneously distributed as a consequence of a homogeneous beam. However, as the surface is not equipotential, the secondary electrons have to overcome different potential barriers depending on the position from where they are emitted. This fact is taken into account and the energy analysis is performed similarly to the conductor materials.
- In addition, the position of the peak of the spectra of true secondary electrons was determined, being 1.9 ± 0.1 eV for Kapton, 2.3 ± 0.1 eV for Teflon and 4.3 ± 0.2 eV for Ultem.

5 Conclusiones

Los principales resultados de esta tesis se enumeran a continuación:

Investigación sobre una nueva forma de disminuir la SEY de superficies.

- Se han investigado en el laboratorio materiales compuestos con SEY muy bajo.
- Se ha propuesto una hipótesis del proceso que confiera una SEY baja a las superficies compuestas.
- Se han realizado simulaciones por ordenador para comprobar la hipótesis del modelo propuesto y se ha extraído más información del proceso.
- El proceso de carga depende de varios factores:
    - Tamano de los dominios metal/dieléctrico. Cuanto mayores son los dominios, mayor es el potencial superficial que se obtiene para un flujo de electrones incidente constante.
    - Flujo de electrones incidente. Cuanto mayor sea el flujo de electrones, mayor será el potencial superficial alcanzado.
    - Constante de tiempo del proceso de descarga. Si la constante de tiempo es baja, la carga se disipa fácilmente y el potencial superficial alcanza valores más bajos.
- Se caracterizaron superficies con SEY inferior a 0.2 hasta energías incidentes de alrededor de 1 keV. Se demostró que esto se produjo directamente por el efecto sinérgico entre la carga acumulada en los dominios dieléctricos y la rugosidad de la superficie.
- La diferencia de potencial entre los dominios conductor y dieléctrico necesario para disminuir considerablemente el SEY es menor que 2 V.
- El potencial decrece rápidamente sobre la superficie y por lo tanto no produce ningún efecto fuera del volumen más cercano del espacio sobre la superficie.
- Pueden diseñarse materiales compuestos conductores con dominios dieléctricos y conductores. Estos serían adecuados para revestir superficies con el objetivo de evitar el efecto Multipactor.

Nueva técnica para medir los espectros de energía de electrones de materiales dieléctricos

- Se estudió el proceso de carga de muestras dieléctricas planas.
- Se propuso que el proceso de carga transmite información de la naturaleza energética de los electrones emitidos. A medida que la superficie dieléctrica se carga positivamente, una barrera potencial crece sobre la superficie. Los electrones secundarios emitidos tendrán que superar esta barrera de potencial y los electrones sin suficiente energía son atraídos de nuevo a la superficie.
- Esta hipótesis se puso primero en práctica en muestras de conductores flotantes. Los espectros de energía de las muestras de conductores se pueden obtener utilizando un analizador de energía de electrones hemisféricos. De esta manera, los espectros de energía de las muestras medidas por el método propuesto se contrastaron con la medición del analizador.
- El método tiene en cuenta que el potencial superficial en los conductores es homogéneo en toda la superficie, por lo que todos los electrones secundarios tienen que superar la misma barrera de potencial.
- El método propuesto fue capaz de medir la energía de los verdaderos electrones secundarios (los emitidos con energías más bajas) que contribuyen a la mayor parte de la población de electrones secundarios.
- El método propuesto mide con precisión el pico más bajo de los espectros secundarios y el FWHM de la distribución.
- El método se aplicó entonces a muestras dieléctricas cuyos espectros de energía no son fáciles de obtener por otros métodos. Las muestras dieléctricas fueron Kapton, Teflon y Ultem.
- El método tiene en cuenta que, la carga depositada sobre una superficie dieléctrica se distribuye de manera homogénea como consecuencia de un haz homogéneo. Sin embargo, como la superficie no es equipotencial, los electrones secundarios deben superar diferentes barreras de potencial dependiendo de la posición desde donde se emiten. Este hecho es tenido en cuenta y el análisis energético se realiza como para el caso de materiales conductores.
- Además, se determinó la posición del pico de los espectros de electrones secundarios verdaderos, siendo 1.9 ± 0.1 eV para Kapton, 2.3 ± 0.1 eV para Teflon y 4.3 ± 0.2 eV para Ultem.